Investigation of Wire Arc Additive Manufacturing of nano-treated 7075 aluminum alloy

by

Shiyu Teng

A thesis submitted in partial fulfillment of the requirements for the degree of

Master of Science

Department of Mechanical Engineering
University of Alberta

Abstract

This novel study makes it possible to manufacture high-quality, large-size 7075 aluminum alloy parts through additive manufacturing. The study comprehensively investigates the process and the control of the quality of the nano-treated 7075 aluminum alloy part manufactured by the in-situ multi-sensor Cold Metal Transfer (CMT) Wire Arc Additive Manufacturing (WAAM) system. A complete research flow, including equipment and environment setup, measurement calibration, process parameter exploration, and quality control, is presented in this study. To achieve the research in this research flow, five sub-studies were performed. An in-house in-situ multi-sensor WAAM system (referred to as WAAM system) was first built with the ability to conduct the WAAM printing process, and monitor and record the temperature during the printing process, layer's contour geometry, and energy input in-situ. To ensure the temperature measured and recorded in this study is correct, calibration work on the emissivity of the WAAM-made 7075NT aluminum wall was done. A full-factorial screening experiment was then designed and carried out to screen out the vital process parameters that significantly affect the geometrical properties. Next, the screened parameters are used to find the parameter set that leads to sound layer geometry and the lowest energy consumption. Finally, two heat management strategies, Critical Dwell Time and Critical Interpass Temperature, are applied in the CMT-base WAAM process to validate the weldability of 7075NT aluminum alloy and investigate how these two strategies affect and control the thermal state, and the geometrical and mechanical properties of the parts.

Preface

A version of Chapter 3 of this thesis is submitted to a peer-reviewed journal published in The International Journal of Advanced Manufacturing Technology under the title “Effect of Surface Texture, Viewing Angle, and Surface Condition on the Emissivity of Wire Arc Directed Energy Deposition Manufactured 7075 nano-treated Aluminum Alloy”.

Acknowledgments

I would like to show my sincerest thanks to my supervisors Dr. Ahmed Jawed Qureshi, Dr. Hani Henein, and Dr. Tonya Wolfe. Their guidance, advice and supervision have made this work a success. They have always had my best interest and supported me during the hardest of times. Thank you for all your time and support.

Thanks also to post-doctor fellow Dr. Thomas Lehmann, Co-op student Abdullah Hashmi, and my friend Michael (Yeon Kyu) Kwak for your precious suggestion to my work related to electrical engineering and the experiment equipment setup in this work.

I am also extremely grateful to Dr. Shirin Dehgahi and Anne McDonald. Thank you for your reviewing, advice, and supervision when I struggled to find help with my work.

Thanks to my friends in my research group, Adam Zhe Kuan Lim, Ali Mulhi, Piyush Arora, Yifan Li, Shukoufeh Sardarian, Janmejay Rao, Shalini Singh, Remy Samson, Feiyu Jia and others. Thank you for all of your help and support when I am in need. My friendship with you helped me quickly adjust and get used to my new life.

I am also immensely grateful to my mother Shouxia Li and father Yue Teng for everything they have done for raising me and being there for me through my most difficult times. Your support has made me reach where I am today and will never be ignored.

Finally, thanks to the Mechanical Engineering Department and the University of Alberta. Thank you for giving me the opportunity and resources to study.

Table of Contents

Abstract ii
Preface iii
Acknowledgments iv
Table of Contents v
1. Introduction 1
1.1 The Development of Additive Manufacturing 1
1.2 The Process Chain of AM 2
1.3 The Classification and Current Usage of AM 3
1.4 Wire Arc Additive Manufacturing (WAAM) 6
1.5 Cold Metal Transfer (CMT) 8
1.6 Aluminum Alloy in Wire Arc Additive Manufacturing (WAAM) 9
1.7 Literature Review 10
1.8 Motivation and Research Objective 13
1.8.1 Motivation and Challenges in WAAM process with 7075NT aluminum alloys 13
1.8.2 Research Objectives 14
2. Setup of the sensor-fused CMT-based WAAM system 15
2.1 Introduction 15
2.2 The Setup of the Deposition Module 17
2.3 The Setup of the Monitoring Module 17
3. The Emissivity Calibration on the WAAM Manufactured 7075NT Aluminum Alloy Part. 21
3.1 Introduction 21
3.2 Experiment setup and design 23
3.2.1 Experiment Setup 23
3.2.2 Design of Experiment 27
3.3 Result and Discussion 29
3.3.1 Effect of Surface Texture and Temperature on the Emissivity 29
3.3.2 Effect of Viewing Angle and Temperature on Emissivity 34
3.3.4 Effect of the Surface Condition and Coating on Emissivity 37
3.4 Chapter Conclusion 41

4. WAAM Parameter Screening Experiment 42
4.1 Introduction 42
4.2 Experimental Design 42
4.3 Result and Discussion 45
4.4 Chapter Conclusion 48
5. WAAM Process Parameter Exploration 49
5.1 Introduction 49
5.2 The Influence of WFS and CTWD on Process Current and Voltage 50
5.2.1 Introduction of Synergic Line and CTWD 50
5.2.2 Experimental Design 53
5.2.3 The Effect of WFS and CTWD on Synergic Line 54
5.2.4 Conclusion 56
5.3 Exploring the Proper WFS and TTS for Sound Geometrical Property 57
5.3.1 Experimental Design 57
5.3.2 The Analysis of the WFS on the Layer Geometrical Property 59
5.3.3 Conclusion 61
5.4 Chapter Conclusion 61
6. Heat Management and Quality Control 63
6.1 Introduction 63
6.2 Design of Experiment 63
6.3 Result and Analysis 66
6.3.1 The Analysis of Geometrical properties 66
6.3.2 The Analysis of Heat Accumulation on Part's Geometrical Properties 75
6.3.3 The Analysis of Mechanical Properties 86
6.1 Chapter Conclusion 96
7. Conclusions and Feature Works 98
7.1 Conclusion 98
7.2 Future Work 99
Bibliography 101
Appendix **I** 109

List of Tables

Table 1. The feature of the popular AM technologies [2]. 5
Table 2. Common layer heights by technology [13]..... 6
Table 3. Composition of the 7075NT wire 10
Table 4. The factors that affect emissivity. 22
Table 5. Printing parameters and surface texture (Sq) 24
Table 6. The detail of experiment Group 1 and Group 2..... 28
Table 7. The detail of experiment Group 3..... 29
Table 8. The third-degree fitting results for different surface conditions. 40
Table 9. The definition of factors for WAAM. 43
Table 10. The parameter set of screening experiment and responses. 44
Table 11. The definition and unit of responses..... 45
Table 12. The detail of the parameters set in the experiment. 54
Table 13. The average current (Ia) and the average voltage (Ua) at different CTWD 56
Table 14. The energy consumption at the different WFS. 59
Table 15. The best-fitted parameter set in the CMT-based 7075NT aluminum alloy fabrication process..... 62
Table 16. The critical dwell time and critical interpass temperature designed in the experiment.65
Table 17. The walls' geometrical properties..... 73
Table 18. The P-Value (confidential interval = 95%) and R-sq of the RSM analysis on the layer 1 to layer 7. 82
Table 19. The P-Value (confidential interval = 95%) and R-Sq of the RSM analysis on the layer 8 to layer 25. 84
Table 20. The database of the first 7 layers. 85
Table 21. The comparison of mechanical properties between 7075NT and traditional 7075 aluminum alloy. 90
Table 22. The detail of tensile testing result (Yield strain offset = 0.2%). 91
Table 23.The detail of the test of 7075NT aluminum alloy density. 92
Table 24. The detail of the calculated parameters of the porosity test. 95

Table 25. The detail of tensile testing result (EUL = 0.5% strain). 109

List of Symbols

ε	-	Emissivity
η	-	The arc efficiency of CMT welding
σ_{yield}	MPa	The stress at the yield point
ε_{yield}	mm/mm	The strain at the yield point
ΔT	℃	The difference of the interpass temperature of the latest deposited layer
c_p	J/K	The heat capacity of nano-treated AA7075
m	g	The mass of a deposited layer
t_{layer}	s	The duration of depositing a layer
t_d	s	The duration of the detachment stage in a CMT cycle
y_i^{actual}	-	The actual data that collected by the multi-sensor WAAM system
$y_i^{predicted}$	-	The predicted data calculated by the linear regression models
HI	J/mm	Heat input
I_a	A	The average current
I_g	A	The ground current in Synergic Line
I_p	A	The pulse current in Synergic Line
L_{layer}	mm	The length of a layer
Q	J	The heat accumulation in the part
Q_{input}	J	The heat flux into the part
$Q_{dissipation}$	J	The heat dissipates from the part
Sq	mm	The root mean square height
T_{IR}	℃	The temperature that the infrared device captured
T_{True}	℃	The true temperature that the thermocouple captured
T_{dt}^{start}	℃	The interpass temperature at the start of the dwell phase
T_{dt}^{end}	℃	The interpass temperature at the end of the dwell phase
U_a	V	The average voltage
W_{layer}	g	The weight of a layer

List of Figures

Figure 1. The typical AM process chain [2]. 3
Figure 2. (a) The newly registered patents in AM area; (b) The application areas that AM is being used for [7]. 4
Figure 3. Popular materials used in AM technology [7]. 5
Figure 4. A typical Wire Arc Additive Manufacturing (WAAM) system (RAMLAB, 2022). 8
Figure 5. The wire motion in a single CMT cycle. 9
Figure 6. The sub-studies and their classification. 14
Figure 7. The physical setup of the WAAM system. 16
Figure 8. The structure of the sensor-fusion WAAM system. 16
Figure 9. The design of the thermocouple pad. 19
Figure 10. The setup of the IR camera. 19
Figure 12. Current and voltage measurement setup 20
Figure 13. Surface texture extraction workflow. (a) The location and size of the scanning area on the WAAM-made wall. (b) The profiler scans the surface topography. (c) The surface texture after applying the filter. 25
Figure 14. (a) The top view of the five different viewing angles. (b) The setup of thermocouples. 25
Figure 15. The volume fraction of liquid of 7075NT with respect to temperature.. 27
Figure 16. The emissivity examined at five different surface texture levels. 29
Figure 17. The cross-section of the WAAM-made wall. 31
Figure 18. Surface mean profiles and temperature mean profiles along the horizontal and vertical direction at the surface texture of (a) $Sq = 0.39$, (b) $Sq = 0.30$, (c) $Sq = 0.24$, (d) $Sq = 0.18$, and (e) $Sq = 0.12$. 32
Figure 19. The standard deviation of (a) waviness profiles and (b) temperature profiles at different surface texture levels. 33
Figure 20. The effect pathway of the factors. 34
Figure 21. Effect of viewing Angle on the emissivity. 35
Figure 22. The change of the emissivity with the TIR in (a) different surface textures and (b) viewing angles. 36

Figure 23. (a) The white oxidized coating attached on the surface. (b) The dark carbonized coating after removing the oxidized coating. (c) The schematic of the layout of the oxidized and carbonized coatings. 38
Figure 24. Four post-processed surface areas on one WAAM-made part by 7075NT aluminum alloy 38
Figure 25. The emissivity gradient of (a) raw surface, (b) polished surface, (c) carbonized coating, and (d) oxidized coating. 39
Figure 26. Printing path of each part used in the screening experiment. 45
Figure 27. (a) An unstable current at the starting and ending of a layer indicates the arc is unstable when igniting and extinguishing. (b) The torch displacement versus time plot shows there is significant acceleration and deceleration of the torch. (c) Significant slumping happens at the two ends of the wall. 46
Figure 28. The chart of the Standardized Effect (a = 0.05) for each response. 47
Figure 29. The bijection relationship between WFS and Synergic Line. 50
Figure 30. The schematic current waveform in one cycle of CMT [87]. 51
Figure 31. The typical current waveform at WFS = 200 in/min of CMT in welding Q235 mild steel [85]. 52
Figure 32. Definition of contact tip to workpiece distance (CTWD) [88] 53
Figure 33. The current(a) and voltage(b) of the Synergic Line at different WFS. 55
Figure 34. The current(a) and voltage(b) of the Synergic Line at different CTWD. 55
Figure 35. The top view of the layer at the different WFS. 60
Figure 36. The Energy consumption at the different WFS. 61
Figure 37. The printing trajectory of the part used in this study. 63
Figure 38. The procedure of printing one single layer was applied in this study. 65
Figure 39. The appearance of the WAAM-made 7075NT aluminum alloy walls with two heat management strategies at different critical dwell times and critical interpass temperatures. 66
Figure 40. The range of the wall height and width of (a) Critical Dwell Time strategy and (b) Critical Interpass Temperature strategy. 67
Figure 41. The profiler scanning method of layer contours 68
Figure 42. The average wall cross-section for each wall. 69

Figure 43. The layer height and width for different strategies and critical factor levels. 70
Figure 44. The definition of (a) the layer height-to-width-ratio and (b) centerline deviation. 71
Figure 45. The layer height-to-width ratio for different strategies and critical factor levels..... 71
Figure 46. The mechanical property of (a) wall average height, (b) wall average width, (c) height-to-width ratio and (d) wall centerline deviation. 74
Figure 47. The illustration of the correlation between heat accumulation and two heat management strategies. 75
Figure 48. The interpass temperature and cooling rate in Critical Dwell Time strategy. 77
Figure 49. The substrate temperature in Critical Dwell Time strategy. 78
Figure 50. The interpass temperature and cooling rate in the Critical Interpass Temperature strategy. 79
Figure 51. The substrate temperature in the Critical Interpass Temperature strategy. 80
Figure 52. The contour plot of the effect of $Tdtstart$ and cooling rate on (a) layer height, (b) layer width, and (c) layer height-to-width ratio. 83
Figure 52. (a) The cutting layout. (b) The dimension of the tensile specimen (all dimensions are in mm). 86
Figure 53. The strain-stress curve of horizontal and vertical specimens in (a) Critical Dwell Time and (b) Critical interpass temperature strategies. 87
Figure 54. The stress-strain curve of (a) 7075 T6 aluminum alloy [91] and (b) NbC added steel [92]. 88
Figure 55. Comparison of (a) Young's modulus, (b) yield strength (0.5% offset method), and (c) ultimate tensile strength between specimens. 91
Figure 56. The illustration of the pixel counting process in ImageJ. 93
Figure 57. The porosity testing result. 94
Figure 58. Comparison of (a) Young's modulus, (b) yield strength (EUL = 0.5% strain), and (c) ultimate tensile strength between specimens. 109

1. Introduction

Additive Manufacturing, also called 3D printing, is a cutting-edge technology that can manufacture near-net-shape three-dimensional parts, bringing the benefits of time and cost-efficiency compared to traditional subtractive manufacturing. The term Additive Manufacturing is defined in the ISO/ASTM standard as, "A process of joining materials to make parts from 3D model data, usually layer upon layer, as opposed to subtractive manufacturing and formative manufacturing methodologies." [1]. In typical additive manufacturing, the part is built one layer at a time by depositing a new layer on top of the latest layer until the whole part is printed. In traditional subtractive manufacturing, such as machining, unwanted material is removed to leave the desired part. Additive manufacturing produces near-net-shape parts. Starting with nothing, AM can fabricate the part with only the volume of material required, avoiding material waste during the process and the time loss of removing unwanted material. Therefore, additive manufacturing inherently has low material waste and short manufacturing leading time.

1.1 The Development of Additive Manufacturing

The concept of additive manufacturing originates at the end of the twentieth century. At that time, people began to make topographical maps as 3D representations of terrain by overlaying multiple pieces of paper [2]. Modern additive manufacturing was first introduced and applied with the stereolithography technique by Otto John Munz in 1951 [3]. He designed a system that could selectively expose a transparent photo emulsion in a layer-wise fashion. Each layer was exposed with a cross-section of an object. During the process, the part being built was gradually lowered to vacate space to add the next layer, which was created with the addition of transparent photo emulsion. When the process was completed, the transparent cylinder contained a 3D image of the object. A drawback of this method was that to get the object after the process, the transparent photo emulsion had to be manually removed from the transparent cylinder. In the following years, a number of new additive manufacturing technologies were invented. One of the famous technique 3D polymerization additive manufacturing, was invented by Swainson in 1968 [4]. Swainson proposed a process that used two laser beams on a photosensitive polymer to solidify the desired pattern. The pattern was a slice of an object: one pattern, one layer. The object finally be printed

with several layers of pattern. In his patent, besides photosensitive polymer material, it is also proposed that the metal powder can also be used in this process. The metal powder can be melted and solidified to form a layer using a laser scanning process with a selected mask.

Another notable contribution was the application of stereolithography technology in additive manufacturing by Hideo Kodama [5]. He describes his invention as a "rapid prototyping device". Moreover, he was the first to file a patent describing the laser beam curing process. Sadly, his patent never went through because he gave up financing a year after filing the patent. The first commercialized additive manufacturing system did not start until 1986 with Charles W. Hull's stereolithography patent [6]. Charles W. Hull founded his start-up, UVP Inc., and marketed the first SLA machine in 1998.

While it has been referred to as "rapid prototyping", "3D printing", "net-shape manufacturing", and "freeform fabrication", over the last 30 years the fundamental principle of additive manufacturing has remained the same: depositing material in a layer-by-layer method to fabricate an object. With the flourishing development of this technology, in 2009, ISO (International Organization for Standardization) and ASTM (American Society for Testing and Materials) tried to standardize the term of this technology for its convenient usage in industry [1]. In this thesis, the term "Additive Manufacturing" or "AM" is used.

1.2 The Process Chain of AM

A typical additive manufacturing process chain is illustrated in Figure 1 [2]. Almost all additive manufacturing technologies start by creating a 3D model. In general, this 3D model is a CAD (Computer-Aided Design) model that is either generated by CAD software such as SolidWorks, AutoCAD or CATIA, or scanned from the 3-dimentional topographic scanner. It is important to note that the surface of the CAD model must be a fully enclosed volume because any gaps on the model's surface could be a problem during the slicing step.

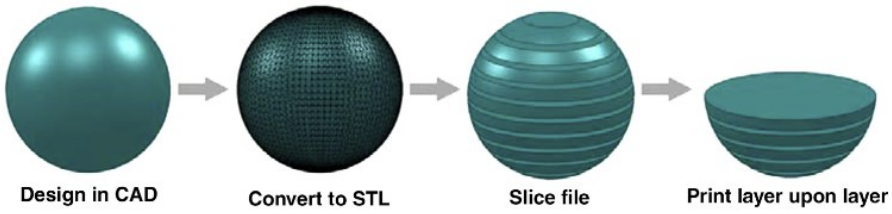

Figure 1. The typical AM process chain [2].

The CAD model needs to be converted into a format that the AM machine understands which in most processes is STL (Standard Triangulation Language). The STL file is the finite triangulated meshed form of the CAD model and, after conversion, the model becomes a calculable object by machine, similar to the application of calculus. The resolution of the STL file is one factor affecting the part's geometrical accuracy. The better resolution of the STL file, the higher the part's geometrical accuracy.

As the part is being built in a layer-by-layer process, the extruder trajectory and the printing sequence of layers need to be defined before material deposition can begin. Traditionally, the trajectory can be created by writing gcode manually. This step is called "slicing", in which the STL model is sliced into several parallel printing layers. Depending on the AM technology, the material, and the machine's resolution, many deposition parameters must be assigned, such as the layer thickness, support, printing speed, and temperature. Fortunately, nowadays, commercial software is often able to automatically slice the STL model with proper parameters that fit the intended machine and material.

Once the sliced file is uploaded to the machine, the material deposition process starts, and the part is fabricated when all layers are printed. In most processes, postprocessing is needed to clean the part of leftover powder or resin or to remove support structure.

1.3 The Classification and Current Usage of AM

In the past 30 years, AM technology has been broadly investigated, developed, and applied for different use cases. Based on the "Wohlers Report 2019: 3D Printing and AM State of the Industry" [7], the world's major economic and industrial powers are rapidly developing AM technologies. The sum of newly registered AM-related patents of U.S., Germany, Japan, and China took up to

63.4% of total AM-related patents in 2019, (Figure 2 (a)). New technology is always serving the requirements of the real world. Figure 2(b) shows the application areas where AM is used. It can be seen that most AM technologies are used for consumer products, motor vehicles, medical, and industrial machines. Aerospace follows behind. The demands for AM technology from these fields accelerate the development of new AM technology.

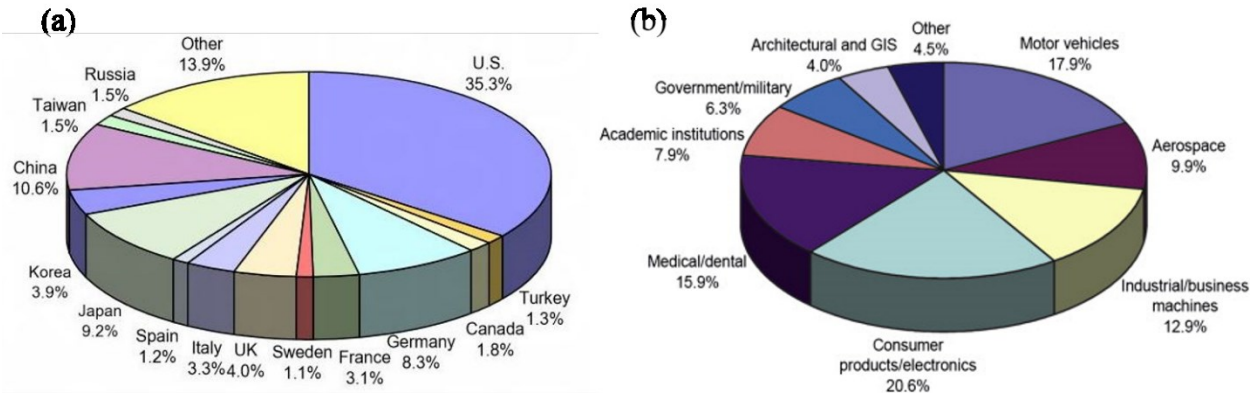

Figure 2. (a) The newly registered patents in AM area; (b) The application areas that AM is being used for [7].

AM technologies are classified into seven categories based on the heat source and the material. The seven categories are: Stereolithography (SLA), Fused Deposition Modeling (FDM), Material Jetting (MJ), Binder Jetting (BJ), Selective Laser Melting (SLM), and Selective Laser Sintering (SLS). Each category features instances of broad commercialization and applications in civil and industrial field for a diversity of geometrical and mechanical demands. The features of each category of AM technologies are listed in Table 1.

From the material aspect, many materials such as Photopolymers, Polymer Powders, Filaments, and metals have enabled to be applied in AM process. Figure 3 shows the percentage of materials used in AM technologies. As the most critical material in human history and the base of modern industry, metals keep showing value and attracting people. Due to its previously mentioned advantages, AM continues to be implemented in metal part manufacturing instead of subtractive manufacturing, especially for high-value metal parts such as rocket nozzle or aero plane high strength aluminum alloy parts. These high-value applications have been one of the main streams of implementing AM technology, especially in the cases of fabricating metal 3D parts in the automobile and aerospace industry [8].

Table 1. The feature of the popular AM technologies [2].

Technology	Process	Application	Material	Precision
SLA	Cured with laser	Injection molds like polymer prototypes, jewelry, dental and medical application, hearing aids	Photopolymer resins	±0.5% (lower limit: ±0.15mm)
FDM	Melted or UV cured	Functional parts in the aerospace and automotive industry, medical and dental application	Thermoplastic filament	±0.5% (lower limit: ±0.5mm)
MJ	Cured with UV light	Colorful prototype, medical models, Small batch injection molds	Thermoset photopolymer resins	±0.1mm
BJ	Joined with bonding agent	Functional metal parts, full-color modes, sand casting, architectural models, packaging, ergonomic verification	Send, Gypsum, Metal powder	±0.2mm (metal) or ±0.3mm (sand)
SLM	Fused with laser	Functional metal parts in aerospace and automotive, medical and dental application.	Metal powder	±0.1mm
SLS	Fused with laser (sintering)	Functional polymer parts, complex ducting, low run part production.	Thermoplastic powder	±0.3% (lower limit: ±0.3mm)

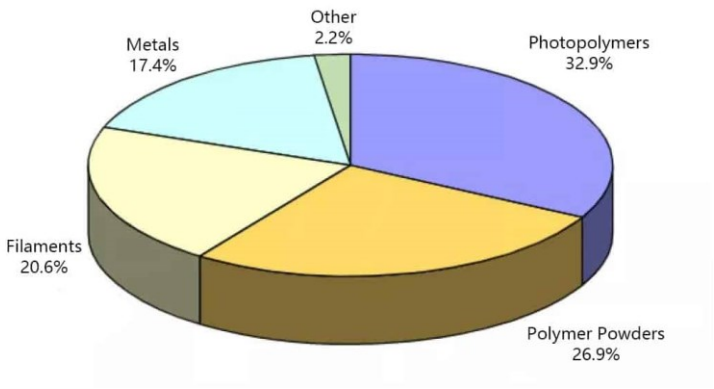

Figure 3. Popular materials used in AM technology [7].

Although some AM technologies, such as Laser Beam Powder Bed Fusion, Metal Selective Laser Sintering, Binder Jetting, and Electron Beam Powder Bed Fusion, can print metal materials, they still have significant weaknesses listed below:

- All these technologies use powder metal as their feeding material. The powder material is usually costly to prepare, and for some cutting-edge metals, there is even no proper powder form that can be used in AM.
- All these technologies require a high-cost equipment purchase fee. It is a burden for start-up companies before getting profit. Only large companies can purchase equipment on a large scale. This seriously damages the spreading of usage of metal AM and affects the development of metal AM technologies.
- Finally, but importantly, all these technologies cannot print large metal parts efficiently [9,10], meaning there is no proper metal AM technology that can make meter-scale dimension metal parts. The printing speed of these technologies is around 2 liters/hr for these technologies, which is low [11,12], and the Z-axis resolution of these technologies are in micron scale, as shown in Table 2Table 2. Common layer heights by technology [13]., indicating a low volume of material deposition [13]. People are looking for disruptive AM technology for efficiently processing large-scale metal parts.

Table 2. Common layer heights by technology [13].

Technology	Common layer thickness (micron)
FFF	50 - 400
SLA / DLP	25 - 100
SLS	100
Material Jetting	16 - 30
Binder Jetting	100
DMLS / SLM	50

1.4 Wire Arc Additive Manufacturing (WAAM)

Wire Arc Additive Manufacturing (WAAM) is an emerging AM technology that allows the fabrication of large-scale metal products with a high deposition rate and short production time [8]. WAAM is a collective terminology for all the processes that use an arc heat source to melt the wire to deposit metal material to fabricate the product in a layer-by-layer method.

A typical WAAM system comprises of a manipulator and an arc-based welding machine, as shown in Figure 4. The manipulator in WAAM is usually a robotic arm or a 3-axis CNC system that carries the welding torch as its payload. It executes the layer-by-layer tool path as defined by slicing software. The arc-based welding machine is a Gas metal arc welding (GMAW) or a Gas tungsten arc welding (GTAW) welding machine. The welding torch on the machine deposits the metal by continuously melting and depositing droplets from the tip of a metal wire along the printing trajectory to achieve layer-by-layer material deposition. Therefore, WAAM falls within the category of Direct Energy Deposition (DED). Meanwhile, based on its mechanism, WAAM technology is an desirable AM process that can contributing on solving the three weaknesses mentioned in Section 1.3.

First, due to WAAM implementing a welding arc as the heat source, the welding machine in WAAM is as same as the regular arc welding machine used in industry. Correspondingly, the formation of the feed metal material in WAAM is the same as the feed material used in regular industrial arc welding, metal wire. Therefore, there is a broadly available metal material used in arc welding that can be applied in the WAAM process.

Second, the manipulator and arc welding machine are easily accessible from the market at a low price. Besides that, the great replaceability can make the assembly of the WAAM system even more straightforward: any robot arm or a 3-axis CNC system combined with an arc welding machine can be a WAAM system. These features make the WAAM system accessible to small companies and academia.

Third, by taking upon the advantages of the tradition arc welding technologies, the material deposition rate in the WAAM process is up to 2.27 kg/h (for 1.2mm diameter stainless steel wire) [14]. This feature allows WAAM to deposit a large amount of material in a shorter time than other AM technologies, making building large-scale metal parts possible. Based on these features and advantages, WAAM is the most promising metal AM technology with widespread development [15].

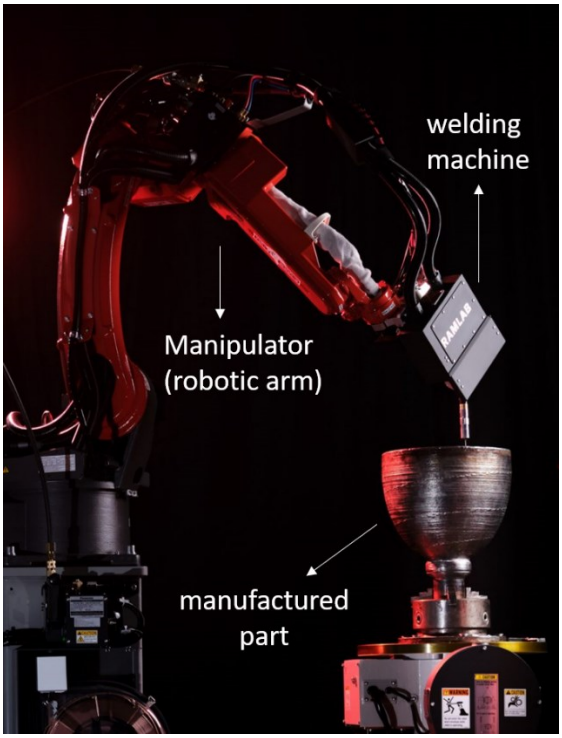

Figure 4. A typical Wire Arc Additive Manufacturing (WAAM) system *(RAMLAB, 2022)*.

1.5 Cold Metal Transfer (CMT)

Cold Metal Transfer (CMT) is a new welding technology introduced by Fronius in 2004. CMT originates from the short circuit transfer in GMAW technology. Therefore, CMT can be considered a variant of GMAW. CMT has been proven to improve product quality by taking advantage of low heat input [16,17]. CMT features a significantly lower energy input during the deposition process than other welding technologies. To achieve this feature, the CMT welding torch controls the oscillation motion of the wire. Instead of keeping the current and voltage at a constant level during the process like the traditional GMAW, the pulse current in CMT only exists for igniting the arc. The arc is then quickly extinguished just before the wire and molten droplet are pushed down into the molten pool. The voltage reduces to a low background value once the wire touches the molten pool and the short circuit happens. Finally, the wire is retracted from the molten pool, ready for the following pulse current. Figure 5 shows the wire motion in a single CMT cycle. shows the wire motion in a single CMT cycle. A completed CMT welding process is just the finite repetition of one cycle described above.

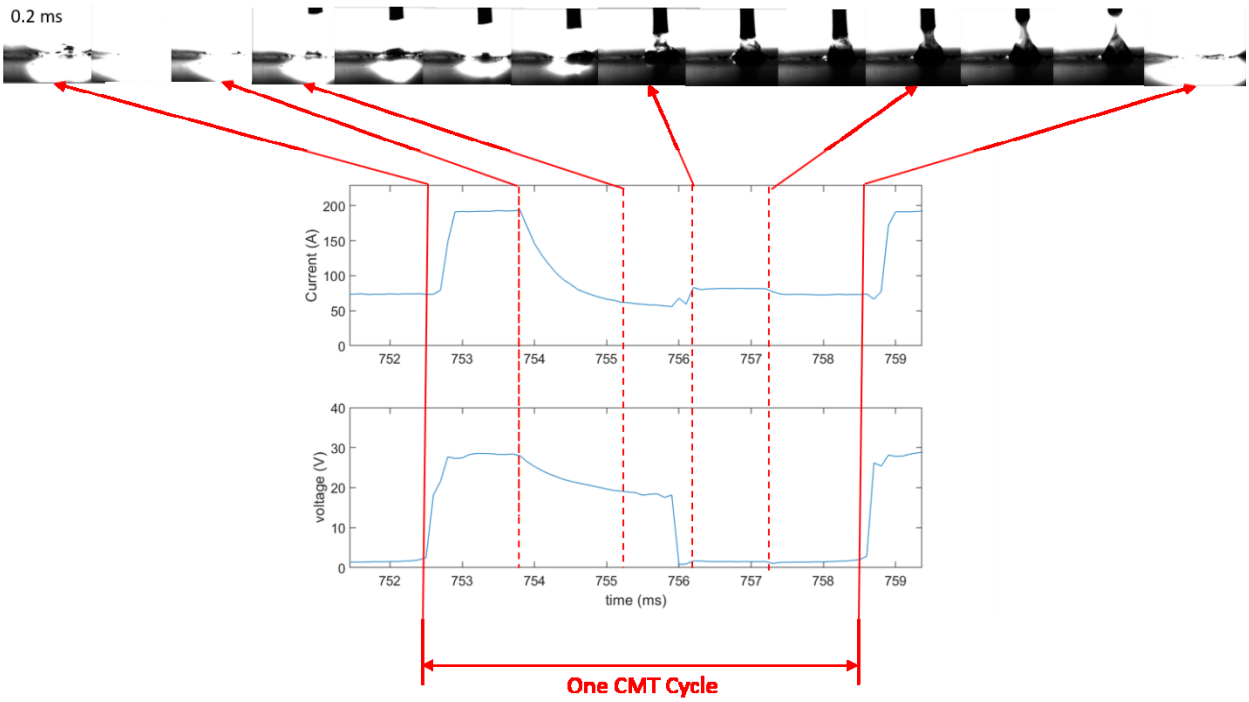

Figure 5. The wire motion in a single CMT cycle.

1.6 Aluminum Alloy in Wire Arc Additive Manufacturing (WAAM)

Aluminum alloys have been widely used in aerospace and automotive industries due to their low density, high chemical and erosion resistance, and high strength and thermal conductivity. CMT-based WAAM has been adopted for aluminum welding because its low heat input is suitable for welding low melting point alloys like aluminum [18–20]. Currently, 2xxx series [21], 4xxx series [22,23], 5xxx series [24], and 6xxx series [25] aluminum alloys have been investigated, and have been shown to be applicable in the GMAW-based WAAM process. However, an aluminum alloy that can be used in the WAAM process does not mean the parts made in this material are of good quality. Many factors may affect the process, leading to undesirable quality of the parts. Two of the most common problems of the as-printed part are the mechanical and geometric properties of the printed part. Although much research has been done to improve the quality of parts, most methods can only be applied in a laboratory type environment.

The 7xxx series alloy contains alloying elements of zinc, magnesium, and copper, usually used in aerospace applications that take advantage of its high strength-to-weight ratio [26]. 7xxx series aluminum alloy, therefore, has become popular in industry. However, the current industrial

manufacturing on the 7xxx series aluminum is still limited to subtractive manufacturing, typically the machining process. This is because the 7xxx series aluminum alloy is well-known as an unweldable material by conventional arc welding technologies such as GMAW or GTAW due to the solidification cracking (hot cracking) [27–29]. To make 7xxx aluminum weldable, NbC (niobium carbide) nano-treated 7075 aluminum alloy (AA7075) was made from MetaLi LLC. The composition of the 7075NT wire can be found in Table 2 below. This improved 7075 aluminum alloy has been implemented in practical welding works and has been shown to significantly mitigate the defects in welding 7075 aluminum alloy [30]. The study from Zuo et al. [30] is the first time the 7075NT wire was applied and had its weldability validated in WAAM. The emergence of WAAM technology gives a chance for manufacturing 7075NT aluminum alloys in a net-shape approach, which can result in significant material savings.

Table 3. Composition of the 7075NT wire

	Mg	Cu	Zn	Mn	Si	Fe	Ceramic	Al
7075NT	2.1 - 2.9	1.2 - 2	5.1 - 6.1	<0.30	<0.50	<0.50	0.4 - 1.2	bal

As mentioned, many traditional wire arc technologies are available for the WAAM process. Gas Tungsten Arc Welding (GTAW) and Gas metal arc welding (GMAW) are two common arc welding technologies to weld most carbon-based iron alloys [31]. These two welding technologies have been widely applied in WAAM, and sound 3D parts can be obtained using by this method [8]. However, for processing low melting point materials such as aluminum alloy, using GTAW-based WAAM and GMAW-based WAAM processes can be challenging due to the high heat input of the arc, which could over-melt the material, causing severe geometrical defects and undesirable mechanical properties during the printing [32,33]. By combining CMT welding technology with WAAM, the CMT-based WAAM can effectively print sound parts made of low melting point metals, for example, 7075NT.

1.7 Literature Review

A wide range of aluminum alloys have been investigated using WAAM. Yang et al. [34] successfully applied Cold Metal Transfer (CMT) based WAAM to printing AlSi7Mg0.6. Gierth et al. [24] fabricated AlMg5Mn using four different welding heat sources, GMAW, CMT, CMT-

ADV, and CMT-PADV, on fabricating AlMg5Mn alloy. Fu et al. [35] printed 2024 Al alloy via GTAW based-WAAM process and studied the effect of printing current on the porosity of the part. Gomes et al. [36] applied CMT, CMT-Pulse, and MIG-Pulse on WAAM to print the 6082 Aluminum alloy straight wall, followed by a comprehensive investigation of the product's quality. Ma et al. [37] combined GMAW based-WAAM and an industrial robot arm and realized the digital controllable printing process on 4043 Aluminum alloy. Ünsal et al. [38] also used an industrial robot arm but bonded it with a CMT heat source to deposit 6061 aluminum alloy.

So far, many attempts with various aluminum alloy and welding heat source combinations have been performed in WAAM to study the effect of these combinations on product quality. However, WAAM technology is still not mature. Every manufacturing process has its drawback, and WAAM is no exception. With a deeper investigation, some general defects that existed in the aluminum alloy WAAM-made part were found [9]. Residual stress, distortion, and deformation are the most common defects in the part [39,40]. Large thermal gradients during the printing, dwelling, and post-cooling process result in residual stresses due to the material's uneven expansion and exhibited as distortion and the poor geometrical properties of the part after the clamps are removed [37,41]. The degree of distortion and deformation of the WAAM-made part is essential to control because if the size and geometry do not fit the manufacturing requirement. Although post-heat treatment can release residual stresses, it costs time and money and sometimes may affect the mechanical properties or reduces the geometrical tolerances. Porosity is another common defect, especially for aluminum and titanium alloys [42]. Most of the pores in aluminum alloy parts are hydrogen pores which are formed due to the great difference in hydrogen solvability in the aluminum alloy during a fast-cooling process. Hydrogen solubility in aluminum decreases with decreasing temperature. Therefore, during a fast-cooling process, with decreasing solubility, the hydrogen is rejected from the solidified aluminum part to molten pool, forming pores if hydrogen cannot escape before aluminum solidifies. The pores in the part can seriously damage mechanical properties, such as strength and hardness. Humps and slumps (drippings) are common defects usually appearing in the horizontal deposition of the last bead in WAAM-made aluminum parts [43,44]. This phenomenon may be caused by the high temperature of the latest deposited bead, which affects the flowability of the molten pool of the current deposition [45,46]. The liquid molten pool then slumps down the two sides of the bead before solidifying, leading to a poor bead profile and affects the geometry of the part [47]. The accumulation of the poor bead profile can

influence the part's overall geometrical properties and surface finishing. Furthermore, the geometry of the first several layers are also undesirable. Especially for the first layer, the connection between the layer and substrate is narrow, which is called "neck connection" [48]. This defect leads to a low strength of connection between the part and the substrate. Also, it can lead to bad thermal conduction on transferring the heat of the part to the substrate. The defect maybe because of the high conductivity of the aluminum alloy. The heat of the deposited material is conducted to the aluminum substrate, causing a rapid solidification and forming neck connection [45].

All these common defects in WAAM-made aluminum products are more or less related to the processing temperature since the temperature is the reflection of the heat accumulation and dissipation from the part [49]. Hence, to get sound and defect-free part, an investigation into control of the temperature during the process is essential. It is possible to control the temperature and improve the quality by managing the heat of the part. Typically, heat management can be done through controlling heat accumulation and heat dissipation. In WAAM, the heat flux is determined by the difference in conduction through the part into the substrate, convection to the surroundings, and heat input from the welding arc. Pre-heating the substrate can reduce the temperature gradient, leading to a homogenized temperature distribution of the substrate. Therefore, residual stress and warping can be mitigated this way [50]. Pre-heating can also reduce the temperature difference between the substrate and molten material to increase the wettability of the deposited droplet [51]. The primary heat input during the process is the heat flux from the welding arc, which is controlled by the welding current voltage and printing speed (torch travel speed). This can lead to a change in the part's size and dimension stability [22,48,52,53]. In addition, the heat input from the arc is absorbed by the part and the absorbed heat is conducted to the rest of layers. Therefore, the heat input from the arc drastically influences the cooling cycle of each layer in the process, similar to an in-situ heat treatment, and the microstructure changes as a result. With a fixed cooling duration between the latest deposited layer to the next layer, the heat dissipated via convection cannot compensate for the increased magnitude of the heat input when the deposited number of layers keeps increasing. The balance of heat input and heat dissipation is therefore broken.

During the WAAM process, the amount of heat from the arc usually greater than the amount heat dissipated from the part to the environment via conduction, convection, and radiation, causing heat

accumulated inside of the part. A good way to mitigate the heat accumulation in the part is increasing the heat dissipation, . Passive cooling is a process that can increase convection heat flux to the environment. The most common and easily applied passive cooling method is setting the dwell time. Dwell time is defined as the idle time between each subsequent layer. This method allows the part to cool down via heat convection, conduction, and radiation to ensure the part has a lower overall temperature before the next layer. This is a method to avoid heat over-accumulation [54–57]. Another cooling method is the active cooling (compulsory cooling). Contrary to the passive cooling process, it increases the convection surrounding the part resulting in a higher cooling rate of the part. Bai et al. [50] designed an advanced in-situ cooling apparatus, a symmetrical aluminum heat sink mounted on the two sides of the part to absorb the heat from the part and convey the heat to the environment. The result shows the as-printed wall has better homogeneous geometry than with the use of natural heat convection. However, this method can only be applied when printing simple shape parts. The air-jet cooling is a other active cooling method that increases the convective heat transfer between the part and the environment by mounting a high-pressure air jet on the welding torch [58]. The output, via this method, has improved the geometrical properties. Liquid cooling integrated fixture plate and Liquid cooling integrated substrate are two active cooling methods can absorb a large amount of heat through heat conduction by using a liquid with a high specific heat liquid (usually water or nitrogen) to increase the cooling rate [44,59]. These two methods have better cooling efficiency than other methods but are limited to fabricating the part with complicated shape, because it is difficult to make a large heat ink that can mounted on the two sides of the unregular shape of wall. Although either passive cooling or active cooing has ability to mitigate the heat accumulation in parts to improve the part's quality.

1.8 Motivation and Research Objective

1.8.1 Motivation and Challenges in WAAM process with 7075NT aluminum alloys

The challenges to reliably building components in aluminum using WAAM are:

- Aluminum is sensitive to the process temperature leading to hydrogen saturation.
- The geometrical properties of the WAAM-made aluminum alloy parts are undesirable because of the process' high heat input and heat accumulation.

- The suitable processing parameters are still unknown for additively fabricating 7075NT aluminum alloy.

Using CMT as the power source for WAAM of 7075NT will help control cooling rate and improve the geometry and metallurgy of the part. Currently, there are no published documents or papers focusing on solving these problems. Therefore, a topic covers and investigates on the solutions of these three issues would be valuable.

1.8.2 Research Objectives

This research aims to comprehensively investigate the process and the control of the quality of nano-treated 7075 aluminum alloy parts manufactured using an in-situ multi-sensor WAAM system. To reach this goal, the research consists of three parts: "WAAM In-situ Multi-sensor Monitoring System Setup," "Process Parameters Exploration," and "Heat Management and Quality Control."

In the "WAAM In-situ Multi-sensor Monitoring System Setup" section, three sensor modules are integrated into the in-house WAAM system and the accurate emissivity of 7075NT aluminum alloy is calibrated to obtain the correct temperature from an infrared (IR) camera. In the "Process Parameters Exploration" part, the energy feature of CMT in 7075NT aluminum alloy and the most suitable parameter for fabricating the 7075NT aluminum alloy are explored. In the "Heat Management and Quality Control" section, two heat management strategies are applied to the WAAM process to control the geometrical and mechanical properties. The five sub-studies listed in Figure 6 correspond to the three aforementioned sections.

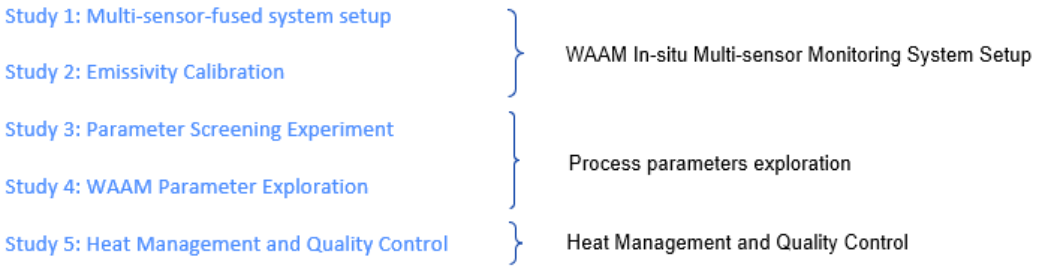

Figure 6. The sub-studies and their classification.

2. Setup of the sensor-fused CMT-based WAAM system

2.1 Introduction

As mentioned in Section 1.7, the temperature of the part during the process plays a significant role in the quality of the CMT-based WAAM-made 7075NT aluminum alloy part. The processing temperature will be measured and recorded to understand cooling rate of the system. To achieve this, an in-situ multi-sensor monitoring WAAM system is necessary. The system integrates different types of sensors so that the system can collect geometry and temperature information during the printing process. Unfortunately, this intended multi-sensor WAAM system does not exist yet. Although some researchers have applied profilometer sensors [26][52] and thermal sensors in other AM systems [27][44], those are not fully integrated. Moreover, rather than measuring and recording the interpass temperature and geometry information for each of layer, those sensors can only measure and record the temperature and geometry information for the overall wall after the printing process. The sensors intended to be used in the WAAM process must also be carefully considered for their inherent limitations. For instance, thermocouple or thermistors are commonly used in measuring temperature. They are usually classified in the contactable static sensor category, meaning they must be fixed and can only measure a spot temperature. However, in the AM process, sticking a contactable thermal sensor and running a measurement on a part that has not been printed out yet is hard to accomplish. Furthermore, the severe high-temperature welding environment in the WAAM process makes those sensors hard to adhere to the part, leading to inaccurate data. Therefore, an in-situ multi-sensor monitoring WAAM system is urgently needed.

In this study, an in-house in-situ multi-sensor monitoring WAAM system (referred to as WAAM system), shown in Figure 7, was built with the ability to conduct the WAAM process and execute in-situ monitoring and recording on the temperature and geometry of the printed part.

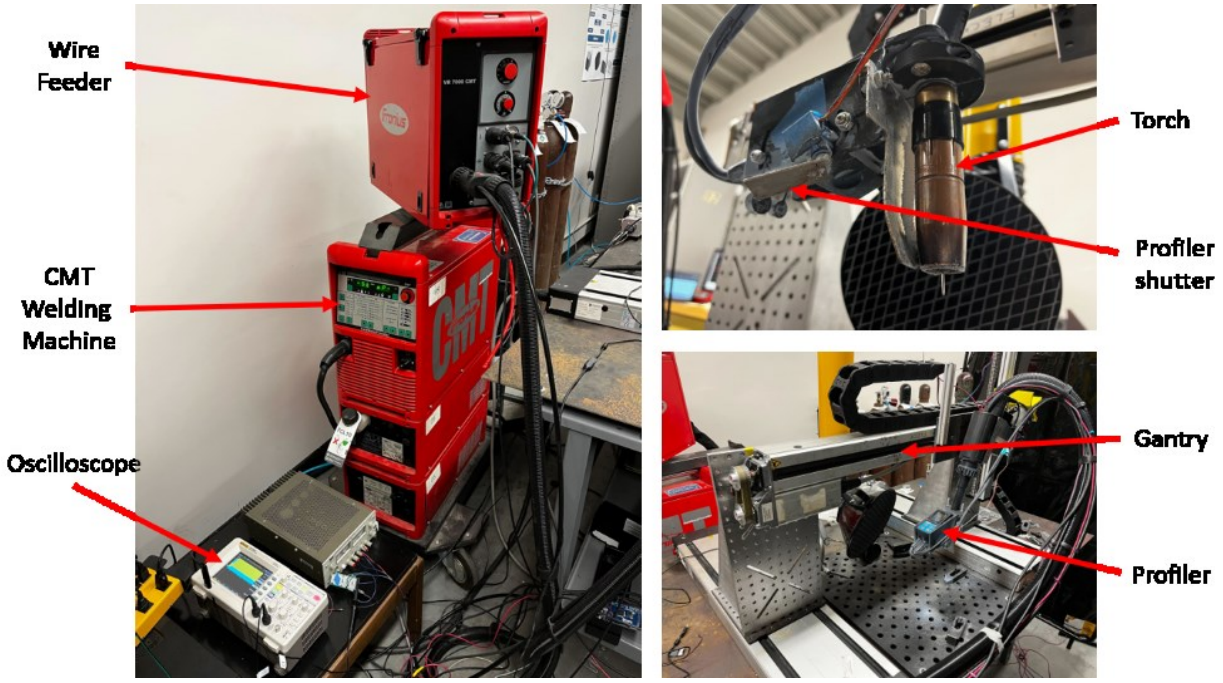

Figure 7. The physical setup of the WAAM system.

This in-situ multi-sensor monitoring WAAM system is comprised of a deposition module and a monitoring module. The structure of the system is shown in Figure 8.

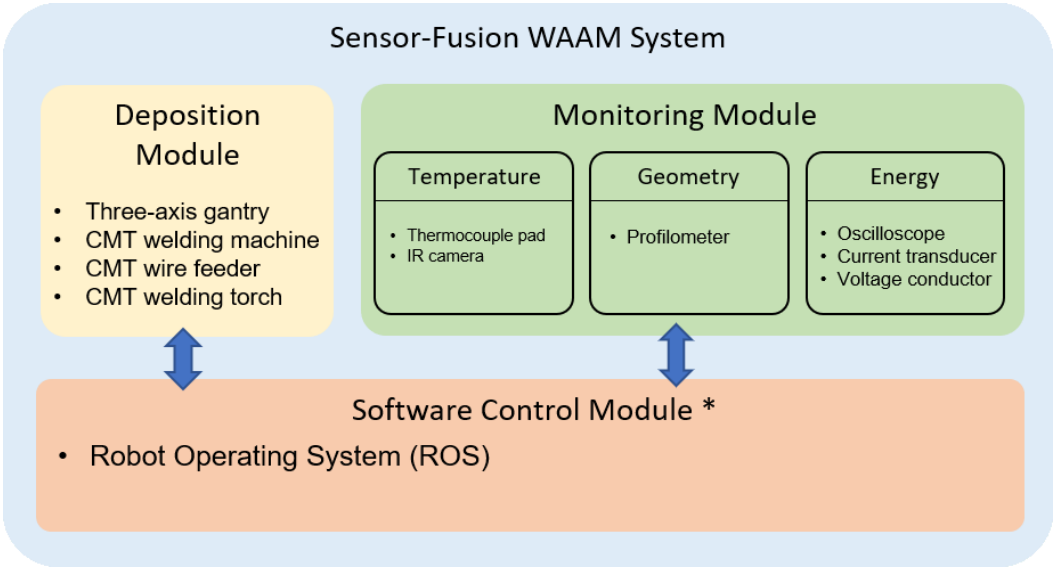

Figure 8. The structure of the sensor-fusion WAAM system.

2.2 The Setup of the Deposition Module

The deposition module is the essential part of the system that takes charge of depositing metal material to fabricate the three-dimensional object. This module includes a three-axis gantry, a Fronius TransPlus Synergic 5000 CMT welding power supply, a Fronius VR 7000 CMT wire feeding unit, and a Fronius Robcata welding torch. The three-axis gantry, comprised of two X-axis sliders, a Y-axis slider, and a Z-axis slider, is shown in the bottom right sub-plot in Figure 7. This gantry allows the WAAM system to print parts as large as 450x450x350 mm. The Fronius TransPlus Synergic 5000 CMT welding power supply is designed especially for the CMT process. The Synergic Line can accurately control the current and voltage based on the material, Synergic Line, and the Contact Tip to Welding Piece Distance (CTWD) in a millisecond to ensure a stable arc is generated during the smooth welding process. The Fronius VR 7000 CMT wire feeding unit is loaded with a regular welding spool and the torch contains a wire buffer that can precisely control the periodical movement of the tip of the wire (in the contact tip) to control the material transfer behavior (globular, spray, and shortcut). The Fronius Robcata welding torch is mounted on the Z-axis of the three-axis gantry. In this study, the torch's nozzle is perpendicularly fixed towards the substrate to ensure the material is deposited vertically.

2.3 The Setup of the Monitoring Module

The monitoring module includes three sub-modules for in-situ measuring and recording the building part's temperature, layer contour, and energy input, respectively. The thermocouple pad was made by integrating 16 K-type thermocouples into a 35mm steel pad for measuring and recording the substrate temperature at a recording frequency of 5 Hz. Figure 9 is the schematic of the design of the thermocouple pad. Before printing, the aluminum substrate is clamped on the top of the pad tightly to guarantee all 16 thermocouples contact the aluminum substrate. An Optris Xi 400 IR camera with an 18° lens was applied with a measurable temperature range from 150℃ to 900℃, providing a 382 by 288 pixel frame with a recording frequency of 50Hz. The spectral range of Xi 400 IR camera is ranges from 8 - 14 μm. The IR camera is aligned to the tip of the welding torch in order to measure and record the interpass temperature during the printing, as shown in Figure 10. Both the IR camera and welding torch were mounted on the Z-axis slider, moving synchronously. Therefore, the distance between the IR camera and the tip of the welding torch is

kept constant to avoid an out of focus IR image. A SICK ProfileTM 2 profile meter sensor (referred to as profiler) was horizontally mounted on the torch, as shown in the top right sub-plot in Figure 7, to scan the new layer's contour immediately after the new layer is deposited. The vertical distance from the profiler's laser sensor to the tip of the wire is 50mm. For the purpose of protecting the sensor in the profiler from the high-intensity arc radiation and filtering the noisy reflected light coming from the welding arc during the process, a physical shutter driven by a servo motor was designed and mounted on the front of the profiler's sensor. When the CMT welding arc is turned on, the shutter closes; when the arc is off, and the scanning of the contour of the layer is needed, the shutter opens. The welding current and voltage must be recorded to obtain the heat input during the process. The current was collected by the LEM 505S current transducer surrounding the ground cable, and the voltage was collected by the copper wire conductor between the torch and fixture plate [60]. The current transducer and wire coil are connected to the ROGAL E1306 oscilloscope to record the measurement data with a frequency of 50Hz. The schematic of the physical connection of the transducer, wire conductor, and an oscilloscope is shown in Figure 11.

In this Sensor-fused WAAM system, both the deposition module and a monitoring module are integrated with the Robot Operating System (ROS) based AM toolchain. The toolchain generates a customized printing path that the three-axis gantry can execute. The customized path is first written in the format of code. Then the code is fed into the ROS-based AM toolchain that interprets the code as a trajectory that the three-axis gantry is able to recognize. After that, the three-axis gantry reads the trajectory and executes the print command. Meanwhile, the toolchain is competent in collecting the data from the sensors set up in the system by grabbing the data stored in the sensors' buffer during the processing and can save that data in a CSV file for the convenience of the data post-processing and analysis.

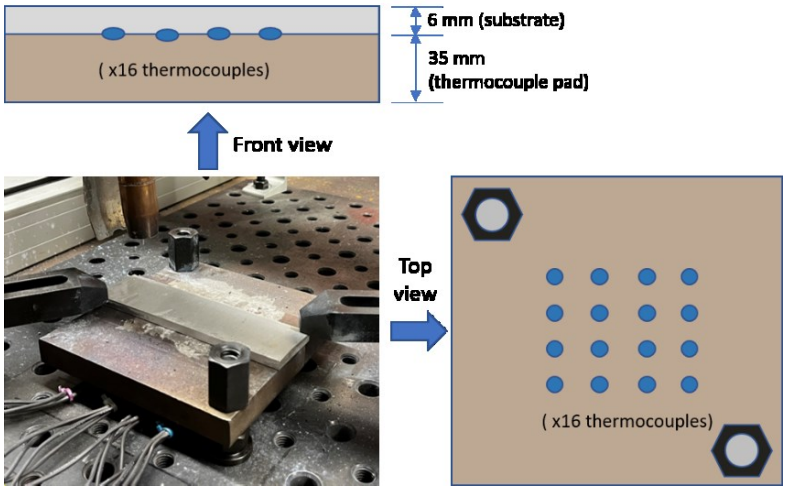

Figure 9. The design of the thermocouple pad.

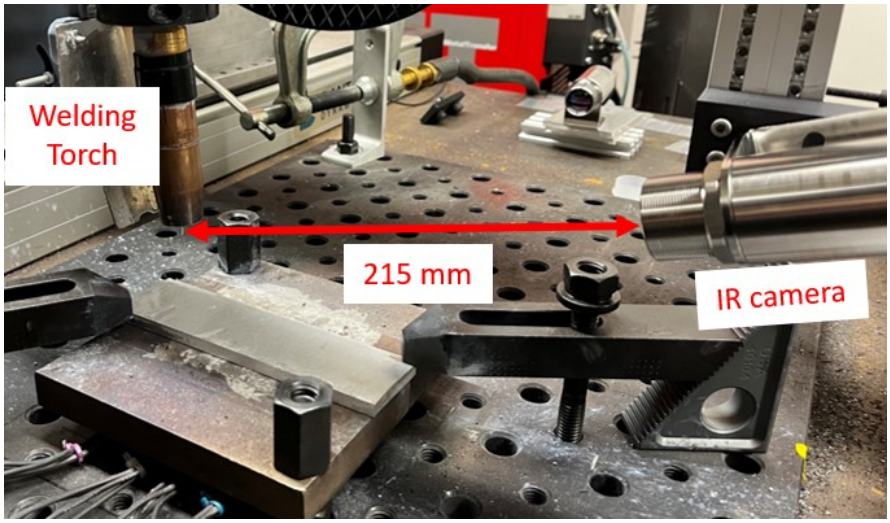

Figure 10. The setup of the IR camera.

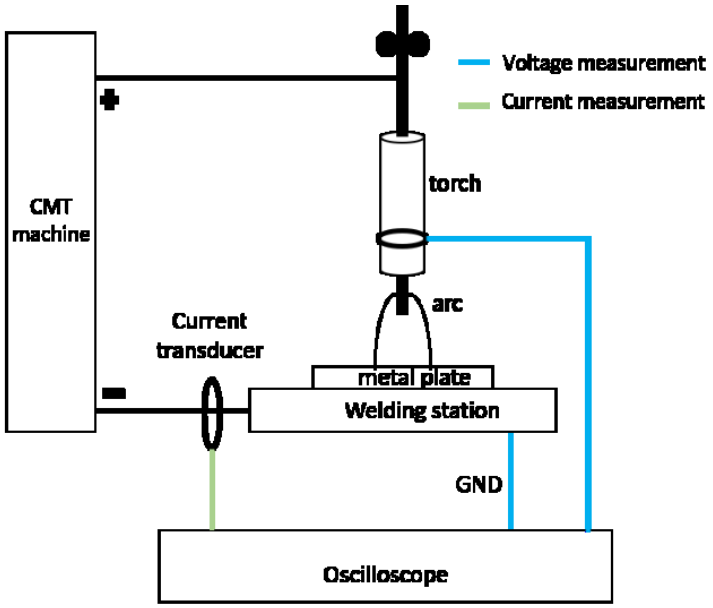

Figure 11. Current and voltage measurement setup.

3. The Emissivity Calibration on the WAAM Manufactured 7075NT Aluminum Alloy Part

3.1 Introduction

Aluminum alloys are one of the most popular materials used in aerospace industry due to their light weight, chemical and corrosion resistance, and excellent thermal and electrical conductivity properties. More and more WAAM applications fabricating aluminum alloy prototypes are appearing in the aerospace and automotive industries [8].

However, using WAAM to fabricate aluminum alloys suffers from undesired product qualities, such as high residual stress, distortion, solidification cracking, and high porosity, which sharply reduce the mechanical and geometrical properties of the part [9]. Many efforts have been made to resolve these defects. It is has been found that the heat accumulation and heat dissipation reflected as temperature during the WAAM process can be significant factors in the formation of these defects [48,52,61,62]. Therefore, an accurate in-situ temperature measurement is required. Geng et al. and Gierth et al. [24,45] used thermocouples in WAAM to measure and record the process temperature. However, this method can only measure the spot temperature and is limited by the complex mounting procedure. On the contrary, contactless infrared (IR) temperature measurement devices can measure and record the temperature without physically touching the target surface, bringing considerable ease of use and setting flexibility. IR devices such as infrared (IR) cameras and pyrometers have been used in WAAM to measure the thermography and spot temperature, respectively [19,55].

One of the critical parameters for obtaining accurate temperature from IR devices is the correct emissivity. Without obtaining the correct emissivity of the target object, the infrared radiation captured by IR devices cannot be converted to accurate temperature information. In practice, the emissivity is not constant but varies depending on many factors which relate to temperature, surface treatment, viewing angle, and wavelength [63–66]. The detailed descriptions of these factors and their effect on emissivity are listed in Table 4. Besides these factors, the aluminum part manufactured by the WAAM process has a distinct oxidation coating on the part's surface, which also drastically affects the emissivity of the aluminum part, preventing the measurement of

accurate temperature data by the IR camera [64,67–69]. Emissivity measurement is necessary before using an IR camera for temperature measurement on the WAAM-made part.

Table 4. The factors that affect emissivity.

Factor	Description	Reference
Temperature	The temperature of the target object	[63,70–72]
Surface Condition	Surface roughness and oxidization	[64,67–69]
Viewing Angle	The angle between the camera's current position and the normal of the target's surface	[65,73]
Wavelength	The wavelength of the spectral radiation emitted from the target object	[66,70–72]

Some approaches are available to obtain accurate emissivity, and the most common one is checking the lookup table compiled by IR device manufacturers or authority institutions. However, this approach is not adequate for the accuracy required for lab research and industrial manufacturing because it has been proven that emissivity can be greatly affected by complicated on-site experimental conditions such as the infrared reflection or the multi-heat-source. More importantly, the lookup table does not include the emissivity of cutting-edge materials like the aluminum 7075NT used in this study. Therefore, the emissivity of the target object should be tailored by taking into account the specific material and processing conditions.

Some researchers have explored the relationship between emissivity and the factors listed above. Lanc et al.[74] studied the emissivity of AW6082 aluminum alloy using an infrared camera on different surface quality and temperature of workpieces, concluding that the emissivity of aluminum alloys declines with increasing temperature in the temperature range from 50 to 200°C. Furthermore, they found that the emissivity decreases with increasing roughness from 1.07 to 1.77 μm in the spectral range from 8 to 14 μm. Wen et al. [67,75] examined the emissivity of 1100, 7150, 7075, and 2024 aluminum alloys. Each sample's surface was polished to a different surface roughness. The emissivity of these samples was then examined over the spectral wavelength range of 2.05 to 4.72 μm at 600, 700, and 800 K. The results showed aluminum alloys usually have an

emissivity of 0.15 at the polished surface (0.08 μm roughness) and 0.3 at a comparatively rough surface (2.90 μm roughness) and decrease with the decrease of the temperature and wavelength.

7xxx series aluminum alloys (Al-Zn-Mg-(Cu)) have the highest strength of all aluminum alloys. As the most common 7xxx series aluminum alloy, 7075 aluminum alloy has been widely used in the aerospace industry. However, 7075aluminum alloy is known to have issues related to weldability by arc welding because of hot cracking and stress corrosion [76]. The nano-treated AA7075 (7075NT) wire (MetaLi LLC, USA) improves weldability by adding ceramic particles to the conventional 7075 material. 7075NT wire has been implemented in practical welding works and has been proven to significantly mitigate the defects in welding 7075 Aluminum alloy [30,76].

Based on the current research, there is limited information available on the emissivity of aluminum alloys and the relationship between the emissivity and its influencing factors. However, for aluminum parts produced by WAAM, the emissivity will changes since additively manufactured parts' surfaces feature periodic bumps and grooves, which is a consequence of layerwise fabrication, exhibiting a pronounced surface waviness [77–79]. Moreover, during the WAAM process with aluminum alloy, a thick oxidized layer is generated and deposited on the surface [80]. Both the pronounced surface condition and oxidization layer are two characteristics of WAAM-made aluminum alloy parts, and these factors affect emissivity. Therefore, this study aims to examine the relationship between the emissivity of additively manufactured 7075NT aluminum alloy and surface texture, temperature, IR camera's viewing angle, and surface condition. The emissivity for each factor was calibrated during a continuous air-cooling process to obtain the emissivity gradient along the temperature. Finally, regression models were built with high fitting accuracy for predicting emissivity.

3.2 Experiment setup and design

3.2.1 Experiment Setup

An additively manufactured part made through WAAM exhibits an undulating surface due to layer-wise deposition. Thus, distinct sets of parameters were used in the WAAM process to generate parts with different surface textures. A total of 13 single-track multi-layer 7075NT aluminum alloy walls were printed with different parameter sets. The parameter sets were designed

by Minitab 19 (Minitab LLC, USA) software, as listed in Table 5. These parameters and their range are chosen by previous pilot experiment.

Table 5. Printing parameters and surface texture (Sq)

Wall	Arc Correction	Gas Flow Rate (CFH)	Pre-heat temp (℃)	Inter-pass Temp (℃)	WFS (in/min)	TS (in/min)	Sq (mm)
1	10	20	120	350	200	8	0.22
2	0	50	120	500	200	20	0.2
3	10	20	20	500	160	20	0.14
4	10	50	70	500	120	8	0.23
5	0	35	70	350	160	14	0.12
6	-10	20	120	500	120	14	0.23
7	-10	20	70	200	200	20	0.19
8	-10	50	120	200	160	8	0.39
9	-10	50	20	350	120	20	0.24
10	10	50	20	200	200	14	0.17
11	10	35	120	200	120	20	0.18
12	0	20	20	200	120	8	0.3
13	-10	35	20	500	200	8	0.34

To obtain the surface texture of the printed wall, a Profiler TM 2 (SICK, USA) sensor was used to scan the topography of a 12mm by 15mm area at the center of the wall surface, as shown in Figure 12 (a). The Y-axis is the printing direction, and the X-axis is the building direction of the wall. In this study, the influence of surface texture is investigated instead of surface roughness. Thus, based on the ISO 25178-2 standard, an S-filter with a cut-off wavelength of 0.8mm is applied to the scanned topography to remove small-scale components from the topography and remaining surface texture [81]. The Root Mean Square Height (S_q), which is the square root of the mean square of the ordinate values of the surface topography defined in the ISO 25178-2 standard, is used to quantify the surface texture in this study. The workflow of surface texture extraction is shown in Figure 12. The S_q of each wall surface was calculated and listed in the last column in Table 5.

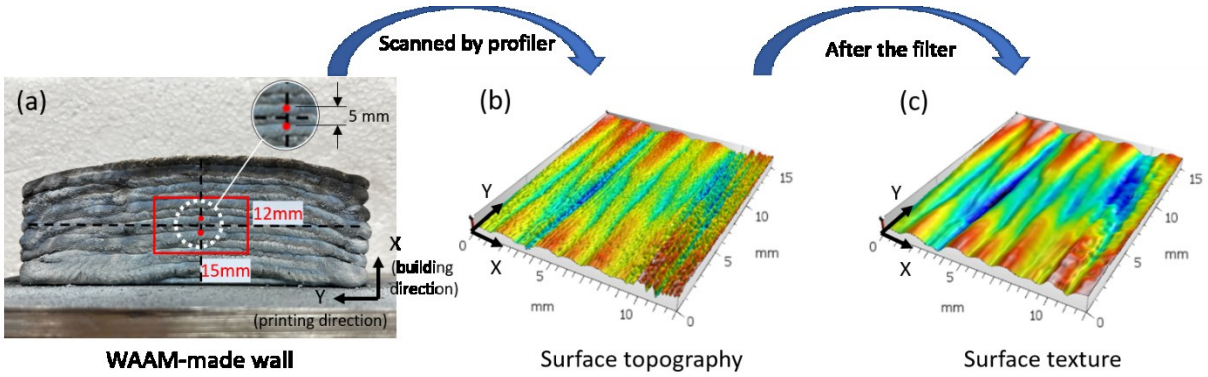

Figure 12. Surface texture extraction workflow. (a) The location and size of the scanning area on the WAAM-made wall. (b) The profiler scans the surface topography. (c) The surface texture after applying the filter.

Figure 13(a) illustrates how the contactless infrared monitoring device was mounted for capturing the thermography at different viewing angles. An Optris Xi400 (Optris, Germany) infrared (IR) camera with a 30° lens and 200℃ to 900℃ measurement range is applied in this study. The IR camera was horizontally mounted 330mm away from the wall. A rotatable platform was designed to rotate the wall around the vertical centerline at the desired angle. The angle between the IR camera's facing direction and the wall's normal is defined as the viewing angle. During the measurement, the wall's vertical centerline was always aligned with the pivoting axis of the rotatable platform. The IR camera and rotatable platform were set up in an opaque black box to avoid external infrared interference during the measurement.

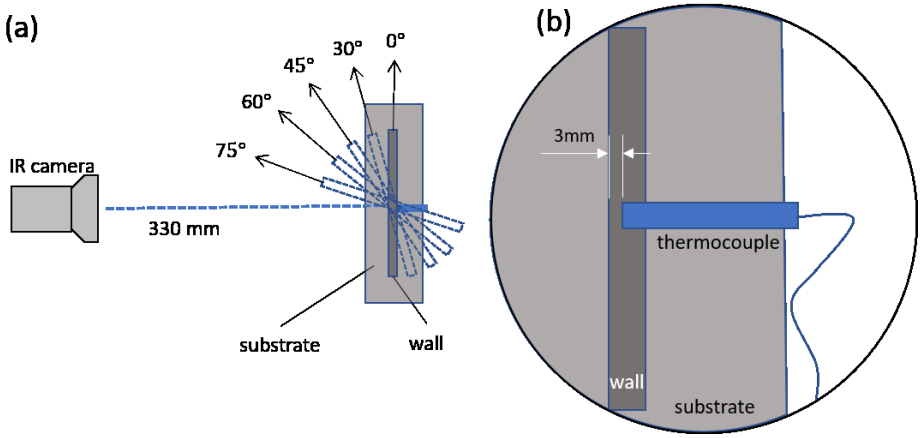

Figure 13. (a) The top view of the five different viewing angles. (b) The setup of thermocouples.

Emissivity is usually examined for calibrating the thermography or thermo-video when an IR camera is applied. The emissivity is defined as the ratio of the true temperature of the target to the thermography temperature that the IR camera captures [74], which can be expressed as:

$$\varepsilon = \frac{T_{IR}}{T_{True}} \quad (1)$$

Where ε is the emissivity, T_{IR} is the temperature that the infrared device captured, and T_{True} is the real temperature of the target's surface [55]. Eq (1) is used for calculating the emissivity in this study. In order to measure and record T_{IR} and T_{True}, an IR camera and two thermocouples were used in this study, similar to the methods used in Nunak et al. [65]. The IR camera recorded the temperature of the wall's surface at a recording frequency of 5Hz. Emissivity was set as 1 in the IR camera during the measurement. The mean temperature of the area, which is the exact same area the profile meter scanned through the red rectangle in Figure 12 (a), was extracted by IR camera. The temperature in the extracted area was marked as T_{IR}. Correspondingly, two K-type thermocouples were used to record the actual temperature (T_{True}). Figure 12 (a) illustrates the position of two thermocouples which were aligned to the vertical centerline of the samples 5 mm apart and were symmetrical with respect to the horizontal centerline of the wall. Figure 13 (b) shows the zoomed top view setup of two thermocouples. The thermocouples were inserted from the back face of the wall until the distance between the tip of the thermocouple and the front face of the wall was 3mm in order to minimize the effect of the temperature gradient caused by the wall thickness. The mean temperature from two thermocouples was used as T_{True}. To examine the emissivity gradient, the continuous T_{IR} and T_{True} need to be recorded during continuous cooling. To obtain this gradient, the wall was heated up to 450℃ in a furnace. Then, the part was placed outside the furnace in a stable lab environment and the thermocouples were inserted. The IR camera then was set to record T_{IR} and T_{True} during air-cooling.

In order to ensure the wall does not melt or soften, the maximum heating temperature had to be carefully decided. ThermoCalc was used to determine the liquidus temperature of 7075NT. The liquidus was found to be 510℃ as shown in Figure 14. To guarantee the temperature fluctuation of the furnace did not exceed the liquidus temperature, a maximum heating temperature of 450℃ was assigned.

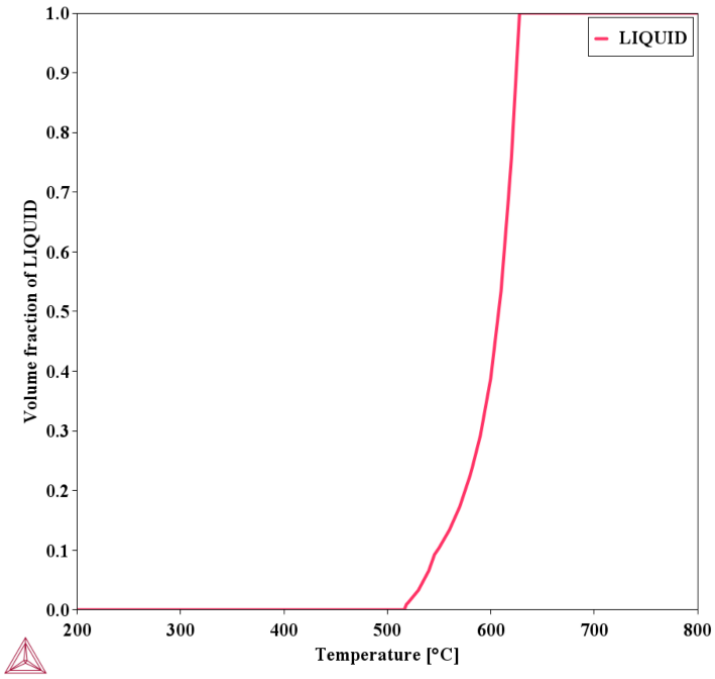

Figure 14. The volume fraction of liquid of 7075NT with respect to temperature..

3.2.2 Design of Experiment

Three experimental groups were designed in this study to investigate the effect of surface texture, viewing angle, temperature, and surface coating on emissivity. Groups 1 and 2 are shown in Table 6, and Group 3 is shown in Table 7. In Group 1, the viewing angle was fixed to 0° (the IR camera faces the normal of the wall). Five levels of surface texture Sq, 0.39, 0.30, 0.24, 0.18, and 0.12, were picked from the walls corresponding to numbers 8, 12, 9, 11, and 5 in Table 5. These five values are in approximately 0.6 intervals between each other and cover the span of the values of surface texture measured in 13 printed walls. In group 2, the surface texture was set as 0.24, which is the median value of the five texture levels assigned in Group 1 while the viewing angles were set to 0°, 30°, 45°, 60°, and 75°. The detail of Group 1 and Group 2 are listed in Table 6.

Due to the lack of data on the emissivity of additively manufactured 7075NT aluminum alloy parts, this study also intends to examine the emissivity of the different surface conditions. Group 3 was designed, including Trials 11, 12, 13, and 14, for examining the emissivities of the raw surface, finished surface, oxidized surface, and carbonized surface respectively. The raw surface in Trial 11 was treated by removing all surface films and impurities, retaining the original surface texture

of the additively manufactured wall. On the contrary, the finished surface in Trial 12 is machined from the raw surface by milling and polishing to remove surface topography. Moreover, it can be observed that the wall made by 7075NT aluminum alloy is covered by an oxidized and a carbonized coating, in sequence. More detail on these two coatings can be found in Section 3.3. The oxidized and carbonized coats may also affect the emissivity. Therefore, Trial 13 and 14 were designed to investigate the carbonized and oxidized surfaces, respectively. Herein, the oxidized surface is the wall's original surface without any surface condition. In contrast, the carbonized surface is obtained by using a wet paper towel to carefully sweep the oxidized film off. The three treated surfaces (raw, finished, and carbonized surfaces) and an original surface (oxidized surface) in Group 3 were established on a separate wall with a surface texture Sq equal to 0.31. The emissivity in all three groups was examined during the continuous air cooling from 360℃ to 150℃. Because T_{True} cannot be read during the continuous air-cooling, both T_{True} and T_{IR} began to be collected when the real-time T_{IR} was lower than 360℃ and stopped recording when real-time T_{IR} reached 150℃.

Table 6. The detail of experiment Group 1 and Group 2

Group	Trial	Sq (mm)	Viewing Angle (°)
1	1	0.39	0
	2	0.30	
	3	0.24	
	4	0.18	
	5	0.12	
2	6	0.24	0
	7		30
	8		45
	9		60
	10		75

Table 7. The detail of experiment Group 3

Group	Trial	Surface Conditions	Sq (mm)	Viewing Angle (°)	Temperature (℃)
3	11	Raw	0.31	0	200℃ to 100℃
	12	Finished	-		130℃ to 90℃
	13	Carbonized	0.31	0	360℃ to 220℃
	14	Oxidized	0.31		360℃ to 220℃

3.3 Result and Discussion

3.3.1 Effect of Surface Texture and Temperature on the Emissivity

Based on Group 1, the emissivity with different surface textures during the continuous cooling process was examined and plotted in Figure 15. The chart shows the maximum, minimum, median, mean, and standard deviation trends of the emissivity at each surface texture level.

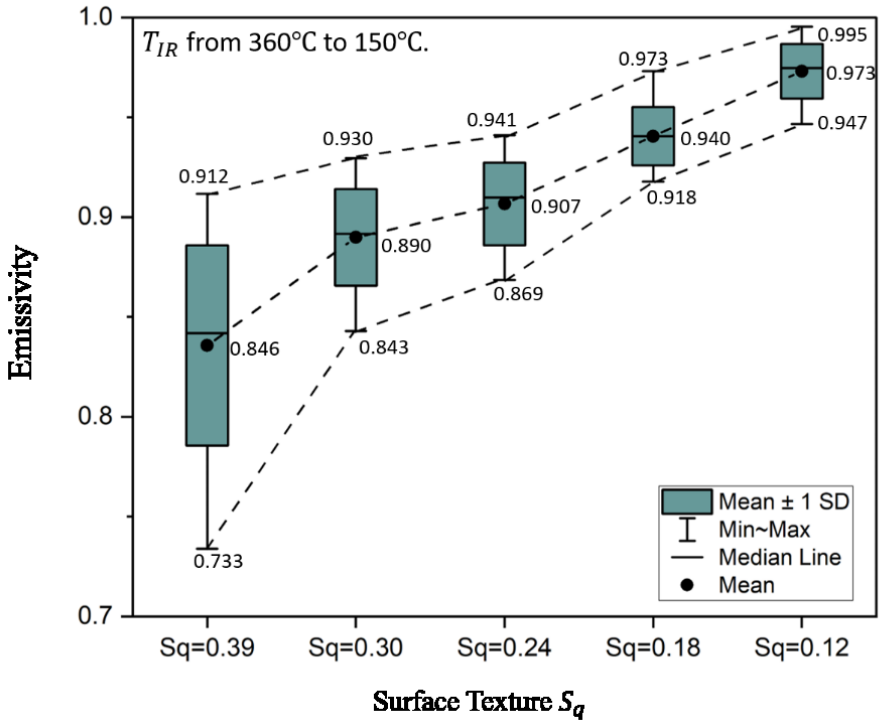

Figure 15. The emissivity examined at five different surface texture levels.

The maximum and minimum values at each surface texture level represent the highest and lowest emissivity during the cooling process. Although the different surface texture levels result in distinct maximum and minimum emissivity, there is still a strong emissivity pattern that can be traced in the chart where both maximum and minimum emissivity increase with the decrease of the surface texture. The maximum emissivity reaches 0.995 at the finest surface texture Sq=0.12, and the minimum emissivity reaches 0.733 at the roughest texture Sq=0.39. Besides that, due to the minimum emissivity increasing faster than the maximum when surface texture increases, the difference of the extreme emissivity values, called the span of the emissivity gradient, decreases when the surface texture is finer.

The median and mean emissivity in the chart exhibited another pattern. The median and mean emissivity values are noticeably close to each other at all textures meaning that the emissivity has a symmetrical distribution. The rectangle bars in the chart are the ± 1 standard deviation of the mean, meaning 68% of the emissivity values are included in the green bar. From the chart, the shrinking green bar and the decreasing surface texture indicate that the emissivity is concentrated in a narrow numerical band at a finer texture. Therefore, by going through the entire chart, two clear and recognizable patterns can be concluded. First, the emissivity increases when the surface texture decreases. Second, the range of the emissivity gradient becomes narrow, and the distribution of the emissivity values during the continuous cooling process converges when the surfaces become finer.

According to the examined result, it is clear that surface texture significantly affects emissivity. To investigate the mechanism of influence of the surface texture, a guiding hypothesis can be made that the emissivity change is due to the layering effect of the surface texture. This hypothesis is based on the existing radiation trapping theory that the trapped radiation keeps reflecting inside the groove and is finally absorbed by the part itself. Only a portion of radiation escapes from the groove and is captured by the IR camera [82]. The temperature recorded by the IR camera from the radiation is proportional to the radiation intensity. Thus, the depth, size, and amount of the side profile of the layer on the part's surface affects the intensity of the emitted radiation and the amount of the radiation the IR camera captures, further affecting the temperature the IR camera records and further affects the calibration of emissivity.

WAAM fabricates the product in a layer-by-layer method, forming the periodic rippled or undulating waviness along the building direction, as shown in Figure 16. Grooves are formed between two layers which may trap the radiation. To validate the hypothesis presented in the last paragraph, the 2D surface topography is decoupled into two orthogonal directions: horizontal and vertical, corresponding to the printing direction and building direction. The surface profiles and the temperature profiles along these two orthogonal directions are then extracted. Figure 17 (a)-(e) shows the topography and temperature profile information of each sample. The color map at the bottom left in each sub-plot in Figure 17 is the topography of the scanned surface area. The topography map has the same coordinate origin as in Figure 12 (a). The profile next to the right side of the topography map is the mean vertical profile which is the average of the vertical waviness of the surface (Y-axis). The rightmost diagram includes three temperature profiles, extracted from the IR camera's thermography, captured at temperatures of 360℃, 260℃, and 160℃ during the continuous air-cooling process and averaged through the Y-axis. The two diagrams at the top of the topography map are also the surface and temperature profiles, but they are averaged along the horizontal waviness of the surface (X-axis). The topography map's vertical profiles on the top side include the surface and temperature information along the wall's building direction. In contrast, the horizontal profiles on the top of the topography map include the surface and temperature information along the printing direction.

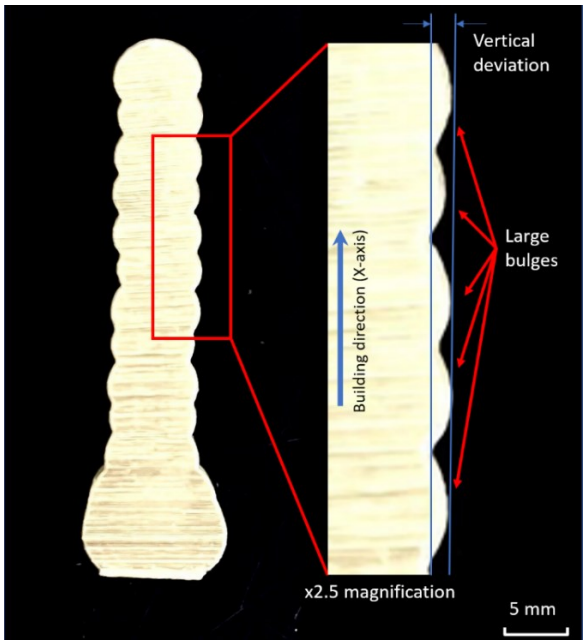

Figure 16. The cross-section of the WAAM-made wall.

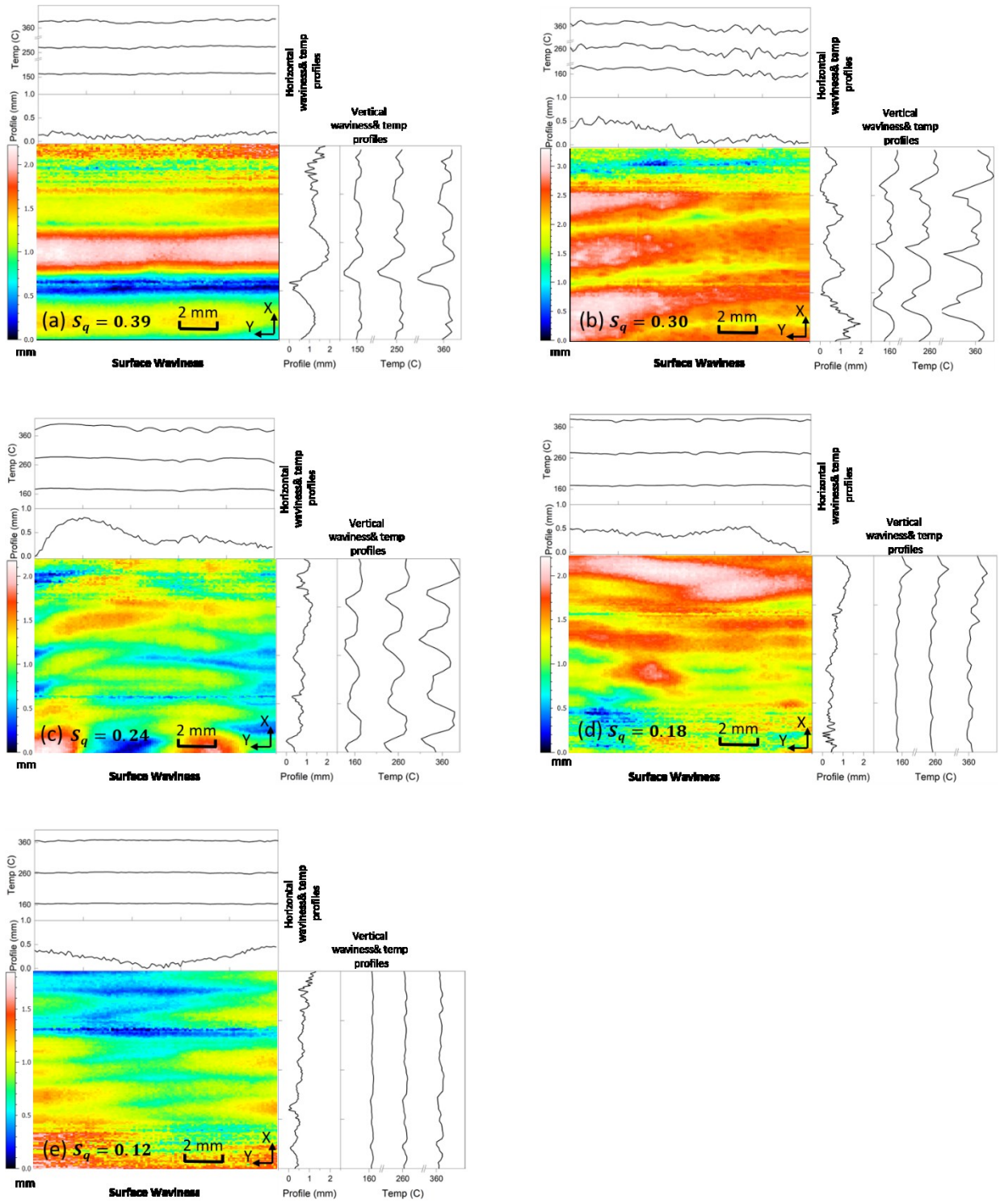

Figure 17. Surface mean profiles and temperature mean profiles along the horizontal and vertical direction at the surface texture of (a) $S_q = 0.39$, (b) $S_q = 0.30$, (c) $S_q = 0.24$, (d) $S_q = 0.18$, and (e) $S_q = 0.12$.

Three characteristics can be found in the profiles in Figure 17. First, the fluctuation of the surface profiles, especially for the vertical surface profile, decreases with the decrease of the surface texture S_q. Second, for surface texture, the fluctuation in the vertical surface profile is more pronounced than the horizontal surface profile. Third, the shape of the temperature profile at the different cooling temperature levels has approximately the same morphology as the surface profile.

The trends of the surface and temperature profiles are numerically quantified in Figure 18. Figure 18 (a) shows the standard deviation of the vertical and horizontal surface profiles at the different surface texture levels. It can be easily observed that the standard deviation of the vertical surface profile is always higher than the horizontal surface profile, which indicates that the surface waviness along the vertical direction (building direction) of the wall is greater than the horizontal direction (printing direction). Moreover, with the decrease in the surface texture, the standard deviation of the vertical surface profile decreases as well. These two observations indicate the surface deviation of the vertical waviness has a more significant effect on the surface texture than the horizontal deviation. Figure 18 (b) shows the standard deviation of the captured temperature profiles at the different surface textures and temperature levels. Similar to the result in Figure 18 (a), the vertical deviation of the temperature profile is always higher than the deviation in the horizontal temperature profile, irrespective of the cooling temperature, which means the overall surface temperature deviation is significantly influenced by the temperature distribution along the vertical direction of the wall. Besides that, the deviation of the vertical temperature profiles decreases with the surface texture significantly.

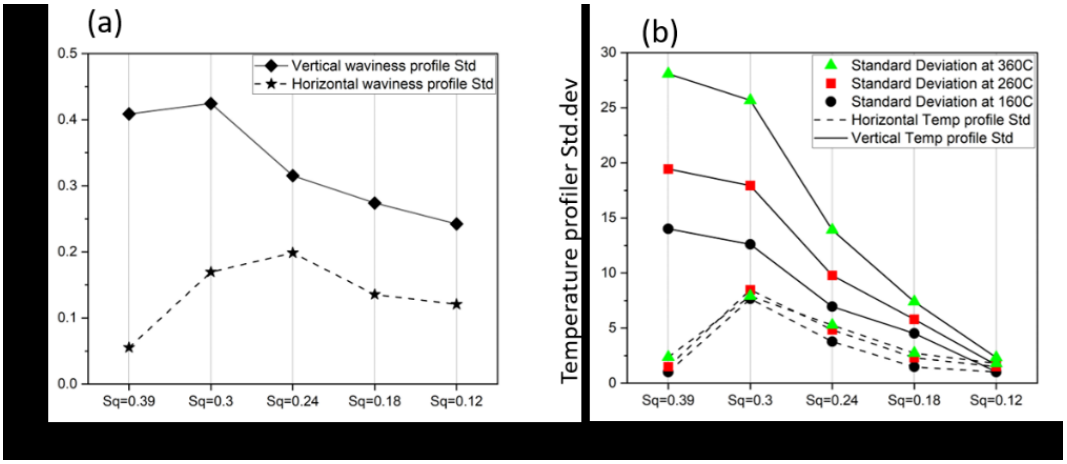

Figure 18. The standard deviation of (a) waviness profiles and (b) temperature profiles at different surface texture levels.

Figure 19 organizes the four factors into two categories and shows the influence pathway between them. In these four factors, the factor "deviation along the building direction" significantly affects the factor "IR camera captured temperature (T_{IR})", which finally affects the calculation for emissivity. The factor "deviation along printing direction" basically has no significant influence on the emissivity. The factor "Thermocouple captured temperature (T_{true})" is an individual factor that does not relate to the WAAM process but is based upon the cooling process during the examination. Therefore, the hypothesis can be proved correct and it can be concluded that the vertical deviation along the building direction predominantly affects the surface texture and the temperature (T_{IR}) the IR camera records. The true temperature (T_{true}) is not affected by the surface texture. So, the examined emissivity via Eq (1) is fundamentally affected by T_{IR} which is influenced by the deviation of the vertical waviness on the surface texture of the WAAM part.

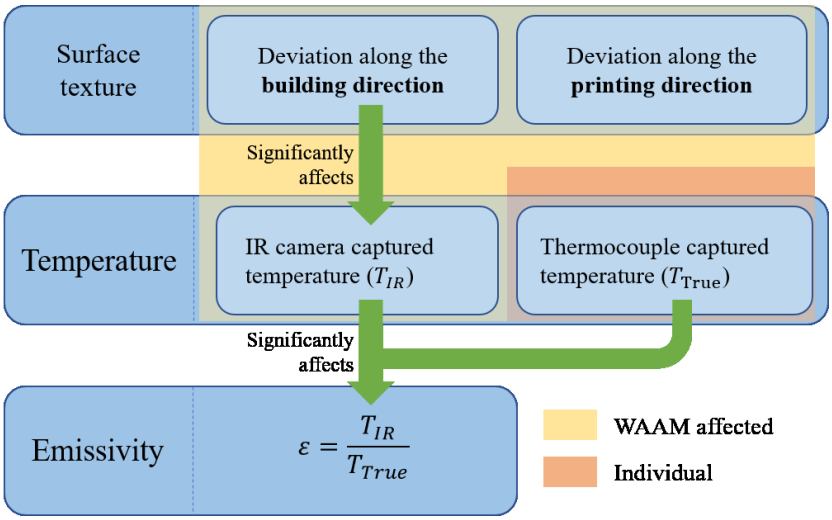

Figure 19. The effect pathway of the factors.

3.3.2 Effect of Viewing Angle and Temperature on Emissivity

The viewing angle, defined as the angle between the facing angle of the IR camera and the normal of the wall surface, is also a factor that affects the emissivity. Figure 20 shows emissivity variation at the different viewing angles and cooling temperature levels. The middle value $S_q = 0.24$ of the five surface textures of the WAAM-made walls used in Chapter 3 was chosen for this viewing angle test. The emissivity was examined at 0° (normal), 30°, 45°, 60°, and 75° respectively. There was a significant decrease in emissivity at an observation angle equal to 30°. This phenomenon

occurs at every cooling temperature level. From 30° to 75°, although the emissivity fluctuates, it does not show the conspicuous susceptibility to the viewing angle. When the viewing angle shifted from 0° to 30°, the emissivity decreased by about 0.05. Between 30° to 75°, the emissivity fluctuated only in the range of 0.03. This emissivity trend is not like other studies. Previous works show the emissivity unchanged as the viewing angle increases with respect to the normal of the rough surface (0°) until 45°, then emissivity starts decreasing drastically and eventually reaches near-zero at 90°, exhibiting a strong angular dependence [69,83].

From the perspective of the continuous cooling temperature, the emissivity usually drops with the decrease of the cooling temperature at each different viewing angle. One noteworthy point is that the rate of decrease in emissivity is not constant but accelerates as the cooling process proceeds.

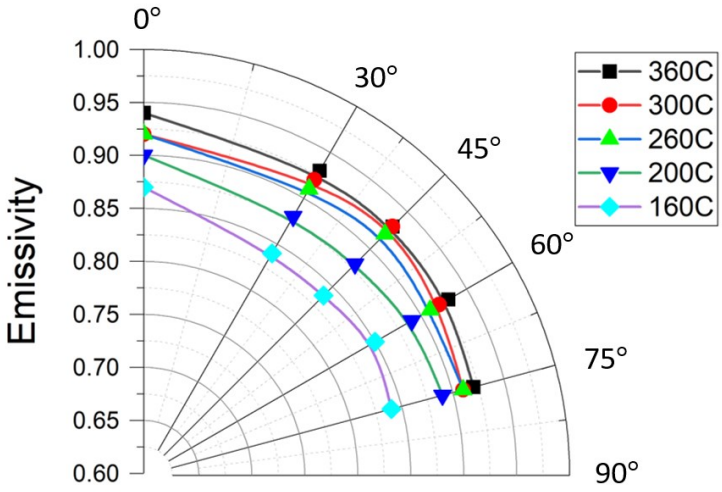

Figure 20. Effect of viewing Angle on the emissivity.

Figure 21 shows the effect of IR camera temperature (T_{IR}) on emissivity. Figure 21 (a) depicts the change of the emissivity with the T_{IR} in different surface texture levels. It's not difficult to observe that the surface texture has a strong relationship with the emissivity, and the rate of decline of each emissivity-temperature curve keeps increasing during the continuous cooling process from 350℃ to 150℃. The higher the surface texture, the more extensive the range of the emissivity during the cooling process. These observations match the results in Figure 15. Figure 21 (b) shows the change of the emissivity with the T_{IR} taken at different viewing angles. The curves appear to be bundled together, implying that the relationship between emissivity and viewing angle is not as strong as it appears to be between emissivity and surface texture. Besides that, the bundled curves present a

clear accelerated descending tendency during the cooling process same as those in Figure 21 (a), which is also consistent with the information in Figure 20.

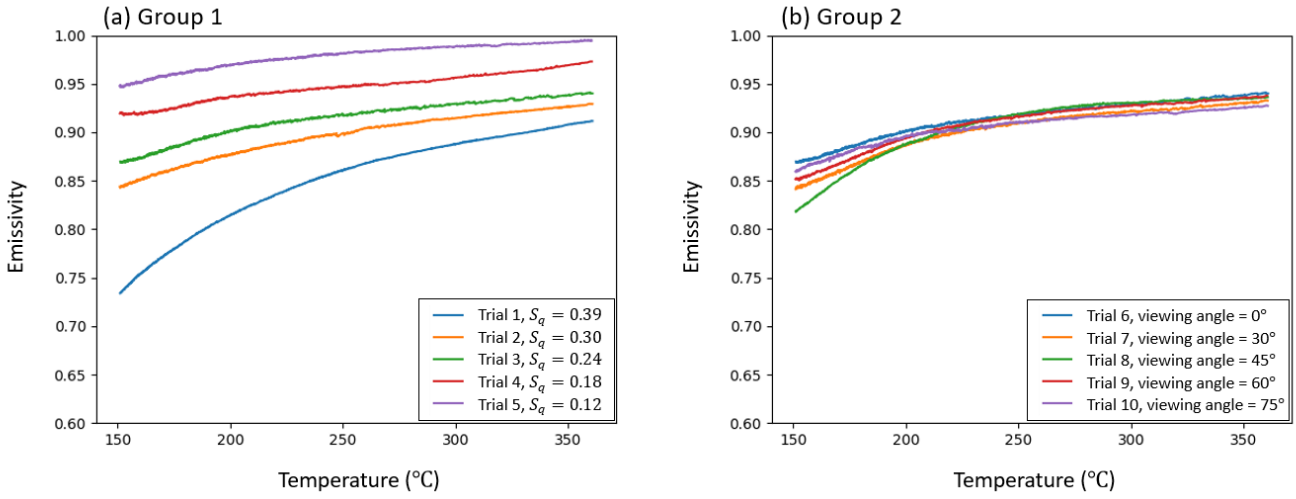

Figure 21. The change of the emissivity with the T_{IR} in (a) different surface textures and (b) viewing angles.

One of the objectives of this study is to model the emissivity so that once the temperature, surface texture, and viewing angle are known, the emissivity of the parts fabricated by WAAM can be predicted. It has been shown the viewing angle has a small effect on the emissivity therefore the viewing angle is not considered in the later regression model. To achieve this, a second-degree nonlinear regression model was built using Minitab 19 (Minitab LLC, USA). The emissivity examined from a total of 10 trials were the responses, and the temperature and surface texture (S_q) were the factors. The second-degree interaction of predictors is also considered in the regression.

$$\varepsilon = 9488e^{-4} - 9492e^{-4} * S_q + 8e^{-4} * T_{IR} - 1111e^{-4} * S_q^2 + 21e^{-4} * S_q * T_{IR} \qquad (2)$$

Eq (2) above is the fitting regression model for predicting the emissivity of the given surface texture (S_q) and temperature (T_{IR}). The model has an R-sq value of 98.06%, indicating the high accuracy of the fit. Some clues about the influence of surface texture and temperature on the emissivity can be traced from the model. For first-degree terms in Eq (2), the coefficient of the surface texture is significantly greater than the coefficient of temperature, meaning the surface texture dominates the emissivity change. It is also notable that the second-degree term of the

temperature (T_{IR}^2) is missing. That is due to the coefficient approaching an infinitely small value, which can be ignored in the model.

Based on the analysis, it can be concluded that the factors such as surface texture, temperature, and viewing angle affect the emissivity. The order of their impact from high to low is surface texture, temperature, and viewing angle.

3.3.4 Effect of the Surface Condition and Coating on Emissivity

As mentioned in Section 2.2, Group 3 is designed to investigate the relationship between emissivity and different surface conditions, including the raw surface, finished surface, oxidized surface, and carbonized surface. WAAM Additively manufactured aluminum alloys usually present themselves with a thick white oxidizing coating, as shown in Figure 22 (a). However, it was noticed that at some locations on the 7075NT additively manufactured part's surface, when this coating comes off, a dark carbonized surface with small adhesive particles reveals itself, as shown in Figure 22 (b). Figure 22 (c) is the sketch of the overlay sequence of two coatings.

The carbonized coating may come from the niobium carbide (NbC) nano-ceramic particle in the treated 7075 aluminum alloy. This involved particle is usually used for preventing excessive grain growth in steel grain boundaries, increasing the toughness and strength of the product pronouncedly [30,76]. During the material deposition process of WAAM, the NbC nano-ceramic particle is not melted but flows with the liquid aluminum in the molten welding pool and is evenly distributed inside the printed layer. The nano-ceramic particles that flow to the edge of the molten pool form the black particle cluster when the molten pool solidifies, attached to the part's surface. Obviously, the NbC nano-ceramic particle, as the most critical component in this novel material, could also affect the emissivity. Considering there is no research on the emissivity of this material so far, further investigation is needed.

Figure 23 shows the four surface areas corresponding to four trials. These four surface conditions were processed on the same part's surface to ensure the consistency of the surface texture. The emissivity examination process in Group 3 is the same process used in Group 1 and Group 2.

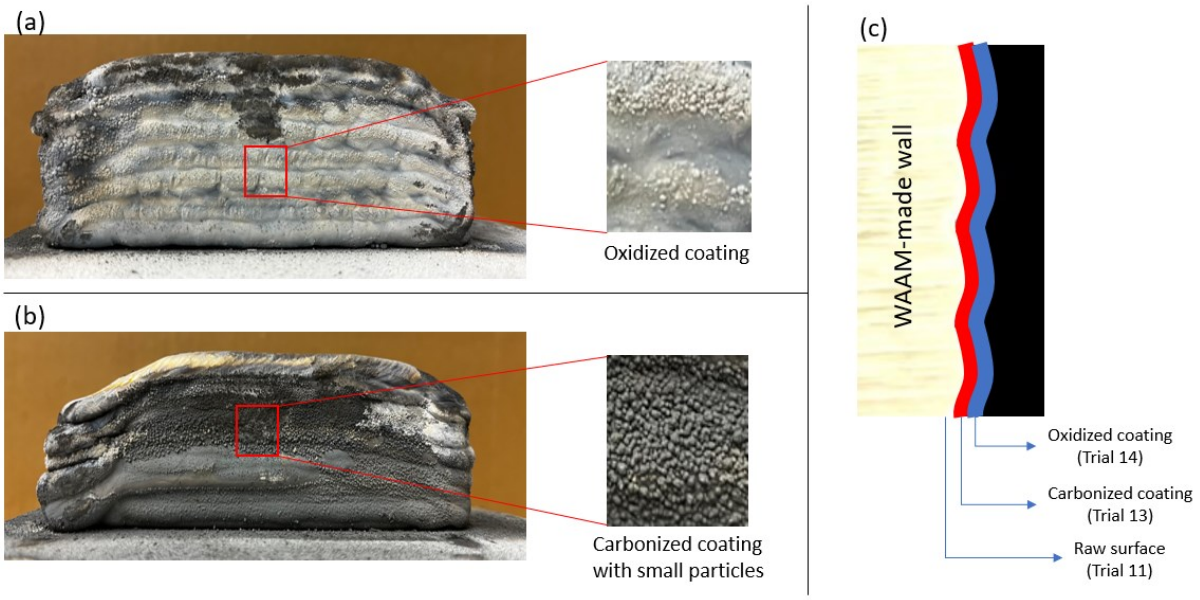

Figure 22. (a) The white oxidized coating attached on the surface. (b) The dark carbonized coating after removing the oxidized coating. (c) The schematic of the layout of the oxidized and carbonized coatings.

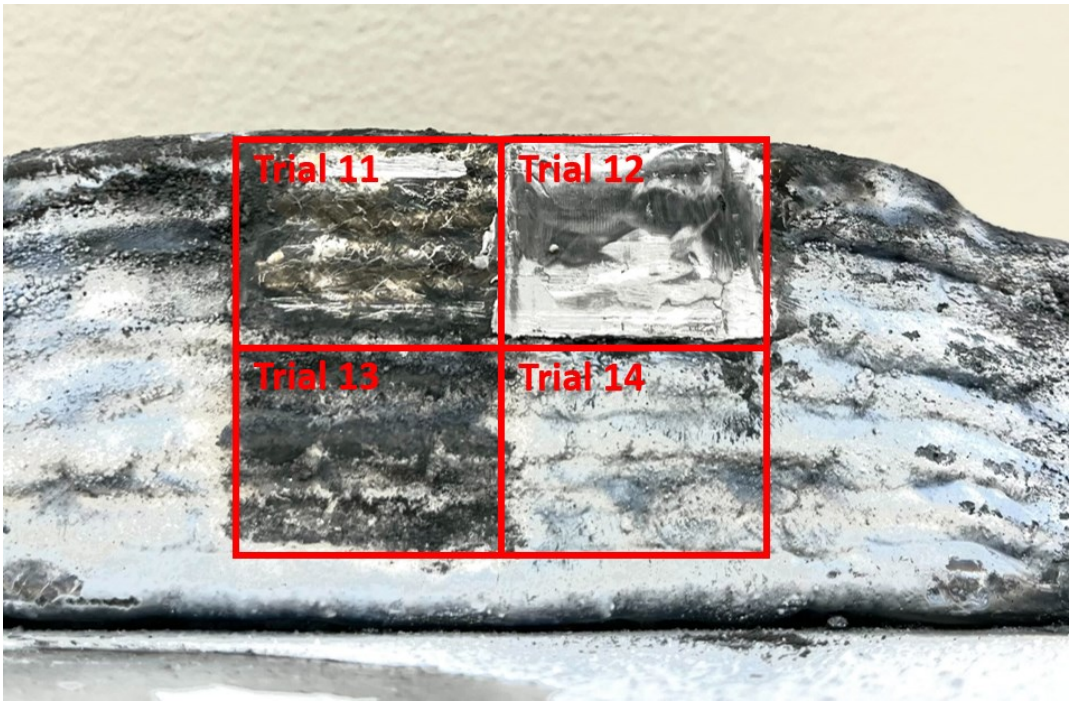

Figure 23. Four post-processed surface areas on one WAAM-made part by 7075NT aluminum alloy.

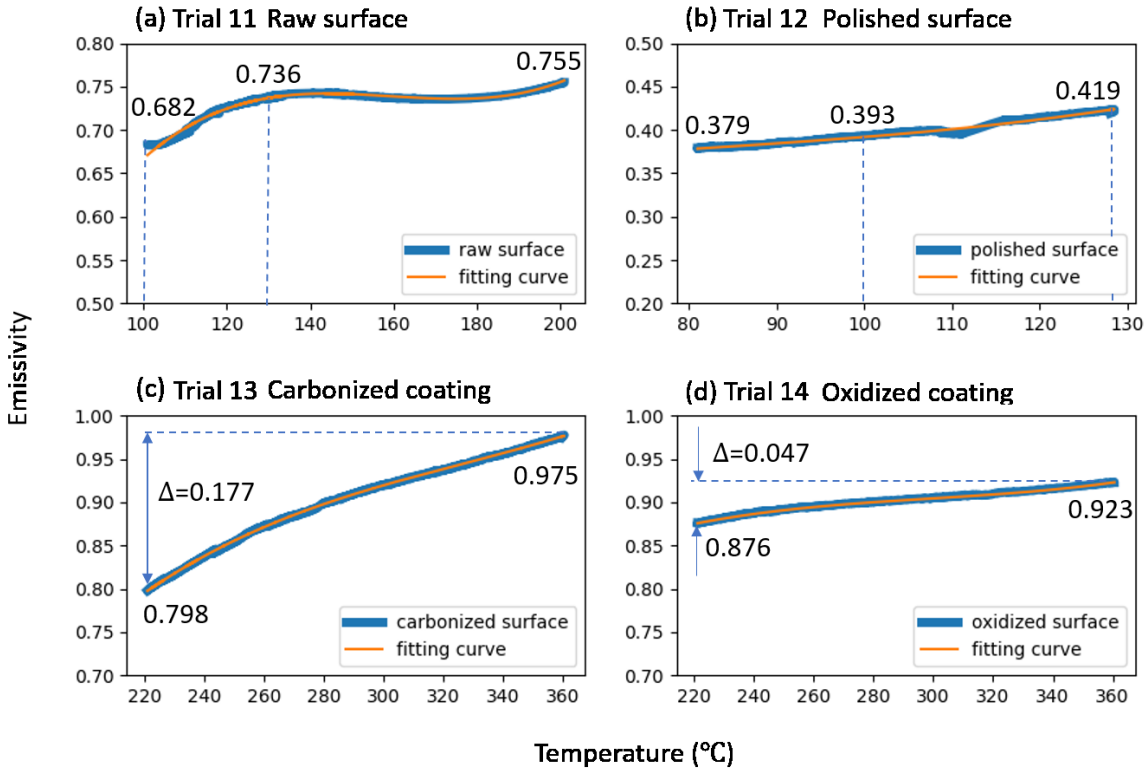

Figure 24. The emissivity gradient of (a) raw surface, (b) polished surface, (c) carbonized coating, and (d) oxidized coating.

The blue curves plotted in Figure 24 are the results of emissivity versus IR camera recorded temperature, where the emissivity for different surface conditions (raw, polished, carbonized coating, and oxidized coating) are shown. Figure 24 (a) and (b) are the results for raw and polished treated surfaces. One of the most significant discrepancies between the results in the Group 1 and Group 2 experiments discussed earlier is the comparatively low emissivity. For the raw surface, the emissivity gradient ranged from 0.755 to 0.682 in the temperature interval between 200℃ and 100℃. However, for the polished surface, the emissivity gradient starts from 0.419 at 130℃ and drops to 0.379 at 80℃. Because Trial 11 and Trial 12 have the same experiment setup except for the surface condition. Therefore, it can be concluded that the 7075NT aluminum alloy part's polished surface has a lower emissivity than the raw surface part. One concern for this conclusion may be the different X-axis range (the IR camera temperature range) in Trial 11 and Trial 12. This difference is because of the limit of the calibration range of the IR camera. However, when analyzing the overlapped range, which is from 128℃ to 100℃ in Figure 24 (a) and (b), the emissivity of the polished surface is also smaller than the emissivity of the raw surface. The

conclusion “polished surface has a lower emissivity than the raw surface part” can be therefore confirmed.

Figure 24 (c) and (d) shows the emissivity gradient of the carbonized and oxidized coating corresponding to the results from Trial 13 and Trial 14 between the temperature range from 360℃ to 220℃. The emissivity gradient of the carbonized coated surface ranges from 0.975 to 0.798, and the oxidized coated surface ranges from 0.923 to 0.876. These results are close to the emissivity gradient examined in Group 1 and Group 2. It is also obvious in Figure 24(c) and (d) that the range of the emissivity of the carbonized coating surface ($\Delta = 0.177$) is wider than the range of emissivity of the oxidized surface ($\Delta = 0.047$). Finally, a general pattern that can be observed in all four subplots is that the emissivity usually decreases when the temperature decreases. This pattern is consistent with the summary from Group 1 and Group 2.

Table 8. The third-degree fitting results for different surface conditions.

Trial	11	12	13	14
Equation	$\varepsilon = B1 * T_{IR} + B2 * T_{IR}^2 + B3 * T_{IR}^3 + b$			
B1	0.0324	0.0029	0.0147	0.0069
B2	-2.05E-4	-2.84E-5	-4.21E-5	-2.23E-5
B3	4.29E-7	1.20E-7	4.28E-8	2.48E-8
Intercept (b)	-0.951	0.267	-0.852	0.174
Residual Sum of Square	0.0103	0.0025	0.0013	1.3659E-4
R-Square	0.9864	0.9839	0.99	0.99

In each subplot in Figure 24, the thin orange line represents the third-degree fitting curve of emissivity. Table 8 lists the fitting model and corresponding coefficients for each term for the trials in Group 3 according to their specific surface conditions. The small regression validation values of the “Residual Sum of Square” and “R-Square” in the last two rows also indicate that the fitting result is highly accurate. This fitting model can be used for predicting the emissivity for different WAAM-made parts’ surface condition in the future.

3.4 Chapter Conclusion

By performing four experimental groups, this study examined the emissivity and its gradient in terms of continuous air-cooling temperature, and explored the influence of the surface texture, viewing angle, temperature, and polished and coated surfaces on the emissivity. Based on the analyzed results, key findings are summarized and listed below:

1) The emissivity of the WAAM-made 7075NT aluminum alloy samples during the continuous air-cooling process between 360℃ to 150℃ has a minimum value of 0.733 at the most significant surface texture $S_q = 0.39$, and the maximum value of 0.995 at the smallest surface texture $S_q = 0.39$.
2) The results of the emissivity gradient exhibit a strong inverse proportionality between surface texture and emissivity. The vertical deviations derived from the vertical waviness have the most considerable influence on the surface texture, which further affects the IR camera temperature (T_{IR}). The emissivity is therefore affected since the temperature the IR camera captures is influenced by the surface texture.
3) In contrast to the trend between surface texture and emissivity, the emissivity gradient does not present a significant correlation with the change of the viewing angle between 0° and 75°.
4) Unlike other additively manufactured aluminum alloy parts, which have only an oxidized coating on the surface, the WAAM-made 7075NT aluminum alloy part has two coatings: oxidized coating outside and carbonized coating underneath.
5) Surface coatings also affect the emissivity gradient significantly. The polished surface shows less emissivity than the raw and other coated surfaces and the carbonized coated surface has a larger range of emissivity gradient than the oxidized coated surface.

4. WAAM Parameter Screening Experiment

4.1 Introduction

WAAM is an interdisciplinary manufacturing process that involves mechanical, electric, and material knowledge. This inherent feature causes that many processing parameters exist in the WAAM process. More importantly, these processing parameters interplay to affect the parts' qualities and bring tremendous difficulty in quantifying the influence of these parameters on the part's quality. Therefore, a screening experiment is necessary to find the parameters which most affect the quality. In this chapter, a screening experiment was designed and conducted to screen out the parameters which affect the printing process significantly. The geometrical properties, including wall height and width, wall projected width, wall's 1st layer height and width, wall's 1st layer height difference, and wall's 1st layer width difference of the WAAM-made wall, were quantified. These parameters were characterized and screened based on the standard effect factor via ANOVA analysis.

4.2 Experimental Design

By reviewing other researchers' contributions in Section 1.7, the Arc Correction, Gas Flow Rate, Torch Travel Speed (TTS), Wire Feed Speed (WFS), Interpass Temperature, and Pre-heat Temperature are known to have a profound influence on part geometrical qualities. A full-factorial screening experiment with three levels and six factors was designed to investigate the influence of these six process parameters on the WAAM-made part's quality. The definitions, unit, and levels of the considered factors in the screening experiment are listed in Table 9. The full-screening experiment table and corresponding results are shown in Table 10. For each trial, a 16-layer and 100 mm length single-track multi-layer wall was printed on a three by six-inch substrate. The fabricating path is illustrated in Figure 25.

Geometrical property is one of the essential properties of the additively manufactured part. As the part will be used in industry, there is no meaning in analyzing the mechanical property and microstructure if the geometrical property is not satisfied. To assess the influence of factors on the geometrical property, the standard effect of the wall height, wall width, wall projected width, 1st layer width, 1st layer height, 1st layer width difference, and the 1st layer height difference are

defined as the responses to quantify the geometrical quality. The detail results of these responses are listed in Table 11. The geometry of the 1st layer is considered as a response in this screening experiment because when fabricating a wall, the connection between the 1st layer and the substrate may affect the thermal condition of the part during the process [52][55], causing undesired geometrical properties on following layers. The wire used in this screening experiment is 7075NT aluminum alloy wire with a 1.2mm diameters made from MetaLi LLC (USA). The chemical compound of this alloy is listed in Table 3. The protecting gas used in this study is pure (100%) argon.

Table 9. The definition of factors for WAAM.

factors	Unit	Levels	Definition / Description
Arc Correction	%	-10, 0, 10	The setting for correcting the arc length.
Gas Flow Rate	CFH	20, 35, 50	The rate of welding protection gas flow from the torch.
Pre-heat Temperature	℃	20, 70, 120	The temperature of the aluminum substrate before the printing.
Interpass Temperature	℃	200, 350, 500	The temperature at the time when start printing the next layer.
Wire Feed Speed (WFS)	in/min	120, 160, 200	The rate at the wire feeder feeds the wire.
Torch Travel Speed (TTS)	in/min	8, 14, 20	The rate of the movement of the torch.

Table 10. The parameter set of screening experiment and responses.

Trial	Arc Correction	Gas Flow Rate	Pre-heat temperature	Inter-pass Temperature	WFS	TTS	Wall height	Wall width	Wall projected width	1st layer height	1st layer width	1st layer height diff	1st layer width diff
1	10	20	120	350	200 (87.65, 12.75V)	8	38.19	9.49	11.37	4.79	4.92	0.70	1.04
2	0	50	120	500	200 (87.65, 12.75V)	20	23.20	5.98	7.24	2.72	3.34	0.40	0.15
3	10	20	20	500	160 (72.24A, 11.8V)	20	23.62	5.01	6.90	2.39	3.26	0.26	0.21
4	10	50	70	500	120 (51.32A, 10.33V)	8	30.92	6.52	9.45	2.88	4.71	0.86	0.37
5	0	35	70	350	160 (72.24A, 11.8V)	14	30.47	5.55	6.59	3.36	4.04	0.25	0.27
6	-10	20	120	500	120 (51.32A, 10.33V)	14	22.99	4.62	6.39	2.45	3.58	2.99	1.78
7	-10	20	70	200	200 (87.65A, 12.75V)	20	25.90	5.53	6.95	2.78	3.26	0.60	0.23
8	-10	50	120	200	160 (72.24A, 11.8V)	8	43.59	7.19	8.73	3.96	4.82	0.11	0.07
9	-10	50	20	350	120 (51.32A, 10.33V)	20	20.47	3.79	6.04	2.12	3.17	1.57	1.01
10	10	50	20	200	200 (87.65A, 12.75V)	24	29.29	7.02	8.60	3.63	3.89	0.26	0.99
11	10	35	120	200	120 (51.32A, 10.33V)	20	23.11	3.31	4.58	2.06	3.01	2.33	0.92
12	0	20	20	200	120 (51.32A, 10.33V)	8	37.23	5.60	6.56	4.11	3.93	0.36	0.42
13	-10	35	20	350	200 (87.65A, 12.75V)	8	36.42	10.09	11.42	4.88	4.80	0.32	0.18

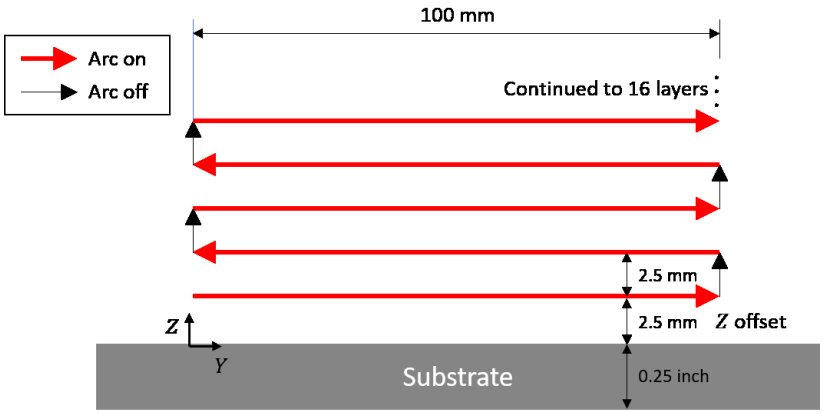

Figure 25. Printing path of each part used in the screening experiment.

Table 11. The definition and unit of responses

Responses	Unit	Definition
Wall height	mm	The mean height of the wall
Wall width	mm	The mean width of the wall
Wall projected width	mm	The top view projected width of the wall.
1st layer height	mm	The mean height of the 1st layer
1st layer width	mm	The mean height of the 1st layer
1st layer height difference	mm	The difference between the maximum height and minimum height
1st layer width difference	mm	The difference between the maximum height and minimum width

4.3 Result and Discussion

The result of the responses is listed in the last seven columns in Table 10. Due to the acceleration and deceleration of the gantry system and the unstable arc ignition at the start of the deposition and extinguishing stages at the end of the deposition process, as shown in Figure 26 (a) and Figure 26 (b), the start and end of the wall are slumping which cannot truly represent the influences of factors to the geometrical property as shown in Figure 26 (c). Herein, only the data from the middle part of the wall, where the TTS is constant and the arc is stable, was used for analysis.

A standardized effect is a dimensionless statistical terminology usually used to quantify how much the factor affects the responses by the experiments. A greater standardized effect value means this

factor has more influence on the corresponding response. The standard effect for each factor in terms of different responses at the 0.05 level was calculated via Minitab (USA) and is shown in Figure 27.

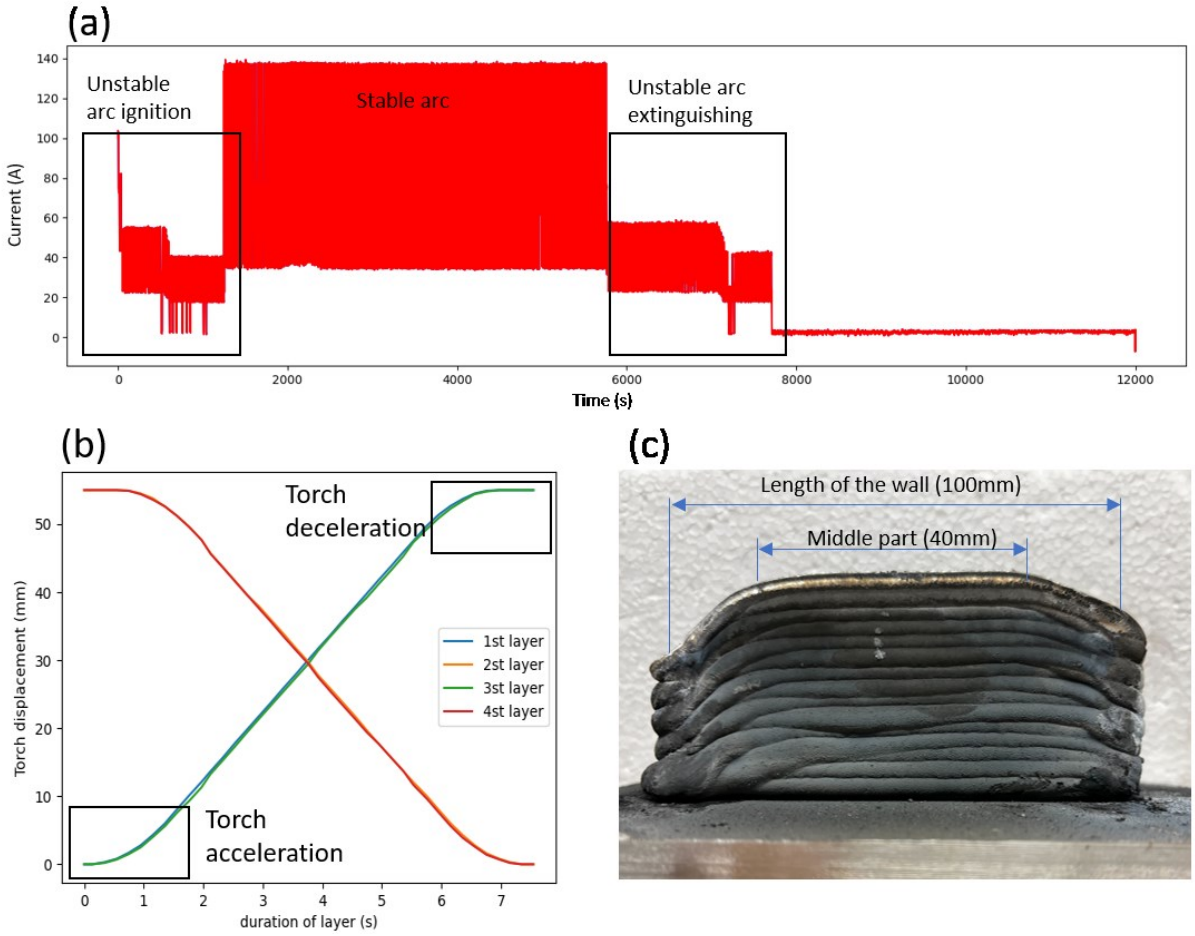

Figure 26. (a) An unstable current at the starting and ending of a layer indicates the arc is unstable when igniting and extinguishing. (b) The torch displacement versus time plot shows there is significant acceleration and deceleration of the torch. (c) Significant slumping happens at the two ends of the wall.

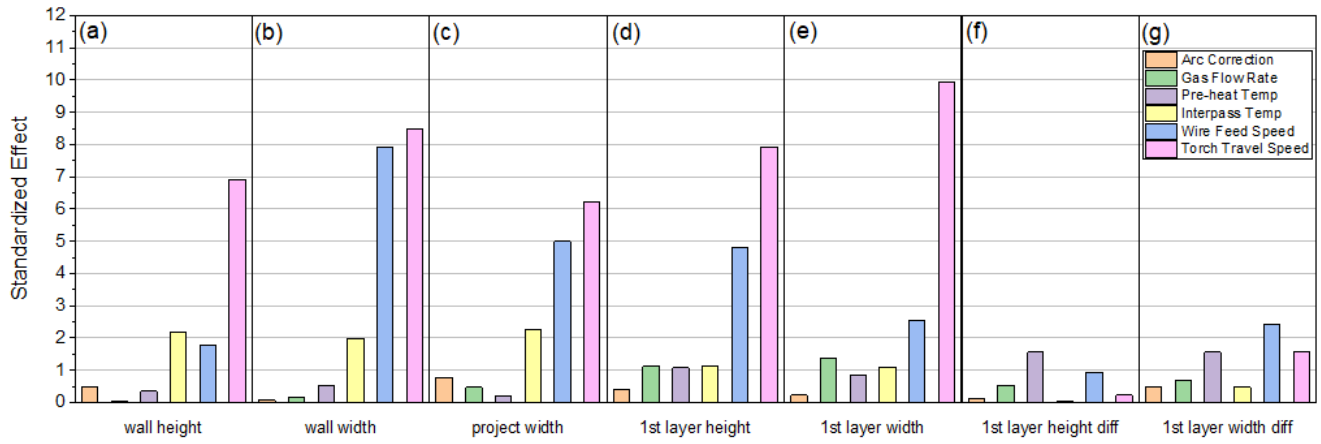

Figure 27. The chart of the Standardized Effect (a = 0.05) for each response.

The sub-chart (a) and (b) in Figure 27 show the standard effect value of the different responses for the wall mean height and width. It can be observed that the TTS, WFS, and interpass temperature have a greater standardized effect than the other three factors. TTS has the most significant influence on height and width at a standardized effect of around 7.5. WFS has a greater effect on the wall width but less on the wall height. The interpass temperature also impacts the wall width but less than TTS and WFS. In sub-chart (a), the interpass temperature and WFS are almost the same with a standardized effect value of about 2, which means WFS loses most of its effect on wall height, and TTS dominates the effect on wall height. The wall projected width is considered a response representing the wall's width distortion. The bigger the factor's standardized effect value to this response, the more likely this factor is to cause wall distortion. In sub-chart (c), the top three factors to which the wall width distortion is susceptible to are TTS, WFS, and interpass temperature. This result is consistent with the top three factors for the wall width in the sub-chart(b).

The sub-chart (d) and (e) in Figure 27 show the influence of factors on the 1st layer width and height. It can be observed that the TTS and WFS have a distinct effect from the rest factors. It is worth noting that in the sub-chart (e), the standardized effect of TTS reaches 10 while the standardized effect is less than 3 for the second most influential factor - WFS, meaning TTS can even be seen as an independent factor that controls the 1st layer width. The 1st layer height difference and the 1st layer width difference are the responses for enabling quantifying the geometrical continuity of the 1st layer. The definitions of these two factors are listed in Table 3. The bigger these two responses, the lower geometrical continuity is for the 1st layer. It can be

concluded from sub-charts (f) and (g) that pre-heat temperature and WFS, instead of TTS, strongly influence the 1st layer continuity. However, except for pre-heat temperature and WFS, TTS still has a more significant impact than Arc correction, Gas flow rate, and interpass temperature. Technically, because the 1st layer is printed directly on the substrate, the Pre-heat temperature can be seen as the "interpass temperature" of the 1st layer. So, although Interpass temperature does not show its influence on the 1st layer explicitly, its effect has been presented by the factor pre-heat temperature.

4.4 Chapter Conclusion

By passing through all sub-charts in Figure 27, a short conclusion can be made that three parameters: TTS, WFS, and interpass temperature have a significant influence on the wall geometrical property and are screened out as the critical factors that will be considered in the later experiment. Due to the statistical limitation of the screening experiment, the analysis results can only determine which parameter affects the part's mechanical quality pronouncedly. However, the analysis cannot determine how the increase or decrease of the parameter influences the quality. The internal relationship still cannot be found. Thus, further experiments need to be done focusing on two aspects: 1) The relationship of the effect of the TTS, WFS, and interpass temperature on the part's geometry quality; 2) Finding the proper TTS, WFS, and interpass temperature values as a parameter set that can bring the best part's geometry property.

5. WAAM Process Parameter Exploration

5.1 Introduction

In the last chapter, the parameters TTS and WFS were proven to have a substantial effect on the geometrical properties of the WAAM-made part. Thus, in this chapter, the main goal is to explore the best combination of TTS and WFS to create sound geometrical properties in a layer. A visual assessment is applied, and the energy consumption is calculated to judge the consequence of using different TTS and WFS sets on the layer's geometrical property. The TTS and WFS that could lead to a sound layer geometry with less energy consumption at the same time will be chosen as the best parameters set for processing the 7075NT aluminum part in WAAM. In addition, the relationship between WFS and contact point to workpiece distance (CTWD) and CMT process current and voltage was explored to meet the main objectives.

As a criterion to judge the suitability of the combination of WFS and TTS, the term energy consumption is used to describe the consumption of the heat input for depositing 1 gram 7075NT aluminum alloy, which is defined as the ratio of the heat input (HI) of one layer to the weight of the layer (W_{layer}), as expressed in Eq (3). t_{layer} is the duration of depositing a L_{layer} length layer, which is expressed in Eq (4). W_{layer} can be calculated via Eq (5), where ρ is the density of the 7075NT aluminum alloy, d is the diameter of the 7075NT aluminum alloy wire used in this study.

$$\text{Energy consumption} = \frac{HI * t_{layer}}{W_{layer}} \tag{3}$$

$$t_{layer} = \frac{L_{layer}}{TTS} \tag{4}$$

$$W_{layer} = \rho * (0.25 * \pi d^2) * (WFS * t_{layer}) \tag{5}$$

In welding, the term “heat input (HI)” is usually used to quantify the behavior of WFS and TTS. Heat input describes the amount of electrical energy that is supplied to the workpiece during the welding process. The mathematical expression of the heat is shown in Eq (6), where I_a and U_a are the average current and voltage, η is the arc efficiency (in CMT arc efficiency is 0.8 [21]), and TTS is the torch travel speed. The unit of heat input is J/mm.

$$HI = \eta \times \frac{I_a \times U_a}{TTS} \tag{6}$$

In the CMT process, I_a and U_a are coupled with WFS and Contact Tip to Workpiece Distance (CTWD), which is also referred to as "wire stick-out distance" in some studies. So, Eq (6) can be reformatted into Eq (7). The I_a and U_a can be confirmed once WFS and TTS are decided. However, there is no lookup table or research that reveals the relationship between I_a and U_a, and WFS and CTWD in 7075 aluminum alloy CMT process. So, to find energy consumption, the relationship between average current (I_a) and voltage (U_a), and WFS and CTWD must be characterized.

$$HI = \eta \times \frac{f(WFS, CTWD)}{TTS} \tag{7}$$

5.2 The Influence of WFS and CTWD on Process Current and Voltage

5.2.1 Introduction of Synergic Line and CTWD

Unlike conventional welding technology, the current and voltage in the CMT process cannot be tuned separately. Instead, they can be changed only by adjusting WFS and CTWD. Every combination of WFS and CTWD corresponds to a current and voltage parameter set called Synergic Line, as illustrated in Figure 28.

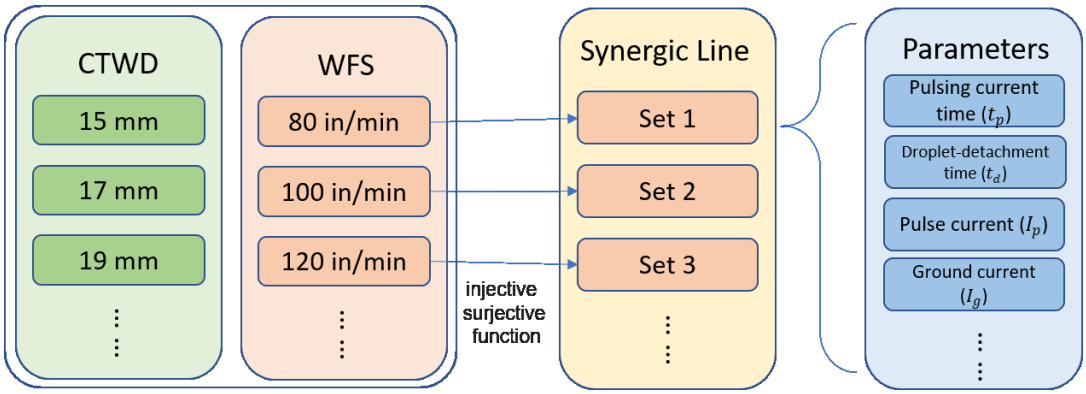

Figure 28. The bijection relationship between WFS and Synergic Line.

A total of the five parameters are the most critical parameters in a Synergic Line [17,84–86]. They are Pulsing current time (t_p), Droplet-detachment time (t_d), Droplet detachment current (I_d), Ground current (I_g), and Pulse current (I_p). These parameters are annotated as (1), (2), (6), (8), and (9), respectively, in Figure 29.

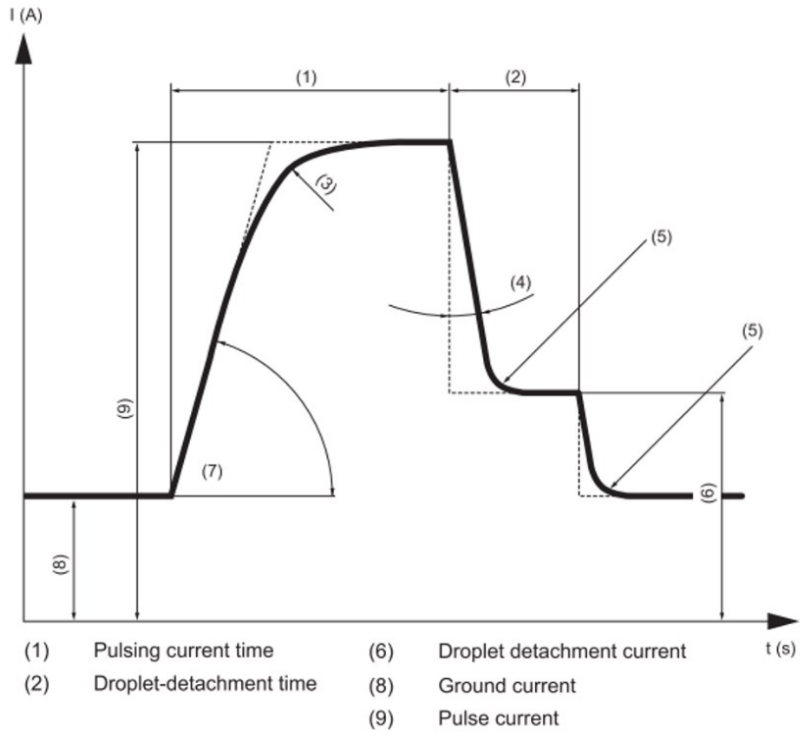

Figure 29. The schematic current waveform in one cycle of CMT [87].

Figure 30 shows one period of CMT current waveform of welding Q235 mild steel. The WFS, current, and voltage of one period are recorded. It can be seen that the pattern of each of these three waveforms consists of four stages: Boost stage, Wait stage, Necking stage, and Detachment stage.

- Boost stage: At the beginning of this stage, the arc reignites with the current rising to the boost current. Since voltage is coupled with current, the voltage follows the raising of the current. When a reignited arc is sensed, the CMT welding system's digital process control unit sends a signal to the wire feeding system to feed the wire forward. The wire speed gradually increases from a negative value indicating wire retraction. Due to inertia, the wire feed speed does not reach a steady-state maximum at the end of this stage. The arc melts the workpiece and the wire and a droplet is formed at the end of the wire.
- Wait stage: During this stage, the current is significantly reduced in order for the droplets not to be separated but to remain at the end of the wire. The wire feeding speed increases to a maximum value, and this value is maintained until a short circuit occurs. The total duration of this stage is 3.92 ms. The maximum wire feed rate measured is about 40 m min−1.

- Necking stage: In this stage, the current rises to the level of droplet detachment current (I_d= 180A) to enhance the electromagnetic force, speeding up the necking of the molten metal column. The wire feed rate decreases until it becomes a negative steady-state value, indicating the retraction of the wire. The droplet spreads into the weld pool smoothly under the combined action of surface tension force and gravitation. The droplet-detachment time (t_d) is about 3.84 ms at this stage.
- Detachment stage: In this stage, the welding current decreases to the level of Ground current (I_g), which equals 60A, and the arc voltage decreases to about 3 V in 0.36 ms. The wire feed rate is kept negative, indicating that the wire is mechanically retracted. The wire retraction motion promotes the pinch-off of the molten metal column and enables spatter-free droplet detachment at both low current and voltage.

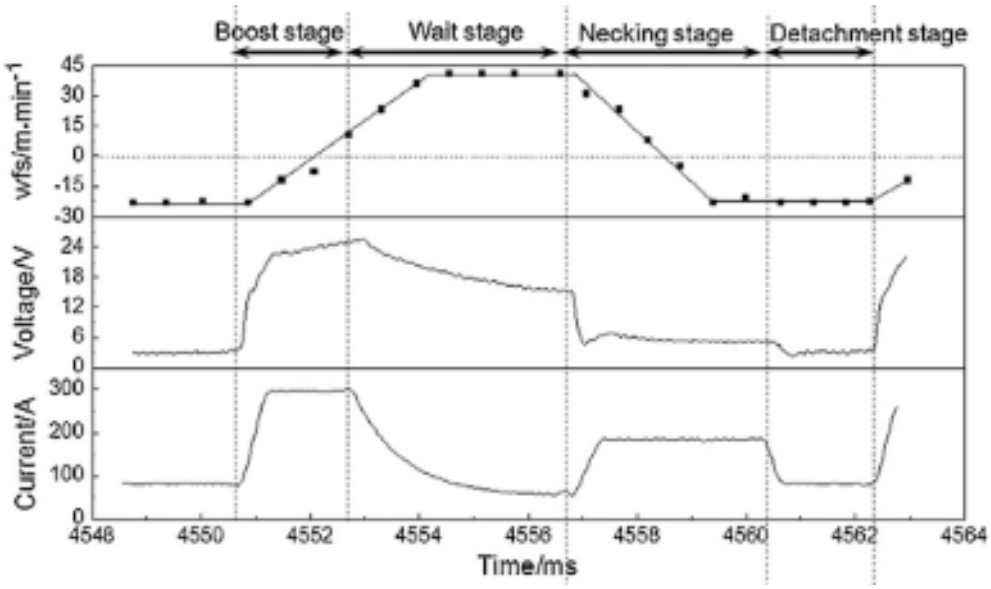

Figure 30. The typical current waveform at WFS = 200 in/min of CMT in welding Q235 mild steel [85].

The Contact Tip to Workpiece Distance (CTWD), illustrated in Figure 31, is another influential factor. Generally, the CMT machine provides more current and voltage in order to keep the arc stable when setting a large CTWD [88], which affects consistency of weld penetration. In welding industry, weld penetration is the groove of the base material to be joined is united and embedded with molten joining materials. In WAAM, weld penetration influences the joining and connection between the latest layer to the printed layer, further affecting the geometry of the layer [89]. Therefore, exploring a proper CTWD for the WAAM process is meaningful.

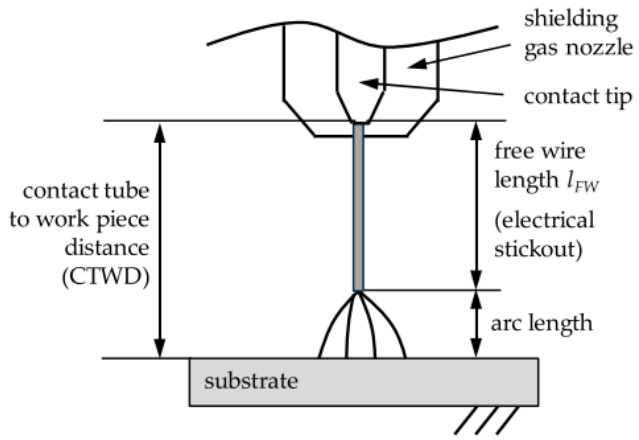

Figure 31. Definition of contact tip to workpiece distance (CTWD) [88].

5.2.2 Experimental Design

As shown in Table 11, two groups of experiment were designed and conducted to characterize the relationship of WFS and CTWD to Synergic Line (current and voltage). The level range of WFS and CTWD in this experiment design refers to the parameters set in the CMT-based WAAM-made 4043 aluminum alloy part [48]. To investigate WFS, in Group 1, the CTWD was fixed at 15 mm, but WFS as the factor was tuned with eight levels from 80 to 220 in/min with a 20 in/min interval between two levels; Similarly, to investigate CTWD, WFS was fixed to 100 in/min, but CTWD were tuned from 15 to 23 mm with a 2 mm interval between two levels. The printed layer length was set to 100 mm for each trial. The current and voltage during the printing process were recorded by the energy monitoring module mentioned in Chapter 3. The material used in this experiment design is 7075NT aluminum alloy, the same as the material used in the previous chapters.

Table 12. The detail of the parameters set in the experiment.

	WFS (in/min)	CTWD (mm)
Group 1	80	15
	100	
	120	
	140	
	160	
	180	
	200	
	220	
Group 2	100	15
		17
		19
		21
		23

5.2.3 The Effect of WFS and CTWD on Synergic Line

The complete Synergic Line (current and voltage waveforms) at the different WFS was recorded and shown in Figure 32. Figure 33 (a) presents the current waveforms. Two apparent patterns can be observed.

First, the Boost stage and Wait stage can be recognized in all eight waveforms. However, unlike the waveform in welding steel, the existence of the Necking stage or Detachment stage in the aluminum alloy welding waveform depends on the designated WFS. When WFS is lower than 120 in/min (including 120 in/min), the Necking stage presents since the low background current cannot provide enough heat to improve the viscosity and fluid ability of the undetached droplets causing discrete droplet detachment. Therefore, in the situation of low welding current, the Necking stage appears with a higher current than the background current to facilitate droplet transfer. When WFS exceeds 120 in/min, the Necking stage disappears and is replaced with the Detachment stage. This is because the spatter could happen when the droplet detaches from the tip of the wire at the time the wire is moving upward in a high welding current. A comparatively low current could avoid the generation of the spatter when the liquid bridge breaks. Regardless of either the Neck stage or the Detachment stage, the ending current converges at around 40A, which may be the most suitable value explored by the Fronius to fulfill the smooth material transfer process. The second pattern is that the Pulse current (I_p) increases with the increase of the WFS until WFS=180 in/min. After

WFS = 180 in/min, the duration of the Boost stage is significantly extended with the constant Pulse current (I_p).

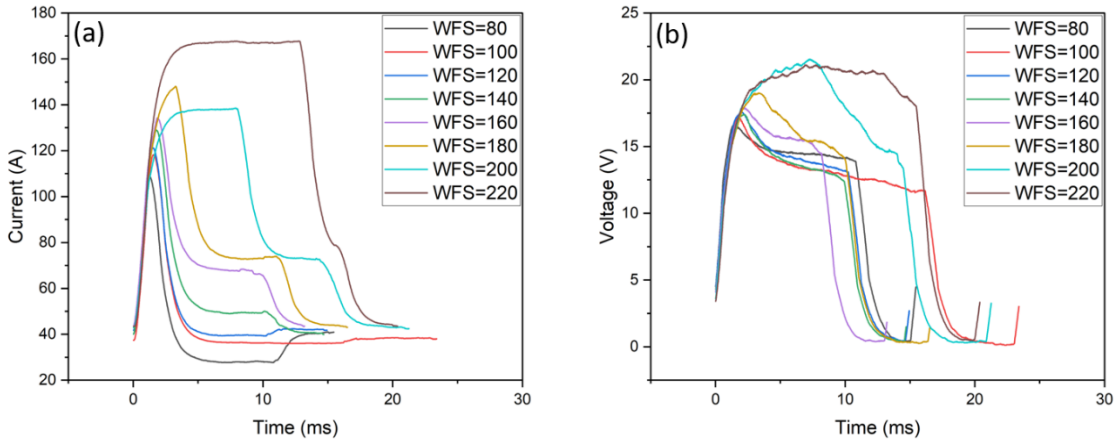

Figure 32. The current(a) and voltage(b) of the Synergic Line at different WFS.

Figure 33 shows the Synergic Line (current and voltage waveforms) at the different CTWD. In Figure 33 (a), all stages exist except for the Detachment stage. There is also an obvious pattern in current waveforms, the peak values are almost identical in one duty cycle at different CTWD, where the Pulse current (I_p) is 110 A and the Ground current (I_g) is about 30 A, the duration of the Boost and Necking stages are almost the same at the different CTWD levels. However, the Droplet-detachment time (t_d) (the duration of the Wait stage) is varied with CTWD. With the increase of the CTWD, t_d decreases from 10.3 ms to 7.0 ms, which results in a shorter duration of one duty cycle at a lower CTWD.

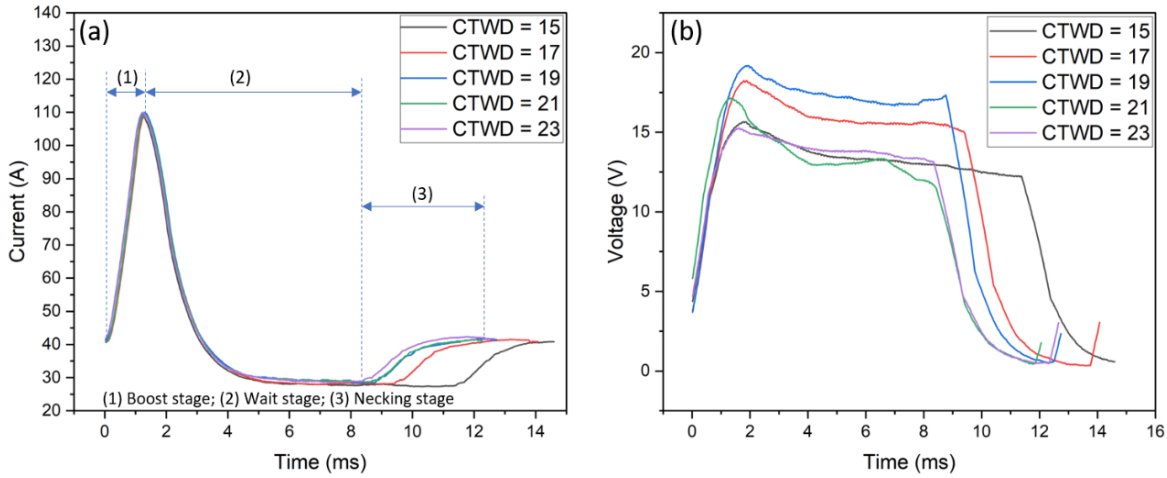

Figure 33. The current(a) and voltage(b) of the Synergic Line at different CTWD.

The average current (I_a) and the average voltage (U_a) was calculated based on Eq (8) and Eq (9), respectively, where i is the number of the sample, and i_t is the total number of samples in one duty cycle. I_a, and U_a at different CTWD are listed in Table 13. It can be seen in the table that I_a increases with increasing CTWD due to the shorter Wait stage and U_a slightly fluctuates in a small range between 9.5 V to 10.5 V, which leads to an oscillated power and further influences the heat input (HI).

$$I_A = \frac{\sum_1^i I_i}{i_t} \tag{8}$$

$$U_A = \frac{\sum_1^i U_i}{i_t} \tag{9}$$

$Power = I_A \cdot U_A$	(10)

Table 13. The average current (I_a) and the average voltage (U_a) at different CTWD

CTWD (mm)	I_a (A)	U_a (V)	Power (W)
15	41.45	9.77	404.97
17	41.76	10.47	437.23
19	42.01	10.35	434.80
21	42.16	9.82	414.01
23	42.65	10.00	426.50

5.2.4 Conclusion

In this study, five essential parameters in the aluminum alloy CMT welding Synergic Line were explored, and the effects of WFS and CTWD on them were investigated by conducting two groups of single-factor experiments.

In Group 1, eight levels of WFS were involved. From the recorded current and voltage waveforms, the following features can be found:

- Three stages appear in the Synergic Line of welding aluminum alloy. The Boost stage and Wait stage always exist. When the WFS lower than 120 in/min, the Necking stage is the

third stage in the Synergic Line. When WFS is higher than 140 in/min, the Necking stage disappears and is replaced by the Detachment stage.

- The Pulse current (I_p) increases with the increase of the WFS until WFS=180 in/min. After WFS = 180 in/min, the duration of the Boost stage is significantly extended.
- Regardless the current either enters the Neck stage or Detachment stage, the ending current lingers at around 40 A.

In Group 2, five levels of CTWD were involved. The following features can be found:

- The Boost stage, Wait stage, and Necking stage can be recognized. However, the Detachment stage disappears in all waveforms.
- CTWD does not affect the Pulsing current time (t_p), Droplet detachment current (I_d), Ground current (I_g), and Pulse current (I_p)in the Synergic Line. In contrast, the Droplet-detachment time (t_d) is the only response to CTWD, which decreases with the increase of the CTWD.

In the later experiment in this study, the CTWD is set to 15 mm constantly because in Table 13, the average current (I_a) and the average voltage (U_a) reach their lowest value at CTWD = 15 mm, meaning setting CTWD to 15 mm can bring the lowest energy input, which is suitable for mitigating heat accumulation and improving aluminum welding layer's quality [90].

5.3 Exploring the Proper WFS and TTS for Sound Geometrical Property

5.3.1 Experimental Design

As introduced in Section 5.1, the main goal of this chapter is to find the best WFS and TTS combination that can lead to sound geometrical properties of 7075NT aluminum alloy in WAAM. The satisfied parameter set should fulfill both the following criteria:

- **Criterion 1: Visual assessment.** The layer fabricated by the chosen parameter set should have a consistent layer geometry.
- **Criterion 2: Energy consumption.** The layer fabricated by the chosen parameter set should have less energy consumption.

Based on these two criteria, an experiment needs to be designed to physically print several layers to observe their appearance and calculate the energy consumption. In the study of Gomez et al. [48], the proper TTS = 14 in/min for fabricating aluminum alloy in the WAAM process has been investigated. Therefore, herein, TTS = 14 in/min is fixed. WFS is the only parameter that needs to be tuned to fit the two criteria.

The detail of the design of the experiment is listed in Table 14. The first column of the table shows eight levels of WFS, which is the only parameter (factor) in this experiment. The range and levels of WFS designed in this experiment are the same as the WFS range and level in Table 12 in section 6.2.2. The second and third columns in Table 14 are current and voltage recorded during the process. The fourth and fifth columns are heat input and layer weight calculated based on Eq (6) and Eq (5); The last column is the energy consumption calculated based on Eq (3). CTWD = 15 and layer length (L_{layer}) = 100 mm were set as constant in the experiment. So, the heat input (HI), duration of depositing a layer (t_{layer}), and the weight of layer (W_{layer}) are functions of the only variable WFS. Therefore, there is only one specific energy consumption corresponding to each WFS as expressed in Eq (11).

$$\text{Energy Consumption} = f(WFS) \tag{11}$$

The weight of layer (W_{layer}) is measured by scaling the weight of substrate before the printing and the weight of substrate and printed layer after the printing. Simply speaking, the weight of layer (W_{layer}) is the difference of the substrate before and after the printing, as expressed in Eq (12).

$$W_{layer} = W_{part} - W_{subsrate} \tag{12}$$

Table 14. The energy consumption at the different WFS.

WFS (in/min)	Current (A)	Voltage (V)	HI (J/mm)	Layer Weight (g)	Energy Consumption (J/mm·g)
80	45.45	9.77	54.73	0.68	8048
100	44.77	9.99	60.44	1.27	4759
120	49.48	10.69	71.48	1.77	4038
140	59.37	10.66	85.52	2.13	4014
160	71.66	10.73	103.91	2.87	3620
180	80.89	11.22	122.65	3.42	3586
200	97.15	13.83	181.57	4.07	4461
220	121.23	14.86	243.44	4.56	5339

5.3.2 The Analysis of the WFS on the Layer Geometrical Property

The top view of the layers printed at eight WFS levels is plotted in Figure 34. By visually observing, these layers can be classified into three categories: discrete layers (layer 1 and layer 2), non-continuous layers (layer 3 and layer 4), and continuous layers (layer 4 to layer 8). The discrete layers are the layers that do not form a complete continuous layer but are comprised of multiple individual droplets distributed along the deposition path. These layers are unqualified with respect to the geometrical property and are undesirable for WAAM. The non-continuous layers are the layers that have gaps at some points of the deposition path, but most sections of the layer are continuous. This is considered a major defect in the WAAM process. This is because the WAAM fabricates the part in a layer-by-layer method like other AM technologies, which means the accumulation of a minor geometrical defect in a layer could be magnified in the upcoming layers and finally cause a significant defect of the wall. Thus, even a minor defect on a single layer in WAAM needs to be prevented. The continuous layers are the layers that we expect to bring good geometrical properties. These layers do not have any gaps or break points along the layer. Their width and height are consistent without any ripples on the top of the layer. However, from layer 7 and layer 8 in Figure 34, it is also noticeable that although they are continuous layers, their surface is covered by a thick, dark layer. This dark layer may be the carbonized particle from the nano-

ceramic particle in the nano-treated 7075 aluminum alloy. From the trials in this study, it is empirically concluded that this kind of dark layer can cause a hard arc-on of the CMT welding. The unstable arc-on is fine for welding a single layer on the plate but could cause a severe slump in the WAAM process. So, it is better to avoid the generation of this dark layer.

The energy consumption at the different WFS was plotted in the chart of Figure 35 based on the calculated energy consumption shown in Table 14. With the increase of the WFS, the curve of energy consumption presents a "U" shape. The highest energy consumption is at the lowest WFS = 80 in/min. Then, the energy efficiency keeps going down until it reaches the lowest energy consumption = 3586 J/mm·g at WFS = 180 in/min. WFS = 180 in/min is a turning point of energy consumption. After WFS = 180 in/min, energy consumption increases with an increase in WFS. energy consumption is defined as the consumption of the heat input per gram of 7075NT aluminum alloy. Therefore, a lower energy consumption means the WAAM system will consume less energy for printing the same mass (or volume) of material. Thus, the lowest energy consumption is located at the bottom of the curve where WFS = 180 in/min is preferred.

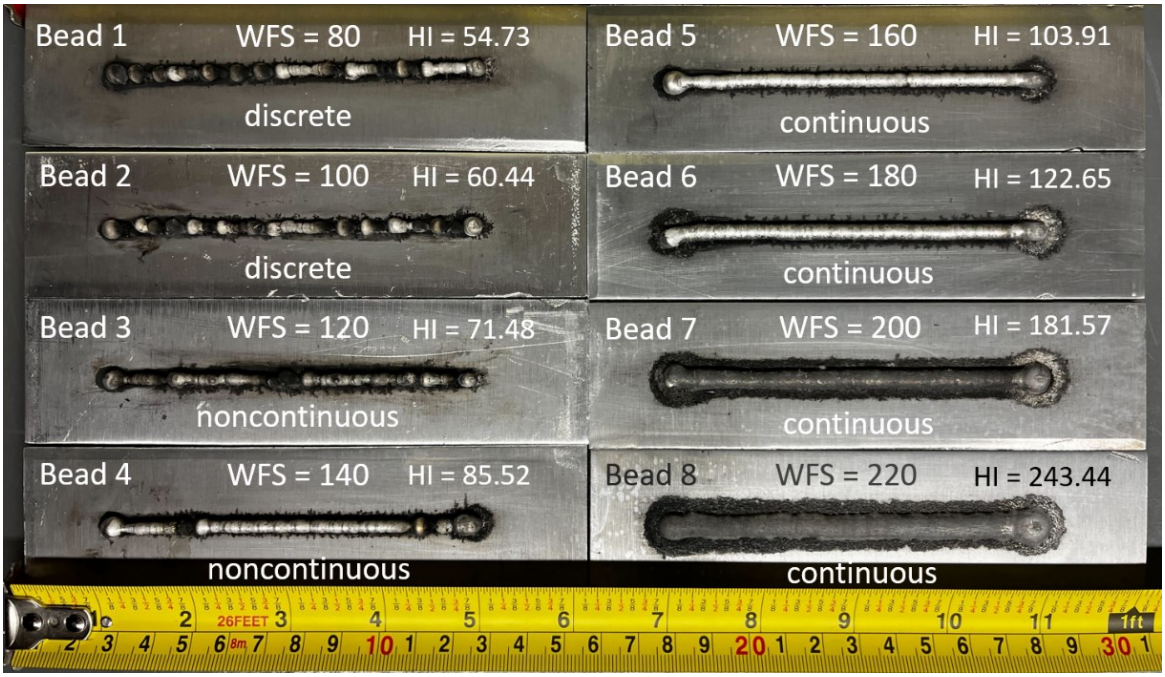

Figure 34. The top view of the layer at the different WFS.

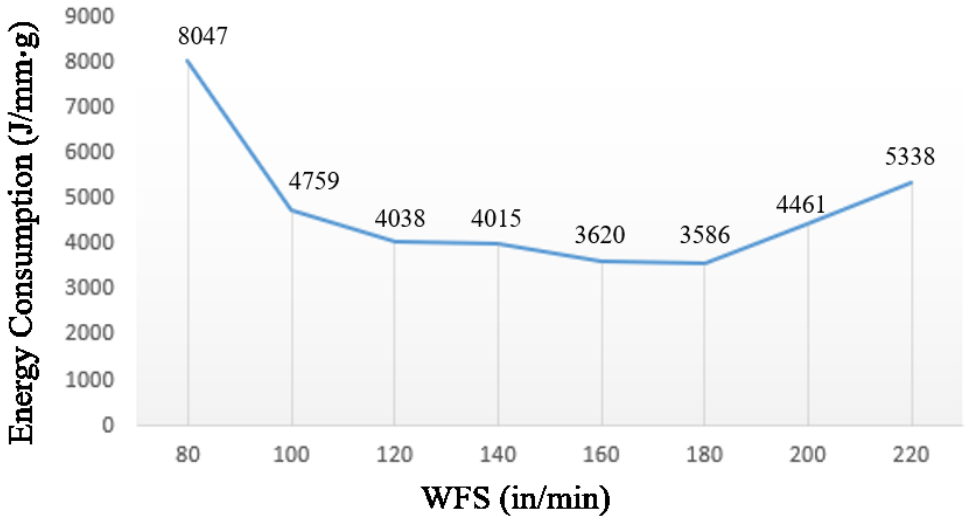

Figure 35. The Energy consumption at the different WFS.

5.3.3 Conclusion

In this experiment, the ideal WFS that leads to a consistent weld bead was explored.. The chosen WFS will be then used as a constant for a fixed heat input in further experiments in this study to control the interpass temperature. To select a proper WFS, two criteria were used: layer geometry property and energy consumption. From the results, two sound layers are formed at the WFS = 160 in/min and 180 in/min, and the lowest energy consumption can be obtained at the WFS = 180 in/min. Thus, a WFS of 180 in/min fits both criteria and can be considered the proper WFS in future experiments.

5.4 Chapter Conclusion

In this chapter, two experiments were conducted to explore the effect of WFS and CTWD on the CMT current and voltage (Synergic Line) and how WFS affects the layer geometry and process energy consumption. Based on the experimental results and two criteria, the following process parameters were chosen to obtain the consistent bead quality and lowest energy consumption in the CMT-based 7075NT aluminum alloy fabrication process:

Table 15. The best-fitted parameter set in the CMT-based 7075NT aluminum alloy fabrication process.

WFS (in/min)	TTS (in/min)	CTWD (mm)	Energy consumption (J/mm·g)	HI (J/mm)
180	14	15	3586	122.65

This parameter set will be used in the later experiment for investigating the heat management strategy in the WAAM process. The heat input (HI) for this parameter set is also listed in the last column in Table 15. To investigate the heat management strategy, the heat ejected into the part during the process must be controlled. Also, by knowing the heat input (HI), the calculation of more complicated heat transfer behavior can be possible in the future.

6. Heat Management and Quality Control

6.1 Introduction

From the results of the screening experiment in Chapter 4, it is known that the interpass temperature is a significant factor affecting the part's geometrical properties. So, in this chapter, the effect of interpass temperature on the geometry of the build will be explored. First, the weldability of 7075NT aluminum alloy in the WAAM process was validated. Second, the heat accumulation in the manufacturing part was controlled by two heat management strategies: Critical Dwell Time and Critical Interpass Temperature. The Response Surface Method (RSM) was used to analyze the relationship between the two heat management strategies and geometrical properties. The geometrical properties and the temperature of each layer during the process were recorded by the monitoring modules that integrated into the WAAM system. Finally, the mechanical properties were measured using tensile testing. The relationship between the WAAM-made 7075NT aluminum alloy build quality and two heat management strategies was given.

6.2 Design of Experiment

In this study, six single-track multi-layer walls, which consisted of 25 layers and 120 mm length for each layer, were printed on the substrate at room temperature (23℃). Each layer was deposited in a bi-directional trajectory, as illustrated in Figure 36. The torch moved up in 2.5 mm Z-offset after the current layer was deposited. The Contact tip-to-workpiece distance (CTWD) was set to 15 mm. The shielding gas was pure argon at a flow rate of 35 CFH. The emissivity of the IR camera used in this experiment was set to 0.9 since based on the testing result from Chapter 3, the emissivity doesn't varied too much with the temperature.

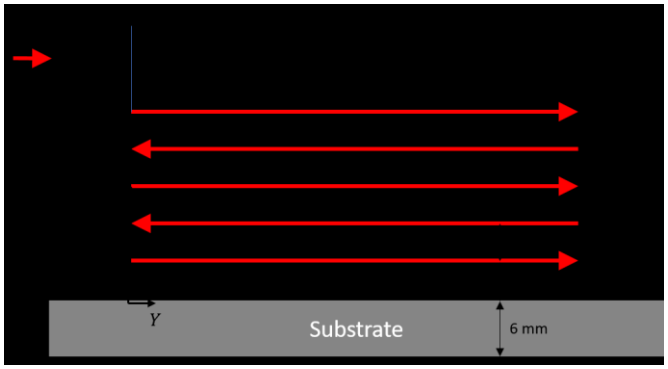

Figure 36. The printing trajectory of the part used in this study.

Heat management strategies, critical dwell time and critical interpass temperature, are two essential methods in this chapter to control the interpass temperature during the printing process. However, many factors in the WAAM process may influence the thermal state of each layer, such as the substrate pre-heat temperature, current and voltage, torch travel speed, and arc correction [8][9][18]. To understand the effect of interpass temperature on the build geometry, only dwell time and interpass temperature will be varied. All other parameters will remain constant.. The parameters used in this experiment are listed in Table 15. The heat input (HI) at the given WFS and TTS was then calculated to 122.65 J/mm, which is the same as what was calculated in the last chapter. Besides setting the constant heat input, the following factors that may affect the heat dissipation were also set to constant. For example, the size of the substrates used in this experiment is six by three inches. The ambient temperature is the room temperature before the process, and the printing process was carried out in a stable air-flowing lab environment without any compulsory cooling approaches.

A general WAAM printing process is the finite repetition of printing one single layer. Figure 37 shows the procedure of printing one single layer in this study. At the start, the new layer is deposited. At the time the new layer is completely deposited, the profiler starts scanning the new layer. Then, the process enters the heat management strategy judgment phase (the diamond patches in Figure 37). Herein, the clear definition of the terms “dwell time” and “interpass temperature” is given:

- **Dwell time**: the duration between the end of scanning and the printing of the next layer.
- **Interpass temperature**: the temperature of the latest deposited layer.

Moreover, the definition of the two heat management strategies is also given:

- **Critical Dwell Time strategy**: once the dwell time reaches the predetermined dwell time called Critical Dwell Time, the print of the next layer is triggered.
- **Critical Interpass Temperature strategy**: once the interpass temperature reaches the predetermined interpass temperature called Critical Interpass Temperature, the print of the next layer is triggered.

The essential difference between these two strategies is the different boundary conditions. In Critical Dwell Time strategy, the dwell time is the only fixed factor. The interpass temperature is uncontrolled. It can be assumed that with the continued number of layers, the volume of the part

increases, and the heat dissipation increases as well. The heat accumulated in part is varied, which may affect the quality of as-printed parts. However, in Critical Interpass Temperature strategy, the interpass temperature is fixed, meaning the heat accumulation in the latest printed layer is fixed, which may also affect the quality of the part.

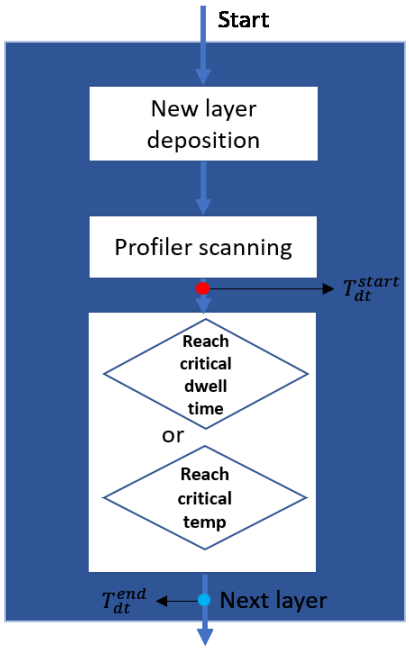

Figure 37. The procedure of printing one single layer was applied in this study.

Two experiment groups were designed to correspond to the two heat management strategies. Table 16 shows the detail of the design of the experiment. The Critical Dwell Time strategy is applied in Group 1. Three critical dwell time levels, in two-fold increments, were set. Group 2 was designed for the Critical Interpass Temperature strategy. Three critical interpass temperatures were set with 100℃ increments.

Table 16. The critical dwell time and critical interpass temperature designed in the experiment.

	Group 1			Group 2		
Critical Dwell Time (s)	15	30	60		-	
Critical Interpass Temp (℃)		-		150	250	350

6.3 Result and Analysis

6.3.1 The Analysis of Geometrical properties

Due to the unstable arc-on and arc-off phase, the 20 mm long unstable arc-on and arc-off sections on the two ends of the wall are removed. Only the 80 mm stable deposition section (middle section) of the wall is retained to analyze in this study.

The weldability of 7075NT aluminum alloy used in the WAAM process was validated at first. Figure 38 shows the appearance and the shape of the stable deposition section of the WAAM-made 7075NT aluminum alloy parts with two heat management strategies at different critical dwell times and critical interpass temperatures. Although the surface appearance and geometry are distinct, all of these parts exhibit successive overlapping layers. This result indicates that the WAAM method can successfully print the 7075NT aluminum alloy walls without any fatal geometrical defects. Therefore, the weldability of aluminum alloy used in the WAAM process can be validated.

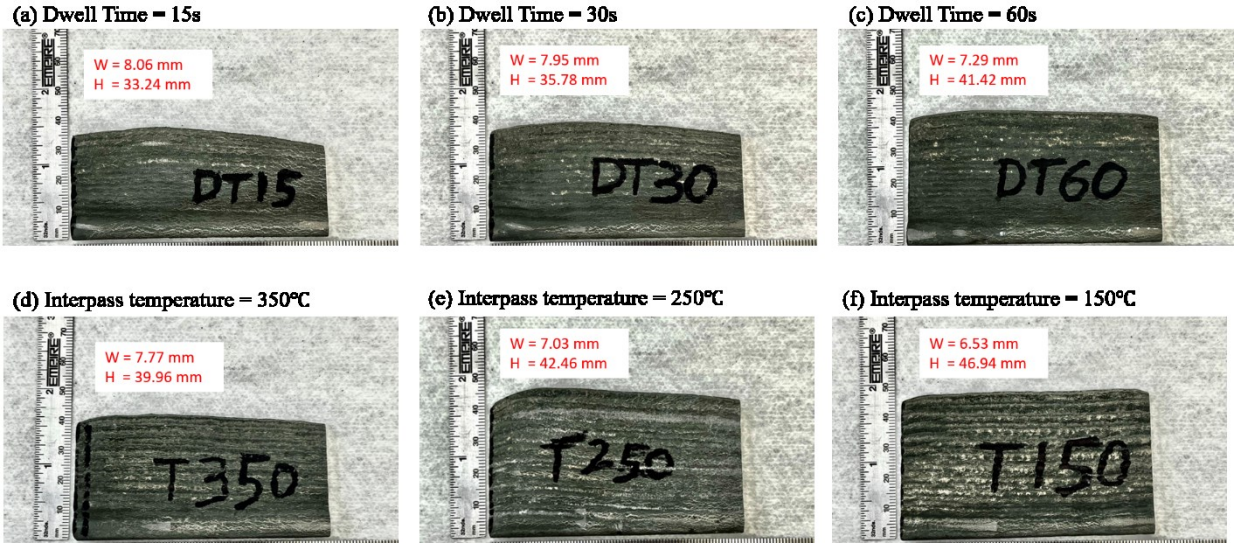

Figure 38. The appearance of the WAAM-made 7075NT aluminum alloy walls with two heat management strategies at different critical dwell times and critical interpass temperatures.

The height and width of each build was measured and are shown in Figure 39. The variation in each wall along the width and height is also noted. Figure 39 (a) shows the basic geometrical properties of the walls that submit to the Critical Dwell Time strategy. A noticeable pattern is that both the wall width and height are small at a short dwell time. The median value of the wall width

does not have a clear relationship to the change of the critical dwell time, but the middle height exhibits an apparent positive correlation to the dwell time. Figure 39 (b) shows the basic geometrical properties of the walls that submit to the Critical Interpass Temperature strategy. The wall width and height are smaller at a greater critical interpass temperature. In contrast, the wall width and height median values at the different interpass temperature levels do not show a clear pattern.

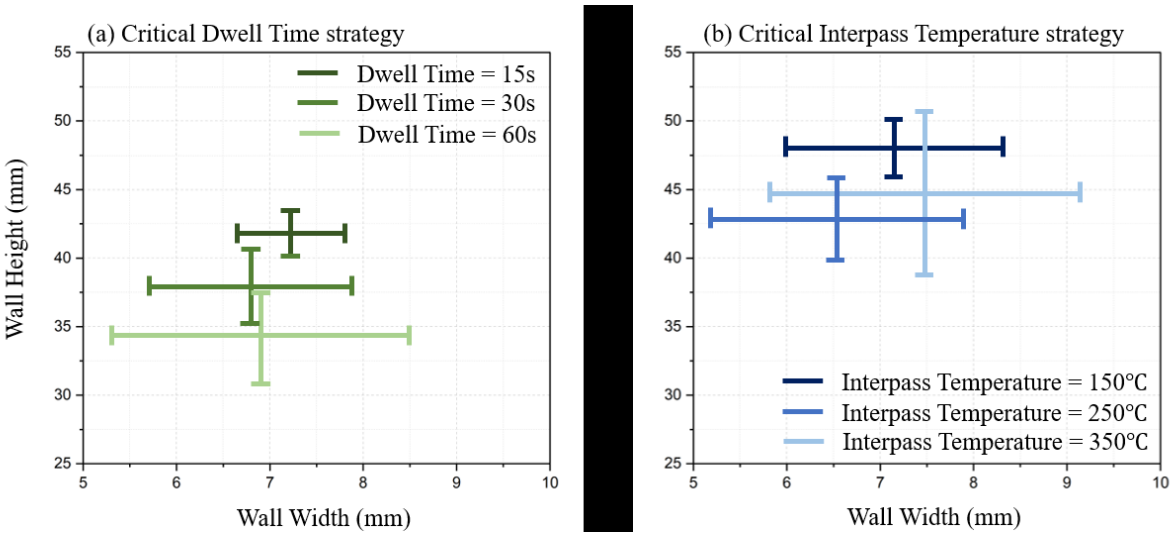

Figure 39. The range of the wall height and width of (a) Critical Dwell Time strategy and (b) Critical Interpass Temperature strategy.

More geometrical properties of these walls need to be measured and examined to establish the relationship between the two strategies and the part's geometrical properties. Because the layer-by-layer deposition approach is used in AM, the overall geometrical property of a part is a function of the geometrical property of each layer. Therefore, it is necessary to analyze how these two strategies and critical factor levels affect the geometrical property of each layer first. By taking advantage of the profiler, the contour of each layer of the wall was collected. Figure 40 shows the profiler scanning method used in this study. When the new layer is deposited, the profiler starts scanning the middle section of the new layer along the printing direction (X-axis). A total of 35 contours in each layer are collected. In the post-processing, the average contour of each layer was calculated. A total of 25 average contours were plotted in one frame to comprise a wall's cross-section, like each subplot in Figure 41.

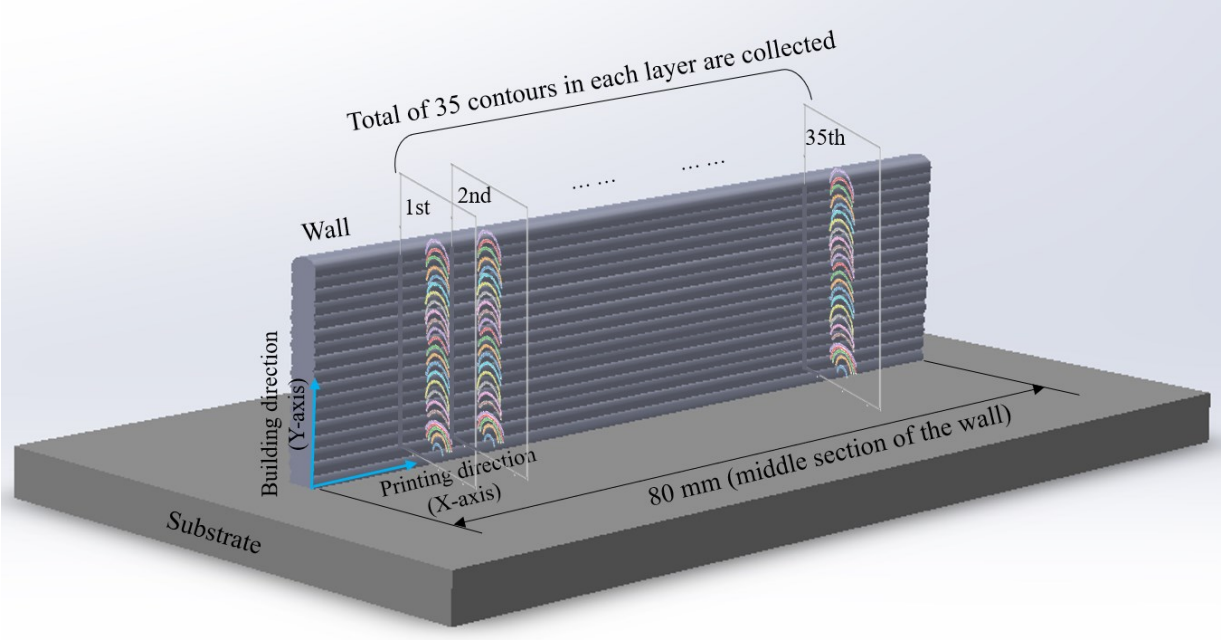

Figure 40. The profiler scanning method of layer contours.

From Figure 42, the different heat management strategies and critical factor levels result in layers with geometrical properties that are significantly distinct between each wall. To quantify the layer's geometrical properties, the terms "layer height," "layer width," and "layer height-to-width ratio" were used. To quantify the wall's geometrical properties, the terms "wall height," "wall width," and "wall centerline deviation" were used. A good geometrical quality of the WAAM-made part in this study is defined as follows:

(1) Have as consistent a layer height and width as possible. Consistent layers could lead to a consistent wall height and width in the layer-by-layer based WAAM process.

(2) Have as larger a layer height-to-width ratio as possible. Unlike cladding processes, which aim to cover more material onto the part surface (X and Y axes plane), AM processes aim to efficiently manufacture parts along the Z axis.

(3) Have as small a wall centerline deviation as possible. The wall centerline deviation represents the incline and distortion of the as-printed wall. A larger wall centerline deviation indicates a small Effective Wall Width (EWW) [24], resulting in lower material utilization.

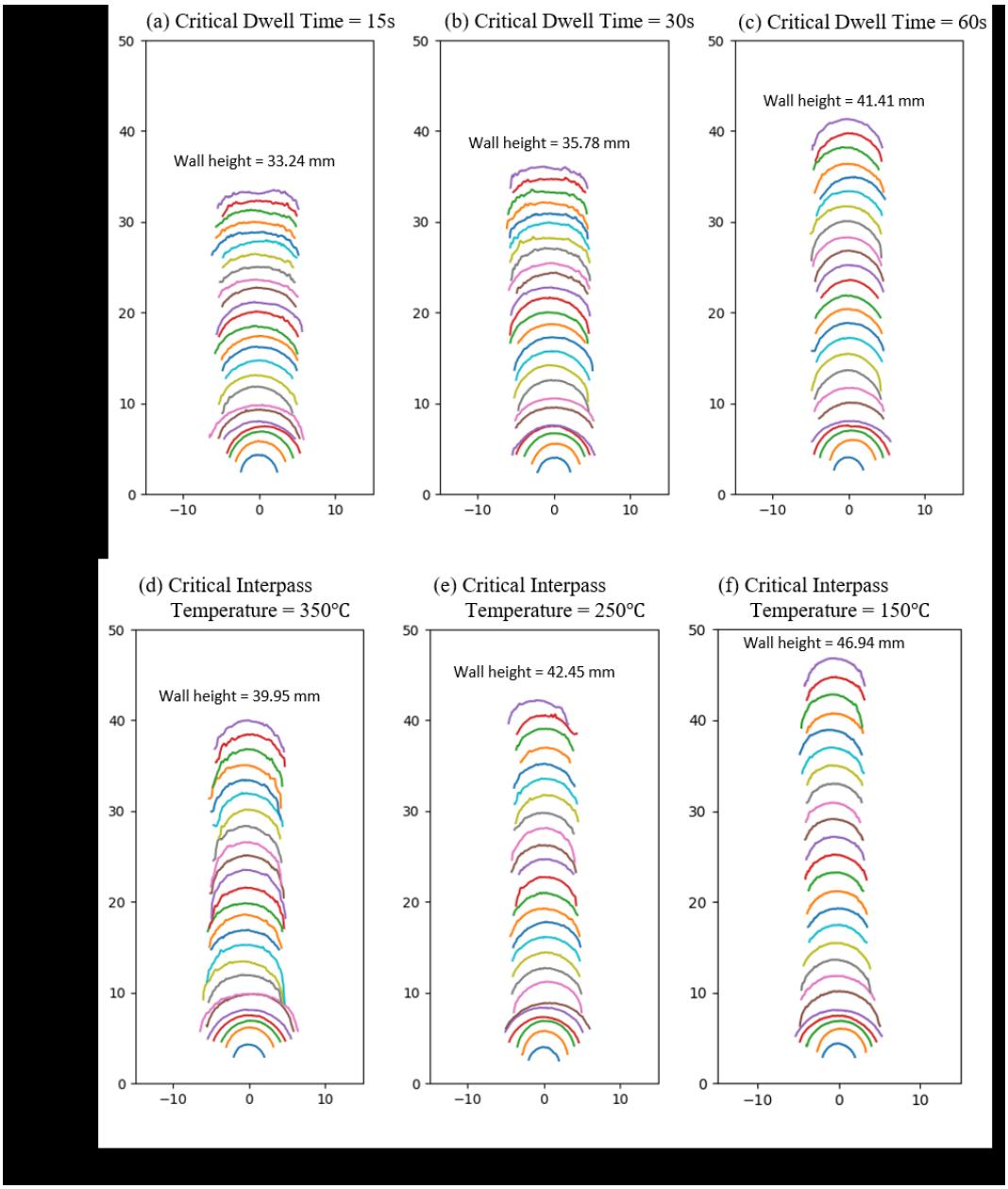

Figure 41. The average wall cross-section for each wall.

Figure 42 shows the layer height and width for different strategies and critical factor levels. In each subplot, the red and blue dots represent the height and width of the layer, respectively. Two common patterns in all six subplots can be easily found: (1) The height and width dots are roughly symmetrical distributed around the 4 mm, taking up the bottom and top portion of each subplot. (2) The height and width start at 4 mm, resulting in a layer height-to-width ratio equal to 1 when the first layer is deposited. But as the number of layers increases, the height sharply decreases while the width increases, indicating a low layer height-to-width ratio.

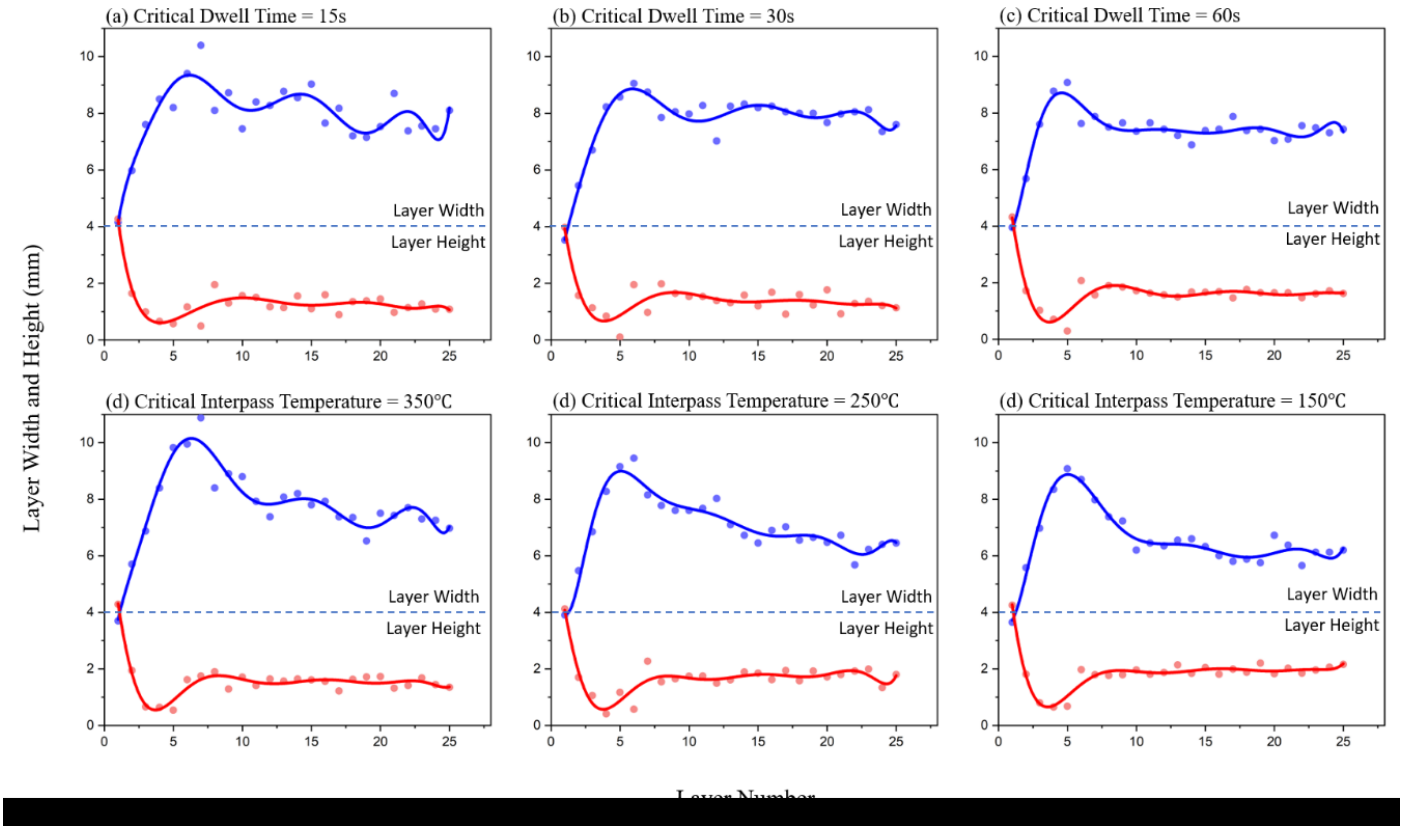

Figure 42. The layer height and width for different strategies and critical factor levels.

The definition of the layer height-to-width ratio is the ratio of the maximum layer height (h_i) to layer width (w_i), which is illustrated in Figure 43 (a). The layer height-to-width ratio of each layer for the two strategies is shown in Figure 44. The greater layer height-to-width ratio, the more vault-shaped the cross-section of the layer is. Conversely, the smaller the layer height-to-width ratio, the flatter cross-section the layer has. By observing the plots in Figure 44, the ratio slightly greater than one only appears at the 1st layer, and for the rest of the layers, all ratio values are small than 1. This means, except for the 1st layer, all the rest of the layers, regardless of the strategy, have a flat vault shape with a larger layer width than layer maximum height. Moreover, in both strategies, the layer drastically drops to around 0.3 at the 2nd layer and keeps decreasing slightly until the 5th layer. Then there is a quick flip and the layer ratio reaches a stable value at the 8th layer. After the 8th layer, the ratio tends to keep stable. Therefore, the layer height-to-width ratio can be divided into two phases. The 8th layer is an interface: before the 8th layer, the ratio is unstable. Including and after the 8th layer, the ratio stabilizes to a stable value. The value of the stable height-to-width ratio depends on the strategy and level. The stable height-to-width ratio at the different critical

dwell times and critical interpass temperatures are shown on the right side of each plot in Figure 44. A greater dwell time and lower interpass temperature can lead to a greater height-to-width ratio.

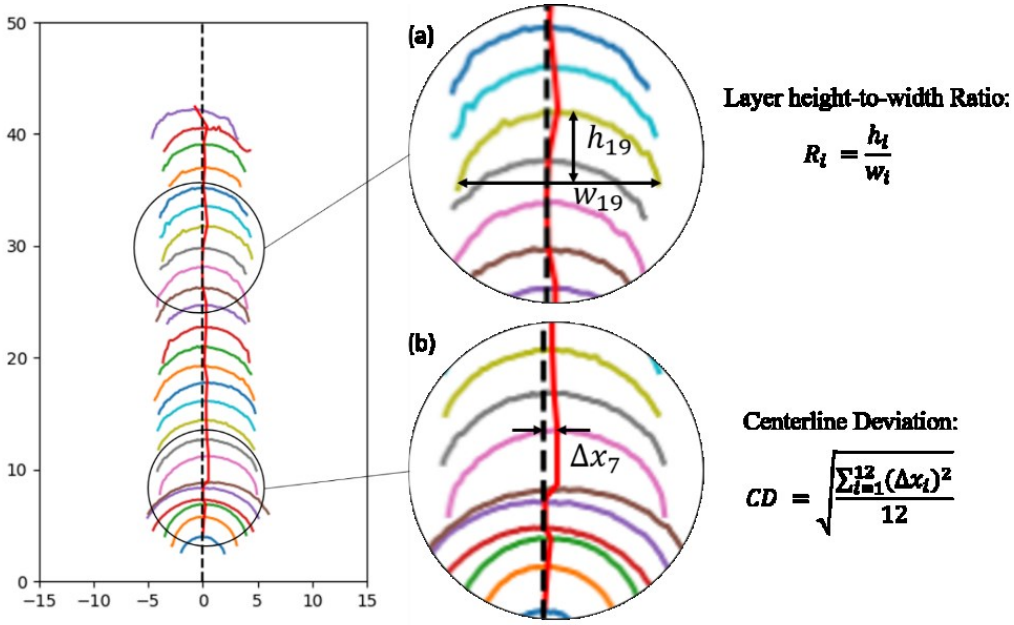

Figure 43. The definition of (a) the layer height-to-width-ratio and (b) centerline deviation.

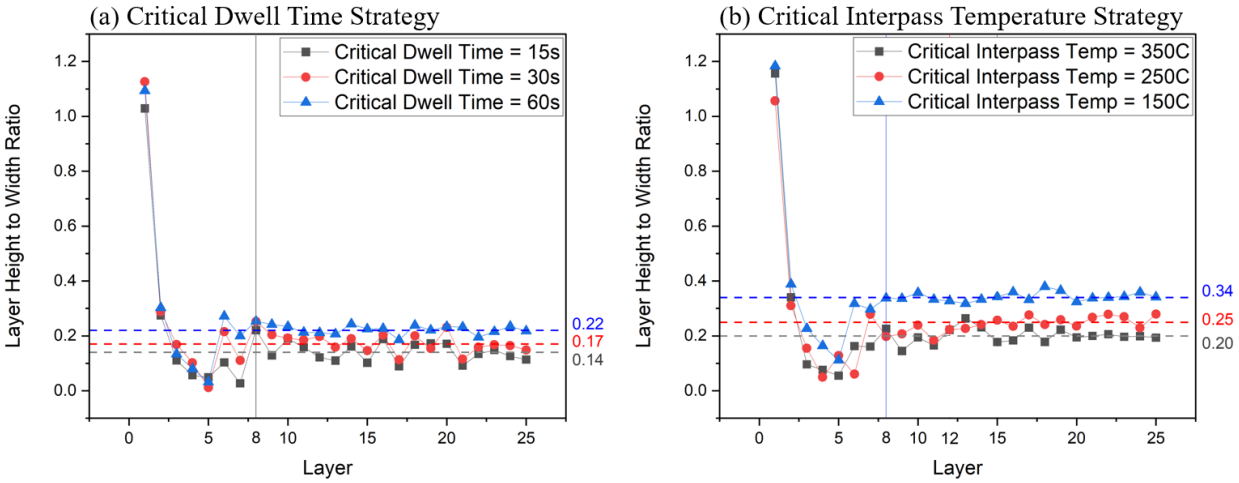

Figure 44. The layer height-to-width ratio for different strategies and critical factor levels.

In each subplot of Figure 42, the distribution of the blue and red dots also varies with the number of layers. Based on that, the non-linear polynomial fitting of layer height and width for different critical levels was plotted as the red and blue curves in Figure 42. For both height and width measurements, the faster they achieve steady state, the more geometrically consistent the wall. All the measurements start at 4 mm but diverge rapidly until the 5^{th} layer. Then, the two curves have a slight fluctuation but tend to keep stable with the increase of layers, which has an almost identical pattern in Figure 44. However, the shapes of the blue curves are different depending on the strategy and the specified critical level. In Critical Dwell Time strategy, when critical dwell time is 15s, the curve fluctuates after an overshoot and it cannot converge even after printing the last layer. With the increase of the critical dwell time, when critical dwell time is 60s, the curve shows a quick convergence and keeps stable until the last layer. In Critical Interpass Temperature strategy, the general shapes of curves show a gradual decline until reaching the stable phase. When critical temperature is 350℃, the decline is in waves. At 250℃, the waviness is not noticeable anymore. At 150℃, the waviness is not easy to recognize. It can be seen that both the critical dwell time and the critical interpass temperature have an effect on the wall height and width and result in different geometrical properties.

The wall geometrical properties depend on the layer geometrical properties, meaning the accumulation of a small geometrical change in each successive layer could finally cause a significant difference in a wall. The factors “wall average height,” “wall average width,” and “wall centerline deviation” are analyzed for each wall, and the results are shown in Table 17 and the diagram is made, as shown in Figure 45, based on the data in Table 17. The wall average height increase and width decrease with increased dwell time and decreased interpass temperature. This tendency matches the layer height and width results above. Moreover, a longer dwell time or a lower interpass temperature results in a greater layer height-to-width ratio, further leading to a greater wall height-to-width ratio. A lower wall centerline deviation is also an aim of the quality control of the WAAM process. Figure 43 (b) defines the term “wall centerline deviation.” The results of the wall centerline deviation are listed in the last three rows in Table 17. The smaller the centerline deviation of the wall, the better the wall geometrical quality of the wall. From the results, the lowest centerline deviation is at 60s and 150℃ in the two strategies, respectively. The centerline deviation has a negative correlation with the critical dwell time, but a positive correlation with the critical interpass temperature. The mean standard deviation of each

geometrical property before and after the 8th layer is also listed in Table 17. The mean standard deviation indicates the variation from the average (mean). Therefore, all geometrical properties of layers before the 8th layer have greater mean standard deviation than those after the 8th layer, meaning layers after the 8th layer have much better geometrical stability than the first seven layers.

A conclusion can be made that the 7075NT aluminum alloy is compatible with the WAAM process. By applying two heat management strategies, each wall's layer geometrical properties vary with the different critical dwell times and critical interpass temperatures. The best wall geometry in this study appears at the longest critical dwell time (60s) and the lowest critical interpass temperature (150℃) in the two strategies, respectively. Regardless of strategy and level, the geometrical properties have a significant distinction before and after the 8th layer.

Table 17. The walls' geometrical properties.

	Wall geometrical properties	Critical Dwell Time			Critical Interpass Temperature		
		15s	30s	60s	350℃	250℃	150℃
Wall height	Wall average height (mm)	33.243	35.782	41.415	39.955	42.458	46.942
	height dev of layers 1-7	1.248	1.197	1.563	1.247	1.199	1.431
	height dev of layers 8-25	0.331	0.233	0.152	0.204	0.288	0.153
Wall width	Wall average width (mm)	8.061	7.954	7.292	7.772	7.028	6.5282
	width dev of layers 1-7	1.534	1.477	1.587	1.430	1.407	1.399
	width dev of layers 8-25	0.374	0.252	0.202	0.284	0.271	0.246
Height-to-width ratio	Wall height-to-width ratio	4.122	4.503	5.687	5.143	6.055	7.195
	ratio dev of layers 1-7	0.352	0.380	0.363	0.393	0.352	0.395
	ratio dev of layers 8-25	0.037	0.036	0.017	0.028	0.042	0.017
Centerline deviation	Wall centerline deviation	0.306	0.311	0.269	0.319	0.269	0.253
	centerline dev of layers 1-7	0.307	0.125	0.153	0.168	0.153	0.226
	centerline dev of layers 8-25	0.288	0.234	0.226	0.240	0.226	0.265

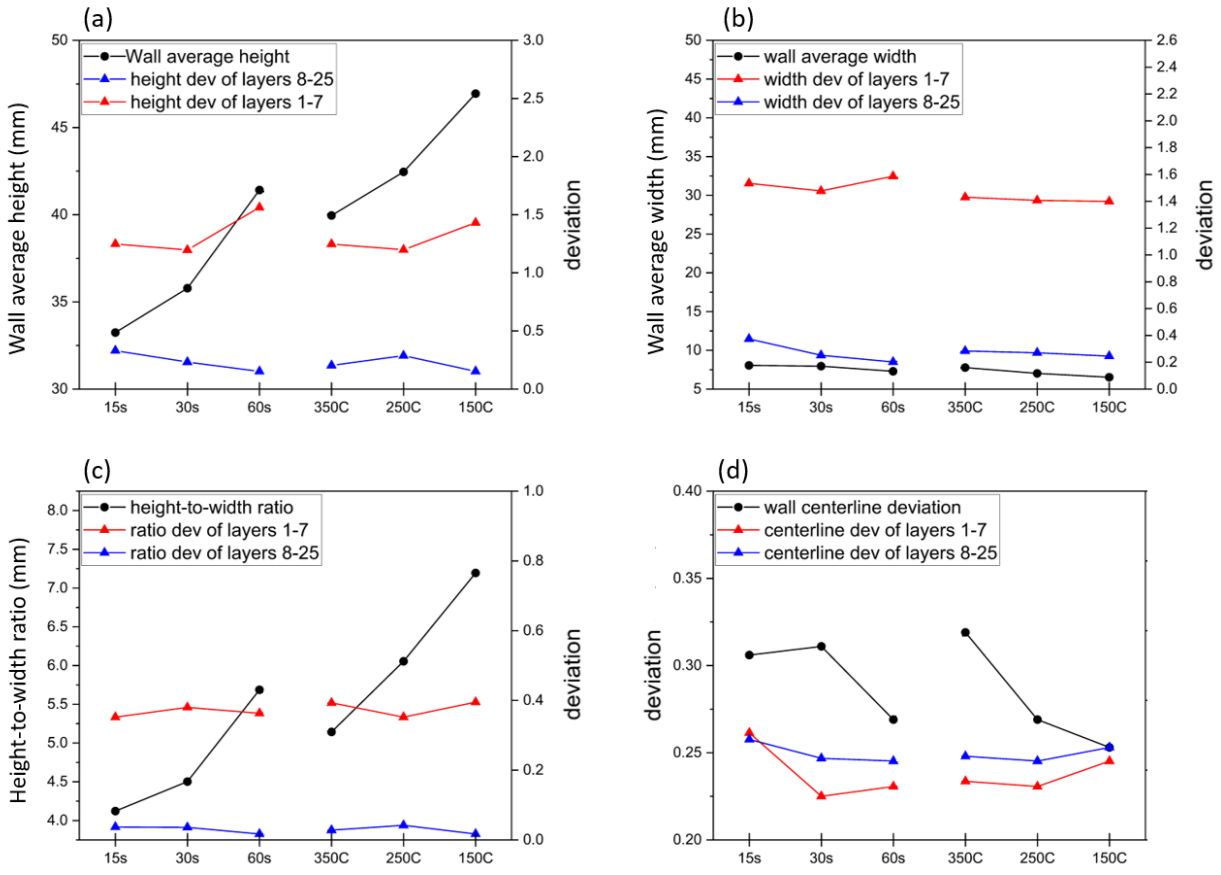

Figure 45. The mechanical property of (a) wall average height, (b) wall average width, (c) height-to-width ratio and (d) wall centerline deviation.

6.3.2 The Analysis of Heat Accumulation on Part's Geometrical Properties

The correlation between heat accumulation (Q) and two heat management strategies is illustrated in Figure 46. The heat accumulation (Q) can be simply modelled as a function of heat input (Q_{input}) and heat dissipation ($Q_{dissipation}$). In this experiment, the process parameters are constant. Therefore Q_{input} is set at a constant 122.65 J/mm. The only variable affecting Q is $Q_{dissipation}$ which is managed by two strategies. Once dwell time increases or interpass temperature decreases, $Q_{dissipation}$ increases via heat conduction, convection, and radiation, leading to a decrease of Q.

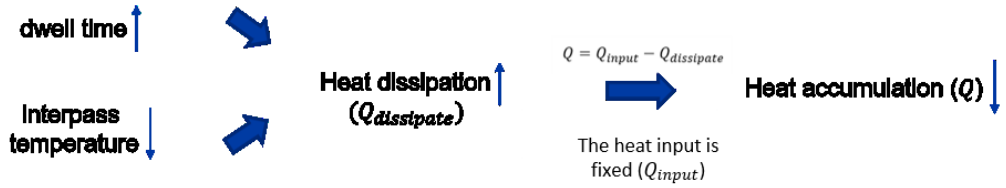

Figure 46. The illustration of the correlation between heat accumulation and two heat management strategies.

Eq (13) was used to quantify $Q_{dissipation}$. In this study, m is the mass of each layer. c is the specific heat capacity of 7075NT aluminum alloy, and ΔT is the change of the interpass temperature. Because all layers were printed in this study using constant WFS and TTS. The material used in the study was never changed. m and c_p are constant for each layer. Thus, ΔT of the layer is proportional to $Q_{dissipation}$. The trend of the ΔT can represent the trend of the $Q_{dissipation}$, although $Q_{dissipation}$ cannot be calculated since c of this new material is unknown

$$Q_{dissipation} = mc_p|\Delta T| \tag{13}$$

Figure 47 plots the interpass temperature and the cooling rate at different dwell time levels in the Critical Dwell Time strategy. The first row in the figure shows the range of the interpass temperature during the dwell time. The red spots are T_{dt}^{start} and the blue spots are T_{dt}^{end}. T_{dt}^{start} and T_{dt}^{end} wich are illustrated in Figure 37. The interpass temperature and cooling rate were calculated based on Eq (14) and Eq (15) and are drawn in the second column of Figure 47.

$$\Delta T = T_{dt}^{end} - T_{dt}^{start} \tag{14}$$

$$Cooling\ rate\ = \frac{\Delta T}{dwell\ time} \tag{15}$$

In Critical Dwell Time strategy, interpass temperature keeps increasing until around the 5th layer. Then a slight fluctuation occurs until the 8th. After the 8th layer, the tendency of the interpass temperature varies depending on the dwell time applied. In the case of critical dwell time equal to 15s, the interpass temperature keeps increasing until the last layer is deposited. In the case of critical dwell time equal to 30s, the interpass temperature keeps climbing but turns stable after the 18th layer. When the critical dwell time is equal to 60s, the interpass temperature quickly stabilizes at the 7th layer. ΔT and cooling rate present a similar trend. They increase in the first few layers and start to converge around the 8th layer. With the increase in dwell time, ΔT rises as well, leading to $Q_{dissipation}$ increases and Q decreases.

Figure 48 shows the temperature of the substrate (T_{sub}) at different dwell times in Critical Dwell Time strategy. In the plot, each temperature profile consists of 25 spikes. Each spike represents a thermal cycle of a layer during the process. It can be seen in all subplots that the spikes are sharp in the first few layers but obtuse after around the 8th layer. This pattern indicates the heat accumulation does not change pronouncedly after the 8th layer, implying the heat conduction between the wall and substrate dominates the change of heat accumulation in the first seven layers, but its leverage is lost gradually when the number of layer increases.

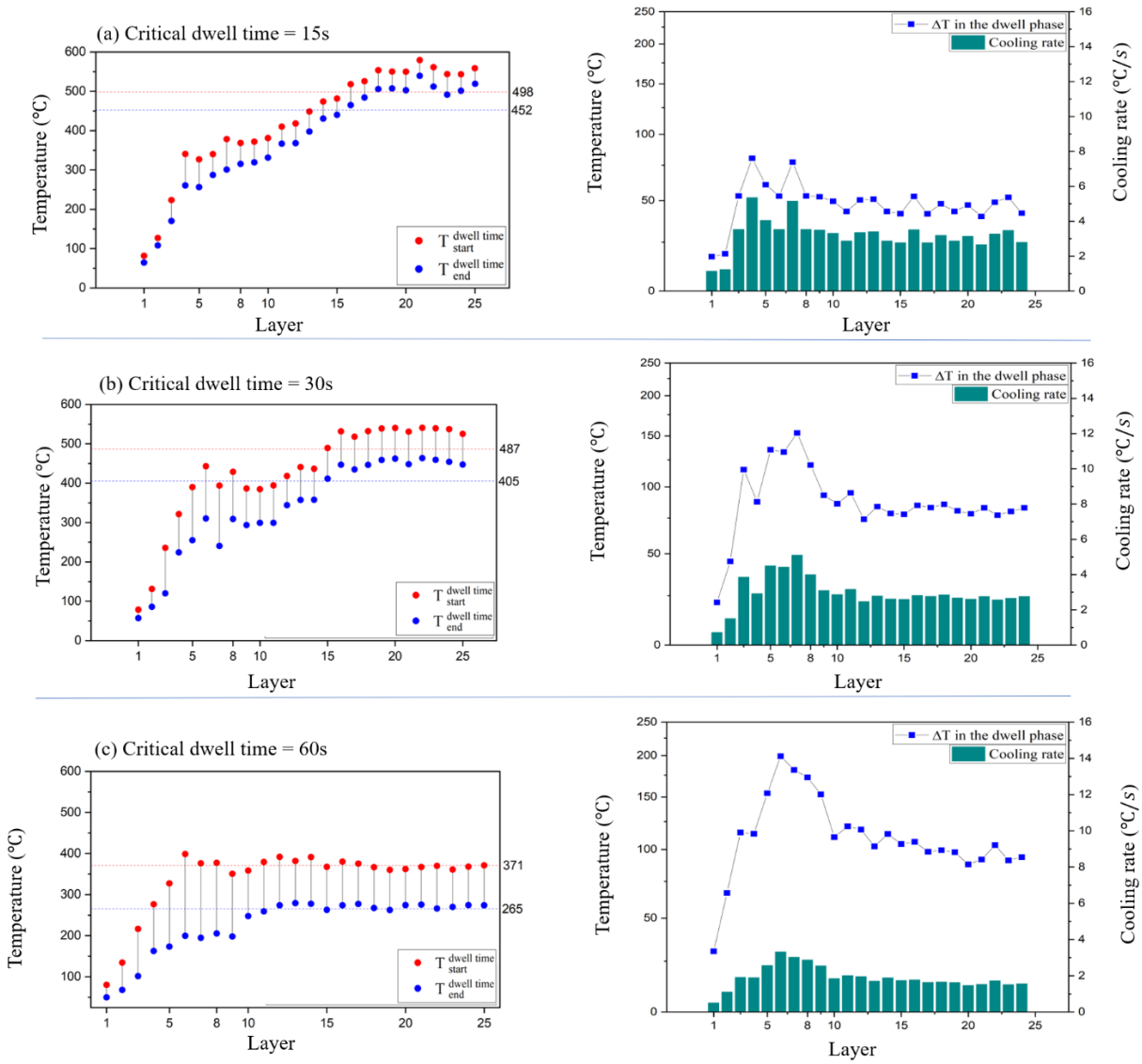

Figure 47. The interpass temperature and cooling rate in Critical Dwell Time strategy.

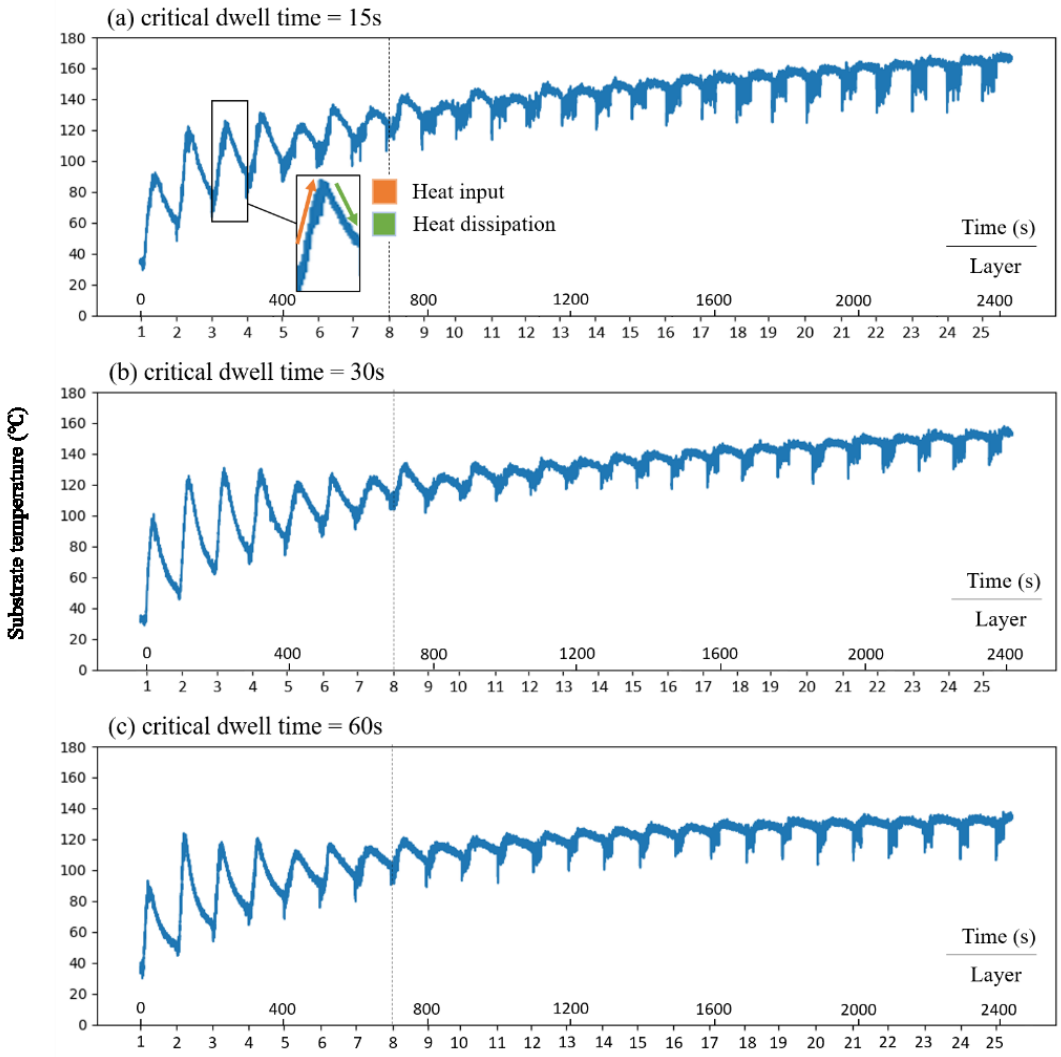

Figure 48. The substrate temperature in Critical Dwell Time strategy.

Figure 49 and Figure 50 show the interpass temperature and substrate temperature in Critical Interpass Temperature strategy. In Figure 49, some blue spots are missing in the first row of the figure since the actual interpass temperature right after the deposition is lower than the critical interpass temperature. The printing of the next layer is immediately triggered so that the T_{dt}^{end} was not recorded. Therefore, the dwell phase is skipped and the dwell time does not exist. The pattern of the interpass temperature, ΔT, and cooling rate is similar to the pattern in Critical Dwell Time strategy. However, depending on the critical interpass temperature, the results tend to be stable at the 13th, 9th, and 12th layers, when the critical interpass temperature was set to 350℃, 250℃, and 150℃, respectively. In Figure 50, spikes become obtuse at the 8th, 8th, and 6th layers when critical interpass temperatures are 350℃, 250℃, and 150℃, respectively.

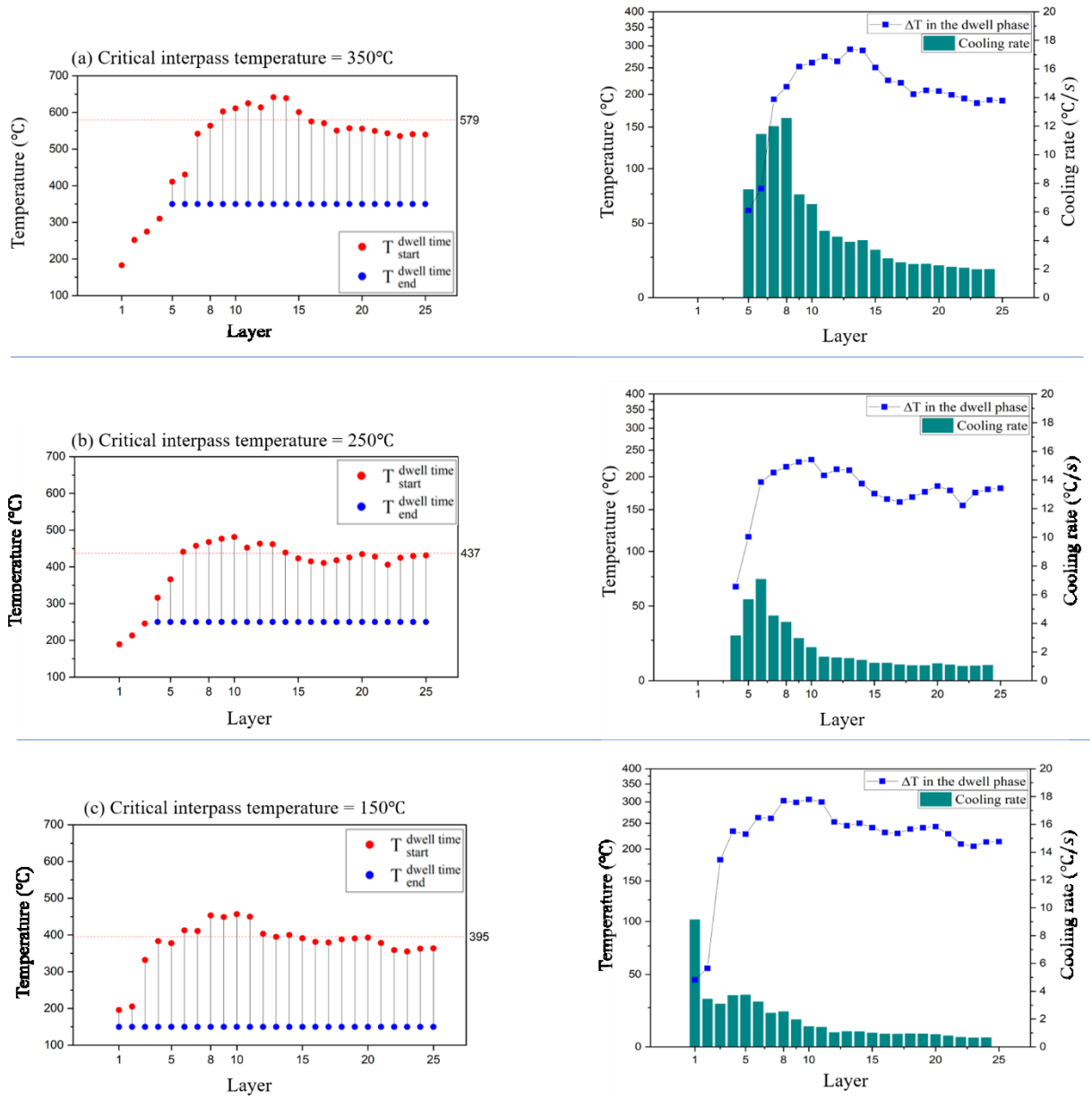

Figure 49. The interpass temperature and cooling rate in the Critical Interpass Temperature strategy.

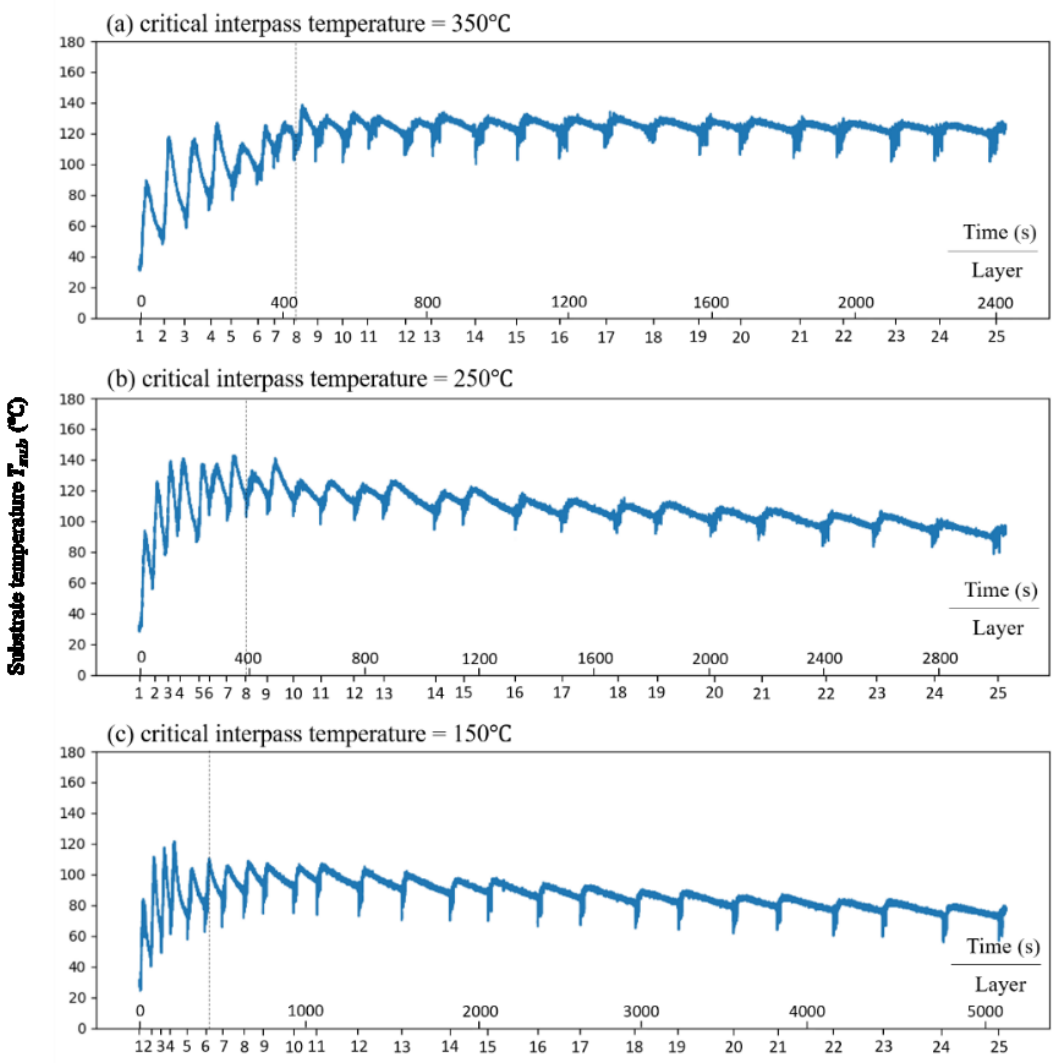

Figure 50. The substrate temperature in the Critical Interpass Temperature strategy.

Based on the temperature information collected from both strategies, an enigmatic layer exists as an interface separating the wall's geometrical properties and thermal state into unstable and stable phases. This layer is usually the 8th layer in this study. It is necessary to find the relationship between the thermal state and geometrical properties in order to efficiently control the geometrical properties of the first seven layers. To find the relationship, Response Surface Method (RSM) analysis was applied by using Minitab (USA). In RSM, T_{dt}^{start}, T_{dt}^{end}, ΔT, and cooling rate are the factors. layer height, width, and height-to-width ratio are responses. A total of 42 sets of data were collected from the first seven layers of all six walls. The raw data used in the RSM analysis is listed in Table 20.

The two-way interaction analysis results with P-values (confidential interval = 95%) and R-Sq are listed in Table 18. The R-Sq values on the three responses are 88.86%, 92.31%, and 84.84%, meaning the model fits well to the data. A small P-Value indicates a strong correlation between the factor and response. Because the confidential interval is set to 95% in this study, the P-Value < 0.05 is considered a small P-Value. In Table 18, the small P-Values are highlighted with a green background. The small P-Values for three responses appear on the term "Cooling rate" and the "interaction of T_{dt}^{start} and Cooling rate". This demonstrates the cooling rate and interaction of T_{dt}^{start} and Cooling rate have a strong influence on the geometrical properties. The function of three geometrical properties and cooling rate and the interaction of T_{dt}^{start} and Cooling rate can be found by building three linear regression models on three properties, as shown in Eq (17), Eq (18), and Eq (19). These regression models are helpful for predicting the wall's geometrical properties once T_{dt}^{start} and Cooling rate are given. The contour plots are also provided in Figure 51 for conveniently checking T_{dt}^{start} and cooling rate for desired geometrical properties.

To further evaluate the accuracy of the regression model, the term Mean Absolute Error (MAE) is used. In statistics, MAE measures errors between paired observations expressing the same phenomenon. MAE is calculated according to Eq (17):

$$\mathrm{MAE} = \frac{\sum_{i=1}^{n} \left| y_i^{actual} - y_i^{predicted} \right|}{n} \tag{16}$$

Where n is the number of data, y_i^{actual} is the actual data collected, and $y_i^{predicted}$ is the predicted data calculated via the linear regression model Eq (17), Eq (18), and Eq (19). The MAE results for wall height, width, and height-to-width are in small values of 15.02%, 15.94%, and 7.68%, respectively. This means the predicted result could fall within $\pm$15.02%, $\pm$15.94%, and $\pm$ 7.68% of the actual value. It can be concluded that the linear regression models for predicting the first seven layers' height, width, and height-to-width ratio are satisfactory.

Table 18. The P-Value (confidential interval = 95%) and R-sq of the RSM analysis on the layer 1 to layer 7.

Term	Layer height	Layer width	Height-to-width ratio
T_{dt}^{start}	0.656	0.117	0.551
T_{dt}^{end}	0.853	0.259	0.800
ΔT	0.860	0.203	0.743
Cooling rate	0.019	0.006	0.002
$T_{dt}^{start} * T_{dt}^{end}$	0.054	0.069	0.064
$T_{dt}^{start} * \Delta T$	0.073	0.081	0.062
T_{dt}^{start}*Cooling rate	0.001	0.046	0.005
$T_{dt}^{end} * \Delta T$	0.875	0.570	0.584
T_{dt}^{end}*Cooling rate	0.745	0.072	0.214
R-sq	88.86%	92.31%	84.84%
MAE	15.02%	15.94%	7.68%

$$\text{Layer height (layer 1-7)} = 6.206 + 1.318 \cdot \text{Cooling rate} - 0.00486 \cdot T_{dt}^{start} \cdot \text{Cooling rate} \quad (17)$$

$$\text{Layer width (layer 1-7)} = 1.298 - 1.389 \cdot \text{Cooling rate} + 0.00259 \cdot T_{dt}^{start} \cdot \text{Cooling rate} \quad (18)$$

$$\text{Height to width ratio (layer 1-7)} = 1.706 + 0.3675 \cdot \text{Cooling rate} - 0.000915 \cdot T_{dt}^{start} \cdot \text{Cooling rate} \quad (19)$$

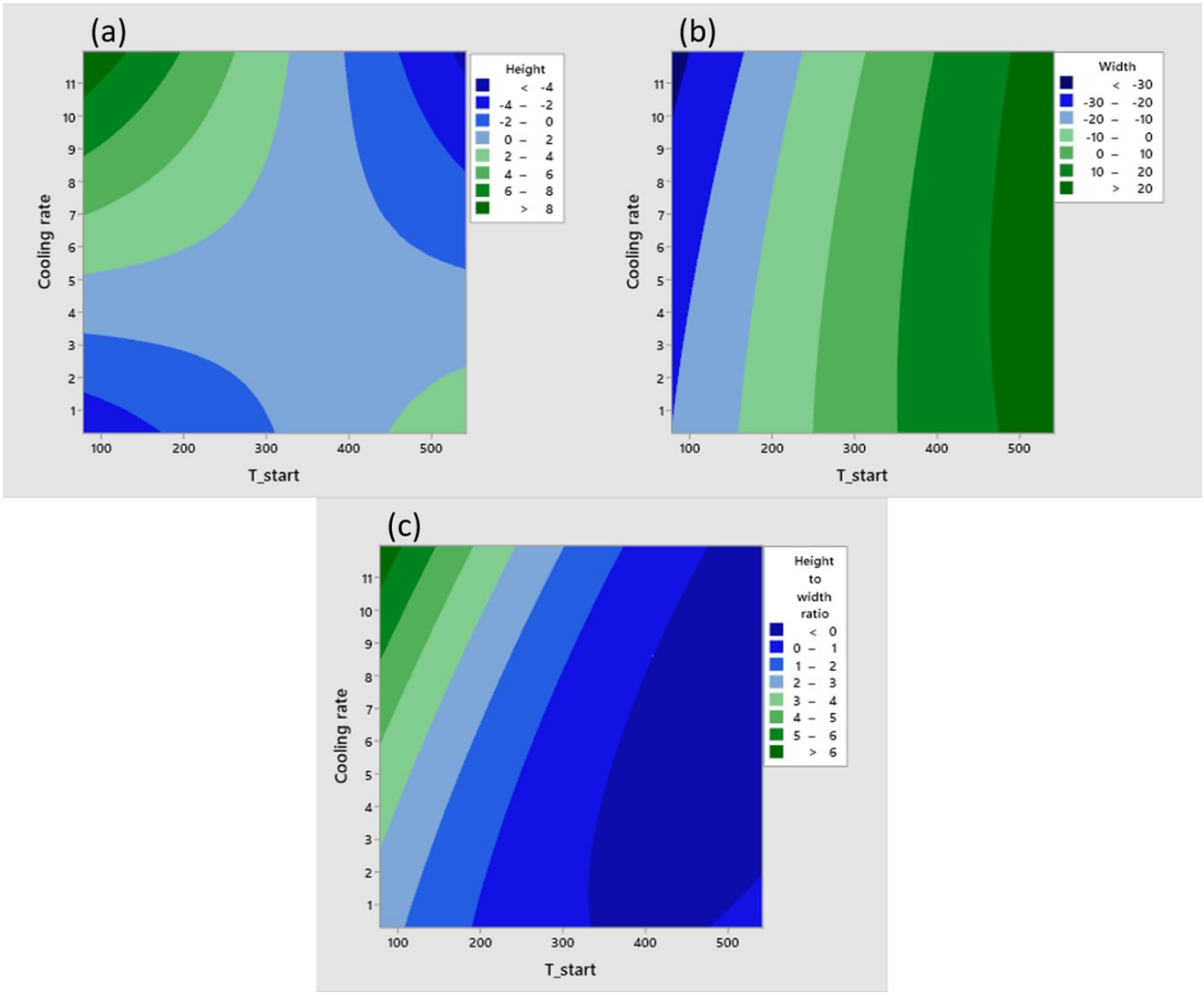

Figure 51. The contour plot of the effect of T_{dt}^{start} and cooling rate on (a) layer height, (b) layer width, and (c) layer height-to-width ratio.

The RSM analysis was also applied to the rest of the layers (layer 8 to layer 25) of each wall printed by the two strategies. The result is shown in Table 19. Contrasting to the result from layer 1 to layer 7, in the RSM result from layer 8 to layer 25, only the cooling rate has a value < 0.05 on the responses "layer width" and "height-to-width ratio", which is highlighted with a green background in Table 19. This result means the cooling rate significantly influences the layer width and height-to-width ratio. For layer height, none of the factors presents a strong effect. This indicates that the layer height of layers 8 to layer 25 is not susceptible to the factors in the scope of this study. The linear regression models to predict layer height, width, and height-to-width ratio were also built, as shown in Eq (20), Eq (21), and Eq (22). The MAE of all three responses is 28.18%, 17.14%,

and 2.23%, respectively. The contour plots are also provided in Figure 51 for convenient checking of T_{dt}^{start} and cooling rate for desired geometrical properties of the layer between 8 to 25.

Table 19. The P-Value (confidential interval = 95%) and R-Sq of the RSM analysis on the layer 8 to layer 25.

Term	Layer height	Layer width	Height-to-width ratio
T_{dt}^{start}	0.499	0.380	0.222
T_{dt}^{end}	0.494	0.567	0.387
ΔT	0.381	0.421	0.417
Cooling rate	0.973	0.011	0.023
T_{dt}^{start}*T_{dt}^{end}	0.873	0.673	0.508
T_{dt}^{start}*ΔT	0.763	0.723	0.447
T_{dt}^{start}*Cooling rate	0.938	0.944	0.117
T_{dt}^{end}*ΔT	0.841	0.736	0.847
T_{dt}^{end}*Cooling rate	0.819	0.982	0.689
R-sq	42.66%	74.29%	65.00%
MAE	28.18%	17.14%	2.23%

$$\begin{aligned}\text{Layer height (layer 8-25)} = {} & 1.253 + 0.308\cdot T_{dt}^{start} - 0.631*T_{dt}^{end} \\ & + 0.006\cdot\Delta T + 0.009\cdot \text{Cooling rate} \\ & - 0.00042\cdot T_{dt}^{start}\cdot T_{dt}^{end} + 0.002\cdot T_{dt}^{start}\cdot\Delta T \\ & + 0.045\cdot T_{dt}^{start}\cdot \text{Cooling rate} \\ & + 0.000087\cdot T_{dt}^{end}\cdot\Delta T - 0.00071\cdot T_{dt}^{end}\cdot \text{Cooling rate}\end{aligned} \quad (20)$$

$$\text{Layer width (layer 8-25)} = 9.084 + 1.62\cdot \text{Cooling rate} \quad (21)$$

$$\text{Height to width ratio (layer 8-25)} = 0.124 - 0.0296\cdot \text{Cooling rate} \quad (22)$$

Table 20. The database of the first 7 layers.

T_{dt}^{start} (°C)	T_{dt}^{end} (°C)	ΔT (°C)	Cooling rate (°C/s)	Layer height (mm)	Layer width (mm)	Height-to-width ratio
81.4	64.3	17.1	0.29	4.04	4.1	1.09
126.8	108.2	18.6	0.31	1.56	5.8	0.30
223.1	170	53.1	0.88	0.94	7.76	0.13
340.6	260.3	80.3	1.34	0.67	8.98	0.08
327	256.2	60.8	1.01	0.41	9.2	0.03
340	287	53	0.88	1.26	7.85	0.27
378.2	300.9	77.3	1.29	0.61	7.99	0.20
78.3	57	21.3	0.35	3.93	3.86	1.13
131	85.9	45.1	0.75	1.44	5.26	0.29
235.5	119.9	115.6	1.93	1.34	6.91	0.17
321.5	233.9	87.6	1.46	0.5	8.24	0.10
390	254.9	135.1	2.25	0.37	8.39	0.01
443	310.2	132.8	2.21	1.53	9.2	0.22
393.6	240.4	153.2	2.55	0.85	9.02	0.11
80	49.6	30.4	0.51	4.28	4.1	1.03
134.4	67.7	66.7	1.11	1.72	6	0.27
216.2	101.4	114.8	1.91	0.85	7.8	0.13
276.1	162.5	113.6	1.89	0.49	8.32	0.08
327.3	173.3	154	2.57	1.62	8.22	0.07
398.6	199.4	199.2	3.32	0.01	9.2	0.12
376.1	194.7	181.4	3.02	1.85	10.24	0.05
182.7	350	-	-	4.28	3.9	1.16
241.6	350	-	-	1.72	5.87	0.34
264.5	350	-	-	0.85	7.05	0.10
300	350	-	-	0.5	8.28	0.08
410.5	350	60.5	7.56	0.49	9.9	0.05
430.1	350	80.1	11.44	1.62	9.97	0.16
541.7	350	191.7	11.98	0.01	10.92	0.16
189.2	250		-	4.06	3.96	1.06
213.25	250	-	-	1.61	5.6	0.31
245.7	250	-	-	1.19	7.1	0.15
316.15	250	66.15	3.15	0.51	8.21	0.05
366.15	250	116.15	5.67	1.34	9.2	0.13
441.15	250	191.15	7.08	0.65	9.25	0.06
457.25	250	207.25	4.53	2.12	8.16	0.28
184.7	150	34.7	4.34	4.24	3.87	1.18
205.1	150	55.1	3.44	1.62	5.75	0.31
332	150	182	3.08	0.99	7.09	0.15
383.4	150	233.4	3.7	0.64	8.22	0.08
377.8	150	227.8	3.73	0.6	9.19	0.03
412.2	150	262.2	3.24	1.92	9.25	0.24
410.6	150	260.6	2.42	1.57	8.12	0.20

6.3.3 The Analysis of Mechanical Properties

To assess the mechanical properties, tensile testing was carried out on the specimens cut from the printed walls. For each wall, the tensile specimens were cut from the horizontal direction (printing direction) and the vertical direction (building direction) by using a wire CNC machine. The cutting layout is shown in Figure 52 (a). The dimension of the tensile specimen used in this study is illustrated in Figure 52 (b). The dimension of the specimen does not follow the ASTM E8 standard since the limitation of the size of the wall. During the test, the specimen was clamped on the Instron (USA) 5966 universal tensile machine with a constant extension rate of 0.02 mm/s [91] until the specimen broke.

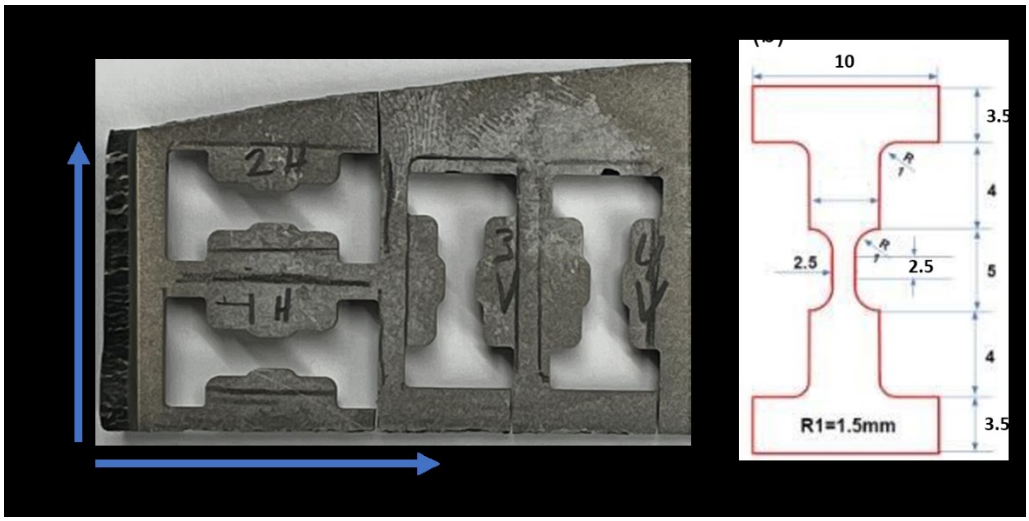

Figure 52. (a) The cutting layout. (b) The dimension of the tensile specimen (all dimensions are in mm).

Figure 53 shows the strain-stress curve of horizontal and vertical specimens cut off from the walls made by Critical Dwell Time and Critical interpass temperature strategies, respectively. The shape of these curves can be observed in Figure 53 (a) and (b). Unlike the typical tensile test strain-stress curve from the traditional 7075 T6 aluminum alloy sample which has a pronounced elastic stage and obvious yield point, as shown in Figure 54 (a), the curves of 7075NT aluminum alloy are smooth without apparent elastic stage and yield point. This result may be because of the existence of NbC (Niobium Carbide) ceramic particles in 7075NT aluminum alloy. Özdemirler et al. [92] added NbC ceramic particles into steel samples at a ratio of 0.2% to 2% in terms of weight. The testing results from these samples are shown in Figure 54 (b). Surprisingly, all curves lose the

shape of traditional steel strain-stress curves after adding NbC ceramic particles. The distinct elastic stage and yield point disappear. Instead, the curves show a smooth morphology. Özdemirler et al. [92] indicate that these NbC-involved steel samples have the elastic stage and yield point. However, their yield stress is too small to be visually observed. This small elastic region forms because the NbC ceramic particles form the coarse NbC precipitates on the grain boundary, which leads to the lower elasticity between grains and causes low yield stress. The NbC ceramic particle may perform a similar function on 7075NT aluminum alloy. The mechanism needs to be investigated in the feature.

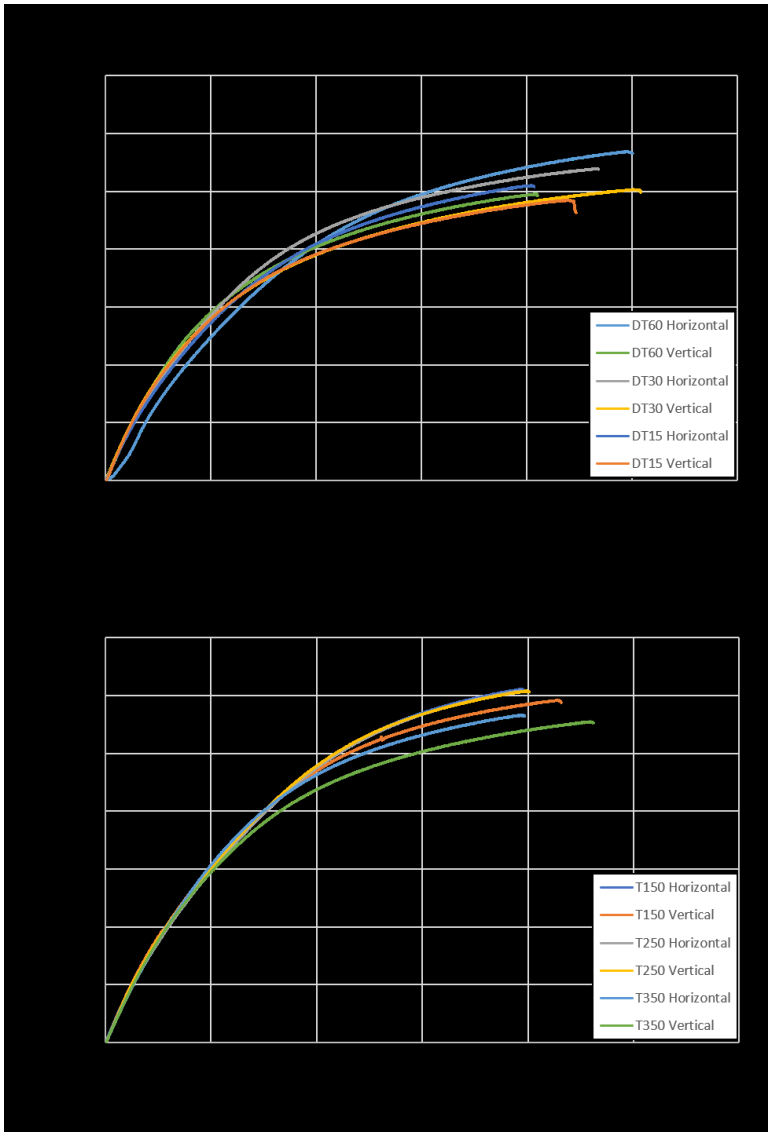

Figure 53. The strain-stress curve of horizontal and vertical specimens in (a) Critical Dwell Time and (b) Critical interpass temperature strategies.

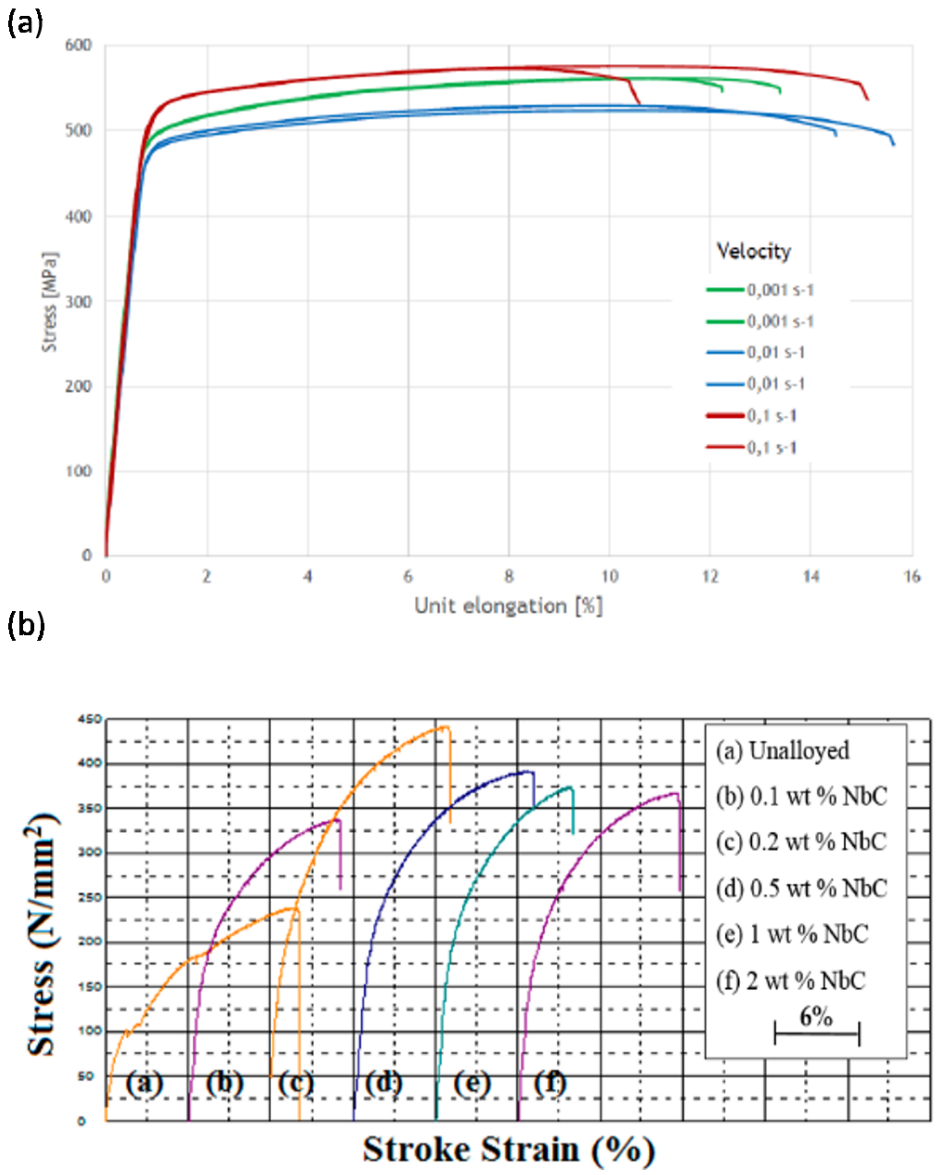

Figure 54. The stress-strain curve of (a) 7075 T6 aluminum alloy [91] and (b) NbC added steel [92].

The mechanical properties, including Young's modulus, yield stress, yield strain, ultimate tensile strength (UTS), and break strain are extracted from Figure 53 and listed in Table 22. The 0.2% offset strain method and Extension-Under-Load (EUL) method are prescribed in ASTM E8 [93] and ASTM B557 [94] standards. In this chapter, the 0.2% offset strain method was used to find the yield point. The Extension-Under-Load (EUL) method was also applied as shown in Appendix I. The mechanical properties are separated into two categories: Young's modulus, yield stress, and yield strain were analyzed together to investigate the material's elasticity. Other

properties, including ultimate tensile strength (UTS) and break strain, were analyzed together to investigate the material's ductility. Regardless of the heat management strategies and specimen cutting direction, the average Young's modulus is 8556.52 N/mm^2, the average yield stress is 123.36 MPa, and the average yield strain is 0.05. Compared to other 7075 aluminum alloy tensile testing results where the yield stress and yield strain are tested around 500 MPa and 0.01 [91,95], this study shows lower yield stress but higher yield strain. Young's modulus is a mechanical property that measures a solid material's tensile when force is applied lengthwise. It quantifies the elastic region's relationship between tensile stress and strain. Young's modulus can be calculated from yield stress and yield strain via Eq (23) if the tensile test is performed at zero stress and strain. Based on yield stress and yield strain in other studies [91,95], the Young's modulus can be calculated to be equal to around 50000.00 N/mm^2 for traditional 7075-T6 aluminum alloy. This Young's modulus is much greater than the 8556.52 N/mm^2 measured in this study. This result indicates that the 7075NT aluminum alloy additively manufactured by the WAAM process has less elasticity than conventional 7075-T6 aluminum alloy. The average UTS in this study is 553.30 MPa which is close to 276 MPa in traditional 7075 aluminum alloy and 518 MPa in 7075-T6 aluminum [91]. However, the breaking strain of 0.22 is higher than 0.11 in traditional 7075 aluminum [91][95], indicating that the 7075NT aluminum alloy additively manufactured by the WAAM process has better ductility than traditional 7075 aluminum alloy. The mechanical properties of 7075NT aluminum, traditional 7075 aluminum alloy and 7075-T6 aluminum alloy mentioned above are summarized in Table 21. From the result, it can be concluded that 7075NT aluminum alloy in the WAAM process presents less elasticity but better ductility.

$$\text{Young's modulus} = \frac{\sigma_{yield}}{\varepsilon_{yield}} \tag{23}$$

It can also be observed from Table 22 that the mechanical properties vary depending on the heat management strategies and the specimen's cutting direction. Young's modulus, yield strength, and UTS are extracted from the table and plotted as charts in Figure 55 (a), (b), and (c). In both two heat management strategies, both Young's modulus and UTS increase when the dwell time increases and the interpass temperature decreases. Because the increase of the critical dwell time or the decrease of the critical interpass temperature reduces the heat accumulation in the manufactured part. Therefore, Young's modulus and UTS are inversely related to heat accumulation. An exception is the yield strength tested in this study, which does not show a strong

relationship to heat accumulation. In the specimen cutting direction aspect, Young's modulus, yield strength, and UTS of the specimen cut off from the horizontal direction (printing direction) are all higher than the samples cut from the vertical direction (building direction). This result shows an anisotropy between the horizontal and vertical directions. The anisotropic mechanical properties commonly exist not only in metal AM processes but in almost all AM processes [8–10,18,24,44]. The anisotropy can be attributed to the cross-sectional and interpass layer weakening by pores and crack initiation by stress concentration at the pores [96].

Table 21. The comparison of mechanical properties between 7075NT and traditional 7075 aluminum alloy.

	7075NT aluminum alloy	Traditional 7075 aluminum alloy	7075-T6 aluminum alloy
Yield stress (MPa)	123.36	145	500
Yield strain	0.05	-	0.01
Young's modulus (N/mm^2)	8556.52	-	50000.00
UTS (MPa)	553.30	276	518.00
Break strain	0.22	0.10	0.11

The interpass temperature in WAAM process of aluminum alloy has great effect on porosity formation which saps the mechanical properties of the printed parts [62]. Therefore, to investigate the effect of two heat management strategies on porosity, the porosity of the tensile specimens was tested in this study. The horizontal and vertical specimens used in porosity testing were cut from the 2-H and 4-V positions of the printed walls, shown in Figure 53 (a), and the dimension of the specimens is shown in Figure 53 (b).

The porosity (ϕ) is defined as a fraction of the volume of voids (V_{void}) over the total volume (V_{actual}), as expressed in Eq (24).

$$\phi = \frac{V_{void}}{V_{actual}} \tag{24}$$

Table 22. The detail of tensile testing result (Yield strain offset = 0.2%).

	DT15-H	DT15-V	DT30-H	DT30-V	DT60-H	DT60-V	T350-H	T350-V	T250-H	T250-V	T150-H	T150-V
Young's modulus (N/mm^2)	8556.90	8252.60	8540.20	8483.40	8794.00	8780.50	8240.30	8172.80	8664.10	8501.60	8877.40	8814.40
Yield Strength (MPa)	128.83	123.40	125.97	121.94	126.89	125.00	128.06	115.19	129.00	116.43	125.67	113.97
Yield Strain	0.018	0.016	0.017	0.016	0.023	0.017	0.017	0.015	0.017	0.147	0.159	0.141
Ultimate tensile Strength (MPa)	509.93	484.57	539.09	502.94	568.55	495.50	565.71	554.59	608.36	607.66	610.94	591.72
Break Strain	0.20	0.22	0.23	0.25	0.25	0.20	0.20	0.23	0.20	0.20	0.20	0.21

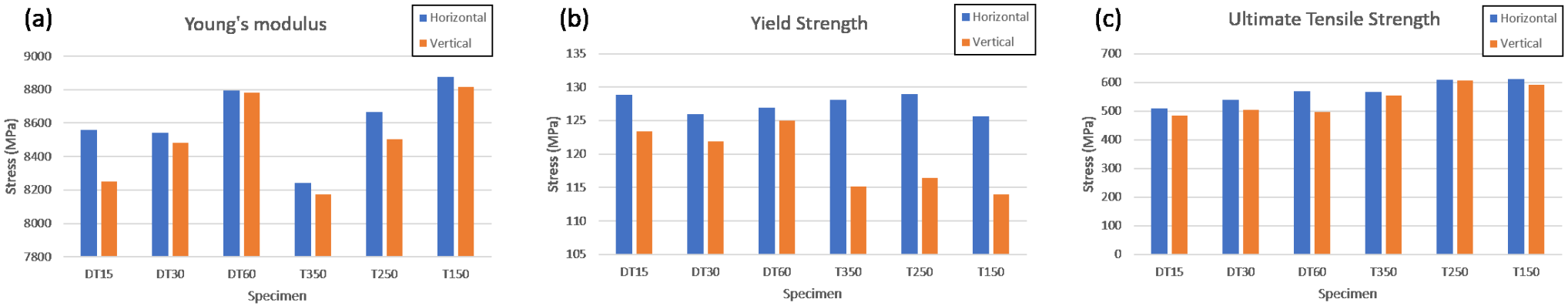

Figure 55. Comparison of (a) Young's modulus, (b) yield strength (0.5% offset method), and (c) ultimate tensile strength between specimens.

$$V_{actual} = \frac{m}{\rho_{7075NT}} \tag{25}$$

$$V_{void} = |V_{bulk} - V_{actual}| \tag{26}$$

Where V_{actual} is the calculated by using the mass (m) of the specimen divided by the density ($\rho_{7075NT} = 0.00271\ g/mm^2$) of the 7075NT aluminum alloy, as expressed in Eq (25). The density of 7075NT aluminum alloy wire was tested by dividing a section of wire with this section's volume, as expressed in Eq (26), where L_{wire} =50mm is the length of the wire section, d_{wire}=1.2mm is the diameter of the wire. This density test was repeated 5 times and the average result of these 5 repetitions was selected as the density of 7075NT aluminum alloy.. The details of the density test data are listed in Table *23*. In Eq (24), V_{void} is the difference between the full-filled specimen volume (V_{bulk}) and the actual volume of the specimen (V_{actual}), as expressed in Eq (26). V_{bulk} is calculated by the product of the area (S) and the thickness ($d = 2\ mm$) of the specimen. Area (s) is calculated by counting the pixel of the picture of the front view of the specimen by using ImageJ image processing software, and converting the counted pixels to area in mm^2 with the coefficient 1 pixel = 0.025 mm^2, as shown in Figure *56*. The calculated V_{actual}, V_{bulk}, V_{void} and ϕ are listed in Table 24.

$$\rho_{7075NT} = \frac{m}{V} = \frac{m}{L_{wire}\pi(\frac{d_{wire}}{2})^2} \tag{27}$$

Table 23.The detail of the test of 7075NT aluminum alloy density.

trial	1	2	3	4	5
Density (g/mm^2)	0.0027098	0.0027071	0.0027076	0.0027091	0.0027228
Average density (g/mm^2)			0.002711		

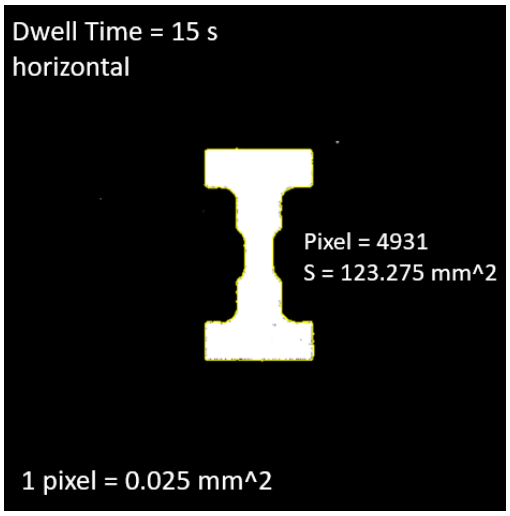

Figure 56. The illustration of the pixel counting process in ImageJ.

The porosity of multiple specimens was tested, and the results were plotted in chart Figure 57. The chart shows that the porosity of the specimens ranges from 1.21% to 1.53%. The lowest porosity was found at a dwell time of 30 seconds, and the highest porosity was found at a dwell time of 15 seconds for vertical specimens. The porosity of horizontal and vertical specimens were similar at each level, with the largest difference being 0.29% at an interpass temperature of 350℃.This indicates there is no obvious isotropy on porosity. However, when analyzing only the porosity of the horizontal specimens, it was found that the porosity increases as the increase of the dwell time and the decrease of the interpass temperature. As analyzed before, the increase of the dwell time and the decrease of the interpass temperature means there is less heat accumulation in the part. Thus, for horizontal specimens, the porosity has a clear trend with the change of the heat accumulation of the part. A possible explanation for this result may be related to the pores existing between two layers. Derekar et.al [62] state in his research that there is huge number of pores accumulated between two adjacent layers found by CT scanning result of the WAAM-made aluminum alloy. In Chapter 6.3.2, it has been claimed that more heat accumulation brings flatter layer. Therefore, the part printed with higher heat accumulation has more layers in a unit of volume and leads to more pores. These pores may cause greater porosity. Moreover, as correlating the porosity with the UTS of the horizontal specimens, it can be found that the UTS is inverse proportional to the porosity. This suggests the higher porosity may be a factor that deteriorates the

UTS along the horizontal printing direction of the WAAM-made part. Compared to the horizontal specimens, the porosity of the vertical specimens does not show a distinct pattern.

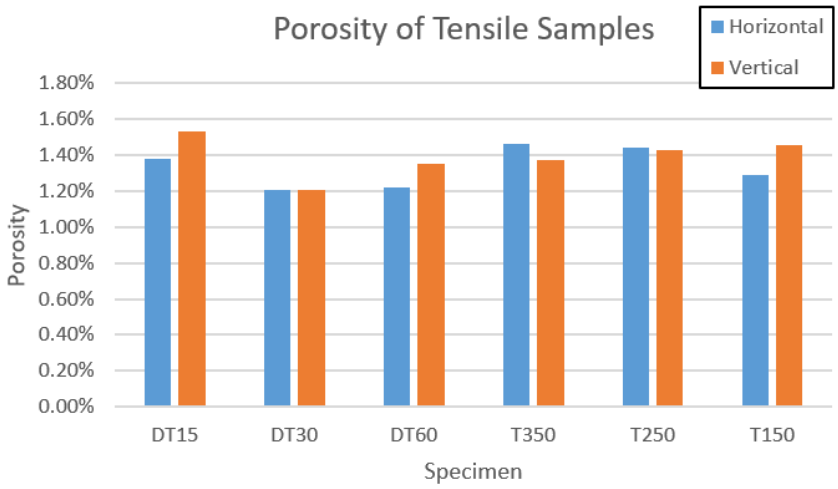

Figure 57. The porosity testing result.

Table 24. The detail of the calculated parameters of the porosity test.

	DT15-H	DT15-V	DT30-H	DT30-V	DT60-H	DT60-V	T350-H	T350-V	T250-H	T250-V	T150-H	T150-V
S (mm^2)	123.475	123.475	123.075	123.075	123.275	123.250	123.575	123.650	123.175	123.350	123.175	123.200
V_{bulk} (mm^3)	246.950	246.950	246.150	246.150	246.550	246.500	247.150	247.300	246.350	246.700	246.350	246.400
Actual mass (g)	0.660	0.659	0.659	0.659	0.660	0.659	0.660	0.661	0.658	0.659	0.659	0.658
V_{actual} (mm^3)	243.542	243.173	243.173	243.173	243.542	243.173	243.542	243.911	242.804	243.173	243.173	242.804
V_{void} (mm^3)	3.408	3.777	2.977	2.977	3.008	3.327	3.608	3.389	3.546	3.527	3.177	3.596
Porosity	1.38%	1.53%	1.21%	1.21%	1.22%	1.35%	1.46%	1.37%	1.44%	1.43%	1.29%	1.46%

6.1 Chapter Conclusion

In this chapter, two heat management strategies were applied to fabricating the 7075NT aluminum alloy wall in WAAM. A total of 6 walls were printed. None of them shows fatal geometrical defects meaning 7075NT aluminum alloy is compatible with the WAAM process. The geometrical, thermal state, and mechanical properties were analyzed, and their relationship to the two strategies was assessed.

For geometrical properties, the following conclusions can be summarized:

- With the increase of dwell time or the decrease of interpass temperature, the shape of the layer tends to be more arch-shaped, and the geometry of the layer stabilizes more quickly
- The 8^{th} layer is an interface that divides the stable and unstable geometrical properties of the layers. Before the 8^{th} layer, layer height, width, and height-to-width ratio have a more significant mean standard deviation, indicating an inconsistent geometry. However, after the 8^{th} layer, the geometrical properties of layers are more consistent.

From the analysis of the thermal state during the process, the following conclusions are summarized:

- In both strategies, interpass temperature and cooling rate increase drastically before the 8^{th} layer and gradually converge to a stable phase from the 8^{th} to the 25^{th} layer.
- According to the RSM analysis result, the interpass temperature and the cooling rate significantly impact the first seven layers' geometrical properties. However, from layer 8 to layer 25, only cooling rate significantly influences the layer width and height-to-width ratio and none of the factors significantly affects the layer height from the eighth to the twenty-fifth layer.

For geometrical properties, the below features can be found:

- The stress-strain curves from tensile test show that 7075NT aluminum alloy has less elasticity but better ductility compared to the traditional 7075 aluminum alloy.

- For the WAAM-made 7075NT aluminum part, the range of yield strength is 115.19 to 129.00 MPa, and the range of UTS is from 509.93 to 610.94 MPa, depending on the heat management strategies.
- The mechanical properties show the samples cut from the horizontal direction have greater mechanical properties than the samples cut from the vertical direction.
- The porosity of specimens ranges from 1.21% to 1.53%. The porosity of the horizontal specimens shows an obvious relationship with the heat accumulation and UTS.

7. Conclusions and Feature Works

7.1 Conclusion

A new process of net-shape fabricating large-size 7075NT aluminum alloy industrial parts by utilizing the WAAM process, and the quality control of the parts has been investigated in this study. To reach this goal, three subtopics: “WAAM In-situ Multi-sensor Monitoring System Setup,” “Process Parameters Exploration,” and “Heat Management and Quality Control” were presented in sequence.

An in-house in-situ multi-sensor WAAM system was first creatively built in this study by integrating a profiler meter, thermocouple, and IR camera together and embedding them into Robot Operating System (ROS). This multi-sensor WAAM system has the ability to conduct the WAAM process and in-situ monitor and record the temperature, layer contour geometry, and energy input during the process. These collected processing data are the foundation of later experiments and analyses.

Processing temperature is a vital information that is necessary to be collected to improve the process and control the quality. However, there is no published research and dataset indicating the emissivity of this new material 7075NT aluminum alloy and its implement in the WAAM process. To obtain temperature data collected from the IR camera accurately, this study calibrates the emissivity of WAAM-made 7075NT aluminum alloy novelly. The calibrated emissivity is between 0.733 to 0.955. Additionally, the result indicates that the surface texture and surface conditions significantly influence emissivity. The regression models were established for convenient off-line prediction and analysis, or the on-line temperature measurement and recording.

The essential process parameters that affect the geometrical property were screened out by designing and performing a full-factorial screening experiment. Based on the ANOVA analysis, three parameters: Torch Travel Speed (TTS), Wire Feed Speed (WFS), and interpass temperature have a significant influence on the wall's geometrical properties. By observing the layer's appearance and calculating the process's energy consumption, a good printed bead was found with a parameter set of WFS = 180 in/min, TTS = 14 in/min, and CTDW = 15 mm. In this parameter set, the energy consumption is 3586 J/mm·g, and the heat input (HI) is 122.65 J/mm.

Two heat management strategies in controlling the quality of parts were investigated. The geometrical, thermal state, and mechanical properties were analyzed, and their relationship to the two strategies was built. For geometrical properties, it can be seen that with the increase of dwell time or the decrease of interpass temperature, the shape of the layer tends to be more arch-shaped, and the shape of the layer stabilizes more quickly. The 8^{th} layer is an interface that divides the stable and unstable geometrical properties. Based on the RSM analysis result, the interpass temperature just after the deposition of the new layer and the cooling rate of the interpass temperature significantly impact the first seven layer's geometrical properties. Linear regression models are given for conveniently predicting the geometry of the first seven layers and the rest of the layers, respectively. The mechanical properties were tested. The yield strength range is from 115.19 to 129.00 MPa, and the range of UTS is from 509.93 to 610.94 MPa. Moreover, the mechanical properties show a pronounced anisotropy along the printing and building directions. The porosity of specimens ranges from 1.21% to 1.53%. The porosity of the horizontal specimens shows an obvious relationship with the heat accumulation and UTS.

The analysis of the walls printed in two applied strategies has been conducted. The results show there is no significant difference in mechanical properties. However, the walls printed by Critical Interpass Temperature strategy have a quicker convergence and better stability of the part's geometrical property than the walls printed by the Critical Dwell Time strategy. Additional, during the process of the WAAM with Critical Interpass Temperature strategy, the interpass temperature is the only factor need to control, rather than the multiple factors, such as surface area, heat conduction, convection, and radiation, in Critical Dwell Time strategy. This provides much more convenience and possibilities to print parts with more complicated shapes. Therefore, this study proposes to do more research and exploration on the Critical Interpass Temperature strategy in order to further optimize part quality.

7.2 Future Work

The results presented in this study give a new possibility to precisely measure, predict, and control the quality of the CMT-based WAAM process for fabricating large 7075NT aluminum alloy parts in the industry. Moreover, the in-situ multi-sensor monitoring system and the analysis methods involved in this study are compatible with other metal materials used in WAAM. However, to

optimize the WAAM process and the quality of its fabricated part. The following future research is recommended.

- More Non-Destructive Testing (NDT) sensors need to be integrated into the current in-situ multi-sensor WAAM system for providing precise material identification and trace analysis of important elements such as nitrogen in steel and phosphorus in aluminum.
- The advanced feedback system between the data collected via the in-situ monitoring system and the process parameters needs to be established to precisely control the layer's geometry and mechanical quality.
- A challenge in this study has not been solved is the unstable arc on and off occurs at the beginning and the end of layer deposition, causing undesired slump and bump of the layer. This issue is common in welding. However, this problem is magnified in parts made by WAAM when defects accumulate at each layer and are reflected in the poor geometry of the part.
- From the mechanical properties testing results, the yield strength has a significant anisotropy on the specimens printed under the Critical Interpass Temperature strategy. This anisotropy may occur because of pores between the interface of each layer. Further CT scanning or microstructure examination is recommended.

Bibliography

[1] ISO 52900:2015, International Standard ISO 52900:2015 Additiva Manufacturing, 2015.

[2] O. Diegel, Additive Manufacturing, in: Compr. Mater. Process., Elsevier, 2014: pp. 3–18. https://doi.org/10.1016/B978-0-08-096532-1.01000-1.

[3] Z. Lanc, B. Štrbac, M. Zeljković, A. Živković, M. Hadžistević, Munz, O. J. Photo-Glyph Recording. US Patent 1956, 2, 775,758., 1956. https://doi.org/10.17222/mit.2017.152.

[4] Swainson, Swainson, W. K. Method, Medium and Apparatus for Producing Three-Dimensional Figure Product. US Patent 1977, 4, 041,476., 1977. https://www.unhcr.org/frequently-asked-questions.html.

[5] H. Kodama, Automatic method for fabricating a three-dimensional plastic model with photo-hardening polymer, Rev. Sci. Instrum. 52 (1981) 1770–1773. https://doi.org/10.1063/1.1136492.

[6] C.W. Hull, Apparatus for production of three-dimensional objects by stereolithography, US Patent 1985 4,575,330, 1985. https://doi.org/10.1088/1757-899X/716/1/012012.

[7] T.T. Wohlers, W. Associates, I. Campbell, R. Huff, O. Diegel, J. Kowen, Wohlers Report 2019: 3D Printing and Additive Manufacturing State of the Industry, Wohlers Associates, 2019. https://books.google.ca/books?id=jy4KxQEACAAJ.

[8] K. Treutler, V. Wesling, The Current State of Research of Wire Arc Additive Manufacturing (WAAM): A Review, Appl. Sci. 11 (2021) 8619. https://doi.org/10.3390/app11188619.

[9] D. Jafari, T.H.J. Vaneker, I. Gibson, Wire and arc additive manufacturing: Opportunities and challenges to control the quality and accuracy of manufactured parts, Mater. Des. (2021) 109471. https://doi.org/10.1016/j.matdes.2021.109471.

[10] T.A. Rodrigues, V. Duarte, R.M. Miranda, T.G. Santos, J.P. Oliveira, Current Status and Perspectives on Wire and Arc Additive Manufacturing (WAAM), Materials (Basel). 12 (2019) 1121. https://doi.org/10.3390/ma12071121.

[11] M. Leary, Powder bed fusion, in: M. Leary (Ed.), Des. Addit. Manuf., Elsevier, 2020: pp. 295–319. https://doi.org/10.1016/B978-0-12-816721-2.00011-7.

[12] A.A. Mohammed, M.S. Algahtani, M.Z. Ahmad, J. Ahmad, S. Kotta, 3D Printing in medicine: Technology overview and drug delivery applications, Ann. 3D Print. Med. 4 (2021) 100037. https://doi.org/10.1016/j.stlm.2021.100037.

[13] B. Redwood, F. Schöffer, B. Garret, The 3D Printing Handbook, 3D Hubs. (2017) 304. https://books.google.com/books/about/The_3D_Printing_Handbook.html?hl=pl&id=R3OvswEACAAJ.

[14] J.F.L.A.W. Foundation, L.E. Company, The Procedure Handbook of Arc Welding, Langara

College, 2013. https://books.google.ca/books?id=irYbuAEACAAJ.

[15] J.L. Prado-Cerqueira, J.L. Diéguez, A.M. Camacho, Preliminary development of a Wire and Arc Additive Manufacturing system (WAAM), Procedia Manuf. 13 (2017) 895–902. https://doi.org/10.1016/j.promfg.2017.09.154.

[16] A. Haelsig, M. Kusch, P. Mayer, New Findings On The Efficiency Of Gas Shielded Arc Welding, Weld. World. 56 (2012) 98–104. https://doi.org/10.1007/BF03321400.

[17] S. Selvi, A. Vishvaksenan, E. Rajasekar, Cold metal transfer (CMT) technology - An overview, Def. Technol. 14 (2018) 28–44. https://doi.org/10.1016/J.DT.2017.08.002.

[18] S. Thapliyal, Challenges associated with the wire arc additive manufacturing (WAAM) of aluminum alloys, Mater. Res. Express. 6 (2019) 0–9. https://doi.org/10.1088/2053-1591/ab4dd4.

[19] W. Carter, C. Masuo, A. Nycz, M. Noakes, D. Vaughan, Thermal process monitoring for wire-arc additive manufacturing using IR cameras, Solid Free. Fabr. 2019 Proc. 30th Annu. Int. Solid Free. Fabr. Symp. - An Addit. Manuf. Conf. SFF 2019. (2019) 1812–1817.

[20] X. Fang, L. Zhang, G. Chen, X. Dang, K. Huang, L. Wang, B. Lu, Correlations between microstructure characteristics and mechanical properties in 5183 aluminium alloy fabricated by wire-arc additive manufacturing with different arc modes, Materials (Basel). 11 (2018). https://doi.org/10.3390/ma11112075.

[21] X. Fang, L. Zhang, H. Li, C. Li, K. Huang, B. Lu, Microstructure Evolution and Mechanical Behavior of 2219 Aluminum Alloys Additively Fabricated by the Cold Metal Transfer Process, Materials (Basel). 11 (2018) 812. https://doi.org/10.3390/ma11050812.

[22] Y. Nie, P. Zhang, X. Wu, G. Li, H. Yan, Z. Yu, Rapid prototyping of 4043 Al-alloy parts by cold metal transfer, Sci. Technol. Weld. Join. (2018). https://doi.org/10.1080/13621718.2018.1438236.

[23] D. Ding, Z. Pan, D. Cuiuri, H. Li, A multi-bead overlapping model for robotic wire and arc additive manufacturing (WAAM), Robot. Comput. Integr. Manuf. 31 (2015) 101–110. https://doi.org/10.1016/j.rcim.2014.08.008.

[24] M. Gierth, P. Henckell, Y. Ali, J. Scholl, J.P. Bergmann, Wire Arc Additive Manufacturing (WAAM) of Aluminum Alloy AlMg5Mn with Energy-Reduced Gas Metal Arc Welding (GMAW), Materials (Basel). 13 (2020) 2671. https://doi.org/10.3390/ma13122671.

[25] M. Köhler, S. Fiebig, J. Hensel, K. Dilger, Wire and Arc Additive Manufacturing of Aluminum Components, Metals (Basel). 9 (2019) 608. https://doi.org/10.3390/met9050608.

[26] G. Li, F. Chen, Y. Han, Y. Liang, Improving Mechanical Properties of PVPPA Welded Joints of 7075 Aluminum Alloy by PWHT, Materials (Basel). 11 (2018) 379. https://doi.org/10.3390/ma11030379.

[27] M. Kang, C. Kim, A Review of Joining Processes for High Strength 7xxx Series Aluminum Alloys, 35 (2017) 79–88.

[28] B. Çevik, Gas tungsten arc welding of 7075 aluminum alloy: microstructure properties, impact strength, and weld defects, Mater. Res. Express. 5 (2018) 066540. https://doi.org/10.1088/2053-1591/aacbbc.

[29] D. Oropeza, D.C. Hofmann, K. Williams, S. Firdosy, P. Bordeenithikasem, M. Sokoluk, M. Liese, J. Liu, X. Li, Welding and additive manufacturing with nanoparticle-enhanced aluminum 7075 wire, J. Alloys Compd. 834 (2020) 154987. https://doi.org/10.1016/j.jallcom.2020.154987.

[30] M. Zuo, M. Sokoluk, C. Cao, J. Yuan, S. Zheng, X. Li, Microstructure Control and Performance Evolution of Aluminum Alloy 7075 by Nano-Treating, Sci. Rep. 9 (2019) 10671. https://doi.org/10.1038/s41598-019-47182-9.

[31] W.-Y. Cai, Y.-B. Wang, G.-Q. Li, Experimental and numerical study on strength of high-strength steel double-V butt-welded joint, J. Constr. Steel Res. 196 (2022) 107397. https://doi.org/https://doi.org/10.1016/j.jcsr.2022.107397.

[32] J.D. Spencer, P.M. Dickens, C.M. Wykes, Rapid prototyping of metal parts by three-dimensional welding, Proc. Inst. Mech. Eng. Part B J. Eng. Manuf. 212 (1998) 175–182. https://doi.org/10.1243/0954405981515590.

[33] M. Chaturvedi, E. Scutelnicu, C.C. Rusu, L.R. Mistodie, D. Mihailescu, S. Arungalai Vendan, Wire arc additive manufacturing: Review on recent findings and challenges in industrial applications and materials characterization, Metals (Basel). 11 (2021). https://doi.org/10.3390/met11060939.

[34] Q. Yang, C. Xia, Y. Deng, X. Li, H. Wang, Microstructure and Mechanical Properties of AlSi7Mg0.6 Aluminum Alloy Fabricated by Wire and Arc Additive Manufacturing Based on Cold Metal Transfer (WAAM-CMT), Materials (Basel). 12 (2019) 2525. https://doi.org/10.3390/ma12162525.

[35] R. Fu, S. Tang, J. Lu, Y. Cui, Z. Li, H. Zhang, T. Xu, Z. Chen, C. Liu, Hot-wire arc additive manufacturing of aluminum alloy with reduced porosity and high deposition rate, Mater. Des. 199 (2021) 109370. https://doi.org/https://doi.org/10.1016/j.matdes.2020.109370.

[36] B.F. Gomes, P.J. Morais, V. Ferreira, M. Pinto, L.H. de Almeida, Wire-arc additive manufacturing of Al-Mg alloy using CMT and PMC technologies, MATEC Web Conf. 233 (2018) 00031. https://doi.org/10.1051/matecconf/201823300031.

[37] G. Ma, G. Zhao, Z. Li, M. Yang, W. Xiao, Optimization strategies for robotic additive and subtractive manufacturing of large and high thin-walled aluminum structures, Int. J. Adv. Manuf. Technol. 101 (2019) 1275–1292. https://doi.org/10.1007/s00170-018-3009-3.

[38] I. Ünsal, M. Hirtler, A. Sviridov, M. Bambach, Material Properties of Features Produced from EN AW 6016 by Wire-Arc Additive Manufacturing, Procedia Manuf. 47 (2020) 1129–

1133. https://doi.org/10.1016/j.promfg.2020.04.131.

[39] Q. Wu, T. Mukherjee, C. Liu, J. Lu, T. DebRoy, Residual stresses and distortion in the patterned printing of titanium and nickel alloys, Addit. Manuf. 29 (2019) 100808. https://doi.org/10.1016/j.addma.2019.100808.

[40] T. Mukherjee, V. Manvatkar, A. De, T. DebRoy, Mitigation of thermal distortion during additive manufacturing, Scr. Mater. 127 (2017) 79–83. https://doi.org/10.1016/j.scriptamat.2016.09.001.

[41] J. Ding, P. Colegrove, J. Mehnen, S. Ganguly, P.M. Sequeira Almeida, F. Wang, S. Williams, Thermo-mechanical analysis of Wire and Arc Additive Layer Manufacturing process on large multi-layer parts, Comput. Mater. Sci. 50 (2011) 3315–3322. https://doi.org/10.1016/j.commatsci.2011.06.023.

[42] J. Gu, J. Ding, S.W. Williams, H. Gu, P. Ma, Y. Zhai, The effect of inter-layer cold working and post-deposition heat treatment on porosity in additively manufactured aluminum alloys, J. Mater. Process. Technol. 230 (2016) 26–34. https://doi.org/10.1016/j.jmatprotec.2015.11.006.

[43] E. Soderstrom, P. Mendez, Humping mechanisms present in high speed welding, Sci. Technol. Weld. Join. 11 (2006) 572–579. https://doi.org/10.1179/174329306X120787.

[44] X. Lu, Y.F. Zhou, X.L. Xing, L.Y. Shao, Q.X. Yang, S.Y. Gao, Open-source wire and arc additive manufacturing system: formability, microstructures, and mechanical properties, Int. J. Adv. Manuf. Technol. 93 (2017) 2145–2154. https://doi.org/10.1007/s00170-017-0636-z.

[45] H. Geng, J. Li, J. Xiong, X. Lin, Optimisation of interpass temperature and heat input for wire and arc additive manufacturing 5A06 aluminium alloy, Sci. Technol. Weld. Join. 22 (2017) 472–483. https://doi.org/10.1080/13621718.2016.1259031.

[46] M. Motta, A.G. Demir, B. Previtali, High-speed imaging and process characterization of coaxial laser metal wire deposition, Addit. Manuf. 22 (2018) 497–507. https://doi.org/https://doi.org/10.1016/j.addma.2018.05.043.

[47] D. Wu, X. Hua, D. Ye, F. Li, Understanding of humping formation and suppression mechanisms using the numerical simulation, Int. J. Heat Mass Transf. 104 (2017) 634–643. https://doi.org/10.1016/j.ijheatmasstransfer.2016.08.110.

[48] A. Gomez Ortega, L. Corona Galvan, F. Deschaux-Beaume, B. Mezrag, S. Rouquette, Effect of process parameters on the quality of aluminium alloy Al5Si deposits in wire and arc additive manufacturing using a cold metal transfer process, Sci. Technol. Weld. Join. 23 (2018) 316–332. https://doi.org/10.1080/13621718.2017.1388995.

[49] X. Xu, J. Ding, S. Ganguly, C. Diao, S. Williams, Oxide accumulation effects on wire + arc layer-by-layer additive manufacture process, J. Mater. Process. Technol. 252 (2018) 739–750. https://doi.org/10.1016/j.jmatprotec.2017.10.030.

[50] X. Bai, H. Zhang, G. Wang, Modeling of the moving induction heating used as secondary heat source in weld-based additive manufacturing, Int. J. Adv. Manuf. Technol. 77 (2015) 717–727. https://doi.org/10.1007/s00170-014-6475-2.

[51] J.H. Ouyang, H. Wang, R. Kovacevic, Rapid prototyping of 5356-aluminum alloy based on variable polarity gas tungsten arc welding: process control and microstructure, Mater. Manuf. Process. 17 (2002) 103–124. https://doi.org/10.1081/AMP-120002801.

[52] J. Xiong, G. Zhang, W. Zhang, Forming appearance analysis in multi-layer single-pass GMAW-based additive manufacturing, Int. J. Adv. Manuf. Technol. 80 (2015) 1767–1776. https://doi.org/10.1007/s00170-015-7112-4.

[53] Y.-A. Song, S. Park, S.-W. Chae, 3D welding and milling: part II—optimization of the 3D welding process using an experimental design approach, Int. J. Mach. Tools Manuf. 45 (2005) 1063–1069. https://doi.org/10.1016/j.ijmachtools.2004.11.022.

[54] V.T. Le, V.T. Le, An Investigation on the Impact of the Interpass-Cooling Time on the Metallurgy of Wire-Arc-Additive-Manufacturing SS308L Components, in: B.T. Long, Y.-H. Kim, K. Ishizaki, N.D. Toan, I.A. Parinov, N.P. Vu (Eds.), Springer International Publishing, Cham, 2021: pp. 196–201. https://doi.org/10.1007/978-3-030-69610-8_26.

[55] D. Yang, G. Wang, G. Zhang, Thermal analysis for single-pass multi-layer GMAW based additive manufacturing using infrared thermography, J. Mater. Process. Technol. 244 (2017) 215–224. https://doi.org/10.1016/j.jmatprotec.2017.01.024.

[56] H. Zhao, G. Zhang, Z. Yin, L. Wu, Effects of Interpass Idle Time on Thermal Stresses in Multipass Multilayer Weld-Based Rapid Prototyping, J. Manuf. Sci. Eng. 135 (2013) 1–6. https://doi.org/10.1115/1.4023363.

[57] T. Lehmann, A. Jain, Y. Jain, H. Stainer, T. Wolfe, H. Henein, A. Jawad, Concurrent Geometry- and Material-based Process Identification and Optimization for Robotic CMT-based Wire Arc Additive Manufacturing, (2020).

[58] F. Montevecchi, G. Venturini, N. Grossi, A. Scippa, G. Campatelli, Heat accumulation prevention in Wire-Arc-Additive-Manufacturing using air jet impingement, Manuf. Lett. 17 (2018) 14–18. https://doi.org/10.1016/j.mfglet.2018.06.004.

[59] K.P. Karunakaran, S. Suryakumar, V. Pushpa, S. Akula, Low cost integration of additive and subtractive processes for hybrid layered manufacturing, Robot. Comput. Integr. Manuf. 26 (2010) 490–499. https://doi.org/10.1016/j.rcim.2010.03.008.

[60] F.G. Cunha, T.G. Santos, J. Xavier, In situ monitoring of additive manufacturing using digital image correlation: A review, Materials (Basel). 14 (2021). https://doi.org/10.3390/ma14061511.

[61] A. Wagiman, M.S. Bin Wahab, Z. Mohid, A. Mamat, Effect of GMAW-CMT heat input on weld bead profile geometry for freeform fabrication of aluminium parts, Appl. Mech. Mater. 465–466 (2014) 1370–1374. https://doi.org/10.4028/www.scientific.net/AMM.465-

466.1370.

[62] K. Derekar, J. Lawrence, G. Melton, A. Addison, X. Zhang, L. Xu, Influence of Interpass Temperature on Wire Arc Additive Manufacturing (WAAM) of Aluminium Alloy Components, MATEC Web Conf. 269 (2019) 05001. https://doi.org/10.1051/matecconf/201926905001.

[63] S. Edition, Fundamentals of Heat and Mass Transfer, 2015. https://doi.org/10.1007/978-3-319-15793-1_19.

[64] R.D. Murphy, E.C. Forrest, A Review of In-situ Temperature Measurements for Additive Manufacturing Technologies, 2016 NCSL Int. Work. Symp. (2016).

[65] T. Nunak, K. Rakrueangdet, N. Nunak, T. Suesut, Thermal image resolution on angular emissivity measurements using infrared thermography, Lect. Notes Eng. Comput. Sci. 1 (2015) 323–327.

[66] C. Da Wen, Investigation of steel emissivity behaviors: Examination of Multispectral Radiation Thermometry (MRT) emissivity models, Int. J. Heat Mass Transf. 53 (2010) 2035–2043. https://doi.org/10.1016/j.ijheatmasstransfer.2009.12.053.

[67] C.-D. Wen, I. Mudawar, Modeling the effects of surface roughness on the emissivity of aluminum alloys, Int. J. Heat Mass Transf. 49 (2006) 4279–4289. https://doi.org/10.1016/j.ijheatmasstransfer.2006.04.037.

[68] A. Olioso, M. Mira, D. Courault, O. Marloie, P. Guillevic, Impact of surface emissivity and atmospheric conditions on surface temperatures estimated from top of canopy brightness temperatures derived from Landsat 7 data, in: 2013 IEEE Int. Geosci. Remote Sens. Symp. - IGARSS, IEEE, 2013: pp. 3033–3036. https://doi.org/10.1109/IGARSS.2013.6723465.

[69] C. Meola, S. Boccardi, G. maria Carlomagno, Infrared Thermography Basics, in: Infrared Thermogr. Eval. Aerosp. Compos. Mater., Elsevier, 2017: pp. 57–83. https://doi.org/10.1016/B978-1-78242-171-9.00003-6.

[70] C. Meola, S. Boccardi, G. maria Carlomagno, Infrared Thermography Basics, Infrared Thermogr. Eval. Aerosp. Compos. Mater. (2017) 57–83. https://doi.org/10.1016/b978-1-78242-171-9.00003-6.

[71] J.J. Bock, M.K. Parikh, M.L. Fischer, A.E. Lange, Emissivity measurements of reflective surfaces at near-millimeter wavelengths, Appl. Opt. 34 (1995) 4812. https://doi.org/10.1364/ao.34.004812.

[72] C. Meola, S. Boccardi, G. maria Carlomagno, Composite Materials in the Aeronautical Industry, in: Infrared Thermogr. Eval. Aerosp. Compos. Mater., Elsevier, 2017: pp. 1–24. https://doi.org/10.1016/B978-1-78242-171-9.00001-2.

[73] A. Maturilli, J. Helbert, S. Ferrari, M. D'Amore, On the effect of emergence angle on emissivity spectra: application to small bodies, Earth, Planets Sp. 68 (2016).

https://doi.org/10.1186/s40623-016-0464-7.

[74] Z. Lanc, B. Štrbac, M. Zeljković, A. Živković, M. Hadžistević, Emissivity of aluminium alloy using infrared thermography technique, Mater. Tehnol. 52 (2018) 323–327. https://doi.org/10.17222/mit.2017.152.

[75] C. Da Wen, I. Mudawar, Emissivity characteristics of roughened aluminum alloy surfaces and assessment of multispectral radiation thermometry (MRT) emissivity models, Int. J. Heat Mass Transf. 47 (2004) 3591–3605. https://doi.org/10.1016/j.ijheatmasstransfer.2004.04.025.

[76] M. C, C. Cao, S. Pan, X. Li, Nanoparticle-enabled phase control for arc welding of unweldable aluminum alloy 7075, Nat. Commun. 10 (2019) 1–8. https://doi.org/10.1038/s41467-018-07989-y.

[77] J. Xiong, Y. Li, R. Li, Z. Yin, Influences of process parameters on surface roughness of multi-layer single-pass thin-walled parts in GMAW-based additive manufacturing, J. Mater. Process. Technol. 252 (2018) 128–136. https://doi.org/10.1016/j.jmatprotec.2017.09.020.

[78] H. Geng, J. Li, J. Xiong, X. Lin, D. Huang, F. Zhang, Formation and improvement of surface waviness for additive manufacturing 5A06 aluminium alloy component with GTAW system, Rapid Prototyp. J. 24 (2018) 342–350. https://doi.org/10.1108/RPJ-04-2016-0064.

[79] K. Samadian, W. De Waele, Fatigue Crack Growth Model Incorporating Surface Waviness For Wire+Arc Additively Manufactured Components, Procedia Struct. Integr. 28 (2020) 1846–1855. https://doi.org/10.1016/j.prostr.2020.11.008.

[80] D. Shi, W. Xing, J. Sun, Z. Zhu, Emissivity Model of Aluminum 7075 During the Growth of Oxide Layer Over the Temperature Range from 800 to 910 K at a Wavelength of 1.5 μm, Trans. Indian Inst. Met. 71 (2018) 1049–1060. https://doi.org/10.1007/s12666-017-1239-y.

[81] ISO 10904:2004, International Standard ISO 25178-2 Geometrical product specifications (GPS) — Surface texture: Areal —, 2003.

[82] J. Hu, Z. Liu, J. Zhao, B. Wang, Q. Song, Theoretical Modeling and Analysis of Directional Spectrum Emissivity and Its Pattern for Random Rough Surfaces with a Matrix Method, Symmetry (Basel). 13 (2021) 1733. https://doi.org/10.3390/sym13091733.

[83] J.A. Sobrino, J. Cuenca, Angular variation of thermal infrared emissivity for some natural surfaces from experimental measurements, Appl. Opt. 38 (1999) 3931. https://doi.org/10.1364/AO.38.003931.

[84] N. Pavan Kumar, S. Arungalai Vendan, N. Siva Shanmugam, Investigations on the parametric effects of cold metal transfer process on the microstructural aspects in AA6061, J. Alloys Compd. 658 (2016) 255–264. https://doi.org/10.1016/j.jallcom.2015.10.166.

[85] M. Chen, D. Zhang, C. Wu, Current waveform effects on CMT welding of mild steel, J. Mater. Process. Technol. 243 (2017) 395–404.

https://doi.org/10.1016/j.jmatprotec.2017.01.004.

[86] P. Wang, S. Hu, J. Shen, Y. Liang, Characterization the contribution and limitation of the characteristic processing parameters in cold metal transfer deposition of an Al alloy, J. Mater. Process. Technol. 245 (2017) 122–133. https://doi.org/10.1016/j.jmatprotec.2017.02.019.

[87] Fronius International GmbH, RCU 5000i Remote control Manual, 2017.

[88] P. Henckell, M. Gierth, Y. Ali, J. Reimann, J.P. Bergmann, Reduction of Energy Input in Wire Arc Additive Manufacturing (WAAM) with Gas Metal Arc Welding (GMAW), Materials (Basel). 13 (2020) 2491. https://doi.org/10.3390/ma13112491.

[89] J. Nadzam, F. Armao, L. Byall, D. Kotecki, D. Miller, Gas Metal Arc Welding Product and Procedure Selection, Tech Rep. C4.200. (2014) 96. www.lincolnelectric.com.

[90] Y. Yehorov, L.J. da Silva, A. Scotti, Balancing WAAM Production Costs and Wall Surface Quality through Parameter Selection: A Case Study of an Al-Mg5 Alloy Multilayer-Non-Oscillated Single Pass Wall, J. Manuf. Mater. Process. 3 (2019) 32. https://doi.org/10.3390/jmmp3020032.

[91] P. Bałon, E. Rejman, R. Smusz, J. Szostak, B. Kiełbasa, Implementation of high speed machining in thin-walled aircraft integral elements, Open Eng. 8 (2018) 162–169. https://doi.org/10.1515/eng-2018-0021.

[92] D. Özdemirler, S. Gündüz, M.A. Erden, Influence of NbC addition on the sintering behaviour of medium carbon PM steels, Metals (Basel). 7 (2017). https://doi.org/10.3390/met7040121.

[93] ASTM E8, ASTM E8/E8M standard test methods for tension testing of metallic materials, (2010) 1–27. https://doi.org/10.1520/E0008.

[94] S.T. Methods, Standard Test Methods for Tension Testing Wrought and Cast Aluminum- and Magnesium-Alloy Products1, i (2010) 1–16. https://doi.org/10.1520/B0557-10.2.

[95] K. Senthil, M.A. Iqbal, P.S. Chandel, N.K. Gupta, Study of the constitutive behavior of 7075-T651 aluminum alloy, Int. J. Impact Eng. 108 (2017) 171–190. https://doi.org/10.1016/j.ijimpeng.2017.05.002.

[96] S.W. Williams, F. Martina, A.C. Addison, J. Ding, G. Pardal, P. Colegrove, Wire + Arc additive manufacturing, Mater. Sci. Technol. (United Kingdom). 32 (2016) 641–647. https://doi.org/10.1179/1743284715Y.0000000073.

Appendix I

Table 25. The detail of tensile testing result (EUL = 0.5% strain).

	DT15-H	DT15-V	DT30-H	DT30-V	DT60-H	DT60-V	T350-H	T350-V	T250-H	T250-V	T150-H	T150-V
Young's modulus (N/mm^2)	8556.90	8252.60	8540.20	8483.40	8794.00	8780.50	8240.30	8172.80	8664.10	8501.60	8877.40	8814.40
Yield Strength (MPa)	39.56	40.51	41.35	43.00	14.26	40.22	39.88	39.12	40.63	42.09	43.60	42.80
Yield Strain	0.005	0.005	0.005	0.005	0.005	0.005	0.005	0.005	0.005	0.005	0.005	0.005
Ultimate tensile Strength (MPa)	509.93	484.57	539.09	502.94	568.55	495.50	565.71	554.59	608.36	607.66	610.94	591.72
Break Strain	0.20	0.22	0.23	0.25	0.25	0.20	0.20	0.23	0.20	0.20	0.20	0.21

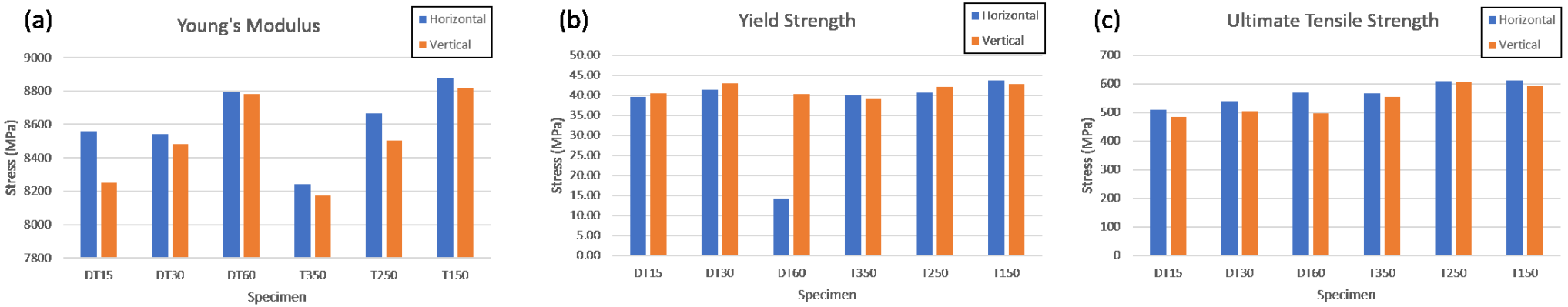

Figure 58. Comparison of (a) Young's modulus, (b) yield strength (EUL = 0.5% strain), and (c) ultimate tensile strength between specimens.